

Colloidal Microswimmers driven by Thermophoresis

Inaugural-Dissertation

zur
Erlangung des Doktorgrades
der Mathematisch-Naturwissenschaftlichen Fakultät
der Universität zu Köln
vorgelegt von

Martin Wagner
aus Düsseldorf

Köln
2017

Berichterstatter:
(Gutachter)

Prof. Dr. Gerhard Gompper
Prof. Dr. Ulrich K. Deiters
Dr. Marisol Ripoll

Tag der mündlichen Prüfung: 8. November 2017

Abstract

Synthetic colloidal microswimmers have received increasing scientific interest over the past years due to their potential applications in micro-fluidics and medicine. The dynamics of such swimmers depend on many factors such as confinement, hydrodynamics, surface interactions, or external fields. The driving mechanism of phoretic colloidal swimmers is based on an asymmetric structure. One part of the swimmer will steadily produce a local gradient (temperature, concentration, or charge) in the surrounding fluid. A different part of the swimmer will be exposed to that gradient, decaying along its surface, and thereby experiences a phoretic driving force. Since many effects are simultaneously present in real-world applications, computer simulations offer a versatile tool to understand the dynamics of microswimmers, especially through the possibility of turning specific interactions or effects off and hence understanding how they affect the behavior.

In this thesis, thermal microswimmers, especially those with a dimeric type of construction, are studied using a mesoscopic computer simulation method, multi-particle collision dynamics, which correctly describes the major features required for thermophoresis, i.e. heat transport and hydrodynamics. After a general introduction to the subject matter and methods, the general microscopic, hydrodynamic framework of phoretic effects is extended to model colloidal thermophoresis as the combined effect of a temperature and corresponding density gradient, with application to single colloid thermophoresis. The obtained results match simulation measurements well and make it possible to easily predict the response of colloids modeled with arbitrary interactions to a temperature gradient. Single swimmer dynamics are studied for two reference models, the Janus particle and the dimer type of construction. Their construction parameters determine their behavior, both in terms of propulsion velocity as well as hydrodynamic flow fields. The latter may qualitatively change, especially in case of the dimer which shows a prominent change between lateral hydrodynamic repulsion and attraction as a function of its geometric construction. Pairs of dimers are studied as well, showing a variety of depletion-induced bound states. Comparison between chemically and thermally driven swimmers shows their qualitative behavior to not depend on the phoretic mechanism employed for propulsion, neither for single swimmers nor pairs. An examination of depletion interactions is undertaken, which arise as a simulation artifact in the simulation method. On this basis, parameters are chosen to physically correct employ the simulation method in the context of many-particle systems, without spurious depletion interactions. Ensembles of thermophoretic dimers are studied in large-scale simulations. Phoretic attraction is shown to lead to crystallization dynamics, with microswimmers forming large and long-time stable, ordered

aggregates. In case of phoretic repulsion, when combined with hydrodynamic lateral attraction stemming from the choice of appropriate construction parameters, a unique kind of dynamic, front-like swarming behavior emerges at intermediate swimmer densities. This phenomenology may offer more versatility and new possibilities in the design of applications based on active matter systems.

Kurzzusammenfassung

Aufgrund ihrer vielfältigen möglichen Anwendungspotentiale in Bereichen wie Mikrofluidik und Medizin haben synthetische, kolloidale Mikroschwimmer in den letzten Jahren an wissenschaftlicher Bedeutung gewonnen. Das Verhalten dieser Schwimmer hängt von vielen Faktoren ab, unter anderem von ihren spezifischen Oberflächenwechselwirkungen, ihrem hydrodynamischen Verhalten, räumlicher Beschränkung und eventuellen externen Feldern. Der Antriebsmechanismus phoretischer kolloidaler Schwimmer basiert auf ihrer asymmetrischen Struktur. Ein Teil des Kolloids produziert stetig einen lokalen (Temperatur-, Konzentrations- oder elektrischen) Gradienten in der umgebenden Flüssigkeit. Ein anderer Teil des Kolloids ist diesem Gradienten ausgesetzt und erfährt hierdurch eine phoretische Kraft, die den Schwimmer antreibt. Aufgrund der Komplexität dieser Systeme bieten sich Computersimulationen als geeignete Methode an, um die Dynamik von Mikroschwimmern zu untersuchen und zu verstehen, insbesondere da einzelne physikalische Wechselwirkungen kontrolliert zu- und abgeschaltet werden können, was eine Abschätzung ihres spezifischen Einflusses auf das System ermöglicht.

Die vorliegende Arbeit beschäftigt sich mit thermischen Mikroschwimmern, insbesondere einer Dimer-artigen Konstruktion. Zur Untersuchung wird die mesoskopische Simulationemethode *multi-particle collision dynamics* benutzt, die die für Thermophorese notwendigen physikalischen Prozesse, vornehmlich Hydrodynamik und Wärmetransport, korrekt beschreibt. Nach einer allgemeinen Einführung in Thema und Methoden wird eine Erweiterung der grundlegenden Beschreibung phoretischer Effekte auf Thermophorese vorgestellt, in deren Rahmen der thermophoretische Effekt als Kombination der Einflüsse eines Temperaturgradienten und des daraus resultierenden Dichtegradienten interpretiert wird. Diese Beschreibung wird im Rahmen der Thermophorese einzelner Kolloide getestet und zeigt gute Übereinstimmung mit Simulationsergebnissen. Sie ermöglicht eine leichte Vorhersage der Reaktion durch beliebige Wechselwirkungspotentiale modellierter Kolloide auf einen Temperaturgradienten. Die Dynamik einzelner Mikroschwimmer wird für die Referenzmodelle der Janus- und der Dimer-Konstruktion untersucht. Neben der Antriebsgeschwindigkeit zeigt deren geometrische Konstruktion entscheidenden Einfluss auf ihre hydrodynamischen Strömungsfelder. Letztere können sich als Funktion der geometrischen Konstruktion des Schwimmers qualitativ ändern, insbesondere im Sinne eines ausgeprägten Wechsels von lateraler Anziehung zu Abstoßung im Falle des Dimers. Die Untersuchung von Paaren von Dimeren zeigt die Bildung einiger gebundener Zustände auf, die durch *depletion*-Wechselwirkungen induziert werden. Der Vergleich zu chemisch angetriebenen Mikroschwimmern zeigt, dass das qualitative Verhalten phoretischer Mikroschwimmer nicht von der Art

des phoretischen Antriebs abhängt. Die *depletion*-Wechselwirkung tritt artifiziell in mesoskopischen Simulationen auf. Eine genauere Untersuchung ermöglicht es, durch Auswahl geeigneter Parameter Mikroschwimmer ohne *depletion* zu modellieren. Darauf aufbauend wird der Fall großer Systeme von Dimeren untersucht. Im Falle phoretischer Anziehung stellt ebendiese den wesentlichsten Einfluss auf die Dynamik der Schwimmer dar und führt zur Bildung stabiler, kristalliner Strukturen. Der entgegengesetzte Fall phoretischer Abstoßung resultiert, im Zusammenspiel mit lateraler hydrodynamischer Anziehung und bei mittleren Dichten, in der Bildung einzigartiger Schwärme von Dimeren mit ausgeprägter Tendenz zur geordneten Bewegung in planaren Schichten. Dieses Schicht-artige Schwarmverhalten von Kolloiden hat Anwendungspotential in Bereichen der weichen Materie und könnte dort neue Konstruktionsmöglichkeiten eröffnen.

Contents

List of Figures	v
List of Tables	vii
Acronyms	ix
Symbols	xi
1 Introduction	1
1.1 Hydrodynamics	6
1.2 Colloidal Dynamics	7
1.2.1 Active Colloids	8
1.3 Thermophoresis	9
1.3.1 Theoretical Description	9
1.3.2 Experimental and Simulation Results	12
2 Simulation Methods	15
2.1 Molecular Dynamics	15
2.2 Interaction Potentials	16
2.3 Mesoscale Simulation Techniques	18
2.4 Multi-Particle Collision Dynamics	19
2.4.1 Introduction of Temperature Gradients	21
2.4.2 Coupling to Colloidal Dynamics	21
2.4.3 MPC Fluid Properties	22
2.5 Implementation of MPC-MD in LAMMPS	24
3 Theoretical Approach to Thermophoresis	27
3.1 Phoretic slip velocity	27
3.2 Diffusiophoresis	28
3.2.1 Slip Velocity	29
3.2.2 Phoretic Force	30
3.3 Thermophoresis	30
3.3.1 Force on a Colloid	30
3.3.1.1 Comparison to Simulation	34
3.3.1.2 Correction for Finite Size Effects	34
3.3.2 Slip Velocity due to Thermophoresis	37
3.4 Analysis of Thermophoresis	39
3.4.1 Simulation Results	39

3.4.2	Size Dependence	40
3.4.3	Temperature Dependence	41
3.4.4	Hard Spheres	44
3.5	Summary and Outlook	45
4	Single Swimmer Dynamics	47
4.1	Dimeric Swimmers	47
4.1.1	Model	48
4.1.2	Theoretical Approaches	48
4.1.3	Theoretical Description of Thermophoretic Dimers	52
4.1.4	Single Dimer Dynamics	53
4.1.4.1	Swimming Velocity	53
4.1.4.1.1	Fixed Size of Hot Bead	57
4.1.4.2	Hydrodynamics	59
4.2	Janus Particle	64
4.2.1	Introduction	64
4.2.2	Model	64
4.2.3	Single Particle Dynamics	65
4.2.3.1	Swimming Velocity	65
4.2.3.2	Hydrodynamics	66
4.3	Mapping to Real Units	69
4.4	Conclusion and Outlook	69
5	Dynamics of Pairs of Dimers	71
5.1	Introduction	71
5.2	Simulation Setup	71
5.2.1	Quantification of Bound States	72
5.3	Results	72
5.3.1	Bound States	72
5.3.2	Phase Diagram	76
5.4	Summary and Conclusions	78
6	Depletion Interactions	81
6.1	Introduction	81
6.2	Theory for Penetrable Hard Spheres	81
6.3	Application to MPC-MD	83
6.3.1	Comparison to Simulations	84
6.4	Colloid-Colloid Interaction Tuning to Avoid Depletion	86
6.4.1	Combination with Bounce-Back	90
6.5	Summary and Conclusion	90
7	Collective Swimmer Dynamics	91
7.1	Introduction	91

7.2	Collective Behavior of Dimers	93
7.2.1	Simulation Model	93
7.2.2	Properties of Reference Dimers	95
7.2.3	Analysis of Clusters	97
7.2.4	Langevin Dynamics	98
7.2.5	Collectives of Thermophilic Dimers	99
7.2.6	Collectives of Thermophobic Dimers	104
7.2.6.1	Swarming Behavior	104
7.2.6.2	Structural Characteristics	108
7.2.6.3	Finite Size Effects	111
7.2.6.4	Effect of Volume Fraction	112
7.2.6.5	Inclusion of Depletion Effects	115
7.3	Summary and Discussion	118
8	Concluding Summary and Outlook	121
	Bibliography	125
	Acknowledgements	135
	Eigenhändigkeitserklärung	137
	Curriculum Vitae	139

List of Figures

1.1	Microscope images of several biological microswimmers.	1
1.2	Several examples of collective motion of micro- and macroorganisms.	2
1.3	Examples of artificial microswimmers.	4
1.4	Examples of dimeric microswimmers.	5
1.5	Experimental results on the Soret coefficient.	13
2.1	Schematics showing the MPC algorithm.	19
2.2	Scaling results of the MPC-MD implementation.	25
3.1	Local coordinate system attached to the colloidal surface.	28
3.2	Fluid temperature and density distribution in the scenario of thermal gradients.	32
3.3	Flow field and backflow of a fixed colloid in a temperature gradient.	36
3.4	Temperature dependence of the Soret coefficient.	43
3.5	Analysis of contributions to the slip velocity.	43
3.6	Size dependence of the Soret coefficient for hard spheres with radius B	45
4.1	Snapshots of synthesized dimers.	47
4.2	Schematic of a dimer and corresponding bispherical coordinate system.	49
4.3	Finite size effect on the propulsion velocity of a dimer swimmer.	54
4.4	Dimer swimming velocities as a function of geometric construction.	56
4.5	Dimer propulsion velocity as a function of γ when the size of the hot bead is fixed and size dependence of the symmetric dimer's velocity.	58
4.6	Flow fields of thermally driven dimers.	60
4.7	Flow field characterization for thermophobic dimers.	62
4.8	Propulsion velocities and flow fields of a thermally driven Janus colloid and their dependence on the coating angle.	67
5.1	Schematic of quantitative descriptors for bound states of two dimers.	72
5.2	Bound states of thermophilic dimers.	73
5.3	Bound states of thermophobic dimers.	73
5.4	Structural features of the Brownian Pair bound states.	74
5.5	Structural features of the Moving Pair and Swimming-Together Pair bound states.	75
5.6	Structural features of the Rotating Pair and Reverse Brownian Pair bound states.	75
5.7	Phase diagrams for bound state formation of pairs of dimers.	76

6.1	Depletion-induced clustering of polystyrene spheres.	81
6.2	Sketch of depletion mechanism.	82
6.3	Depletion forces for different simulation parameters.	85
6.4	Examples of depletion potentials.	88
6.5	Depletion forces when displacements are used.	89
7.1	Structures of ensembles of self-propelled rods.	92
7.2	Influence of displacements on dimer properties.	94
7.3	Flow fields of thermally driven dimers used in simulations of bigger ensembles.	96
7.4	Snapshots of ensembles of thermophilic dimers.	100
7.5	Properties of ensembles of thermophilic dimers.	102
7.6	Bigger ensemble of thermophilic dimers.	104
7.7	Snapshots of ensembles of thermophobic dimers.	105
7.8	Cluster properties of ensembles of thermophobic dimers.	106
7.9	Snapshots of swarms of asymmetric thermophobic dimers.	108
7.10	Structural features of collectives of thermophobic dimers.	109
7.11	Percolated formation of asymmetric dimers.	111
7.12	Cluster properties of ensembles of asymmetric thermophobic dimers at different volume fractions.	113
7.13	Phase diagram of thermophobic dimers.	114
7.14	Snapshots of ensembles of depleted thermophobic dimers.	116
7.15	Cluster properties of ensembles of asymmetric, depleted, thermophobic dimers.	117

List of Tables

2.1	Analytic predictions for MPC fluid properties.	22
3.1	Theoretical and simulation results on the thermal diffusion factor. .	35
3.2	Theoretical and simulation results on the size dependence of the thermal diffusion factor.	40
7.1	Single dimer properties for the two reference constructions of thermophobic and thermophilic dimers.	97

Acronyms

- AO** Asakura-Oosawa. 82
- BD** Brownian Dynamics. 18
- BP** Brownian Pair. 72–74, 77, 78
- IP** Independent Pair. 72, 73, 77
- LD** Langevin Dynamics. 18, 98, 99, 102, 103, 106, 107, 109, 110, 113, 115, 119
- LJ** Lennard-Jones. 17
- MD** Molecular Dynamics. 15, 16, 18, 22, 24, 25
- MIPS** Motility-Induced Phase Separation. 2, 64, 91, 93, 118
- MP** Moving Pair. 72–75, 77, 78
- MPC** Multi-Particle Collision Dynamics. 15, 19–25, 30–32, 36, 39, 64, 65, 71, 83–86, 98, 119
- MPC-MD** Multi-Particle Collision Dynamics coupled to Molecular Dynamics. 22, 24, 25, 30, 31, 34, 45, 46, 48, 68, 71, 78, 79, 81, 83–85, 90, 93, 98, 99, 102, 103, 106, 107, 109, 110, 112, 114–116, 119–122
- MSD** Mean Squared Displacement. 7, 95
- RBP** Reverse Brownian Pair. 73–75, 77
- RP** Rotating Pair. 73–75, 77
- SPTA** Single-Particle Thermal Diffusion Algorithm. 34–36, 44
- ST** Swimming-Together Pair. 73–75, 77, 78, 122
- WCA** Weeks-Chandler-Andersen. 17, 18, 87, 89

Symbols

ω	Angular velocity
k_B	Boltzmann constant
B	Boundary layer width
c	Concentration
ρ	Density
D	Diffusion coefficient
d	Dimensionality
γ	Dimer bead size ratio
δ_b	Dimer bond length parameter
r	Distance
μ_d	Dynamic viscosity
Ξ	Eigenvalue of gyration tensor
W	External potential
δ	Extra separation distance
\mathbf{G}	Fluctuation strength
D_f	Fluid diffusion coefficient
ζ	Fluid friction coefficient
\mathbf{J}	Flux
$f, \mathbf{f}, F, \mathbf{F}$	Force
q	Heat flux
\mathbf{I}	Identity matrix
U	Interaction potential
r_c	Interaction potential cutoff
Δ	Interaction potential displacement
s	Interaction potential effective range
n	Interaction potential exponent
σ	Interaction potential range parameter
C	Interaction potential shift parameter
ε	Interaction potential strength parameter
θ_c	Janus coating angle
ν	Kinematic viscosity
Ma	Mach number
m, M	Mass
μ	Mobility
\mathbf{p}	Momentum exchange
Ψ	MPC Bin

a	MPC cell side length
h	MPC collision time
α	MPC rotation angle
\mathcal{R}	MPC rotation matrix
n_ρ	Number density
N	Number of swimmers
e	Orientation
Pe	Peclet number
\mathbf{r}, \mathbf{R}	Position vector
E	Potential energy
Pr	Prandtl number
p	Pressure
P	Probability density
R	Radius
ξ	Random force
τ	Relaxation time
r/a	repulsive/attractive
Re	Reynolds number
D_r	Rotational diffusion coefficient
Sc	Schmidt number
$L_{x,y,z}$	Simulation box dimensions
S_T	Soret coefficient
T	Temperature
k_T	Thermal conductivity
D_T	Thermal diffusion coefficient
α_T	Thermal diffusion factor
β_T	Thermal expansion coefficient
t	Time
v, \mathbf{v}	Velocity
V	Volume
ϕ	Volume fraction

1 Introduction

The motion of biological organisms at the microscale, such as bacteria, viruses or sperm cells, shows unique features. These organisms move in a fluid environment, and in a region where the Reynolds number Re , a hydrodynamic number characterizing the ratio of inertial to viscous forces, is low. Therefore their motion is nearly inertia-free, and swimming strategies different from what one is intuitively used to from the macroscopic world are employed to achieve directed motion in these environments. Most biological swimmers feature some form of flagella, short or long filaments that stick out from the cell body, whose motion can be controlled by a cellular motor. To achieve self-propulsion, sperm cells employ a wiggling motion of one long flagellum. *E.coli* bacteria and *Salmonella* on the other hand use a helical rotation of a bundle of elongated flagella. Other types of cells, such as paramecium, are covered with many short filaments, called cilia, that perform coordinated strokes to induce motion of the whole cell body. Figure 1.1 shows microscope images of these microorganisms.

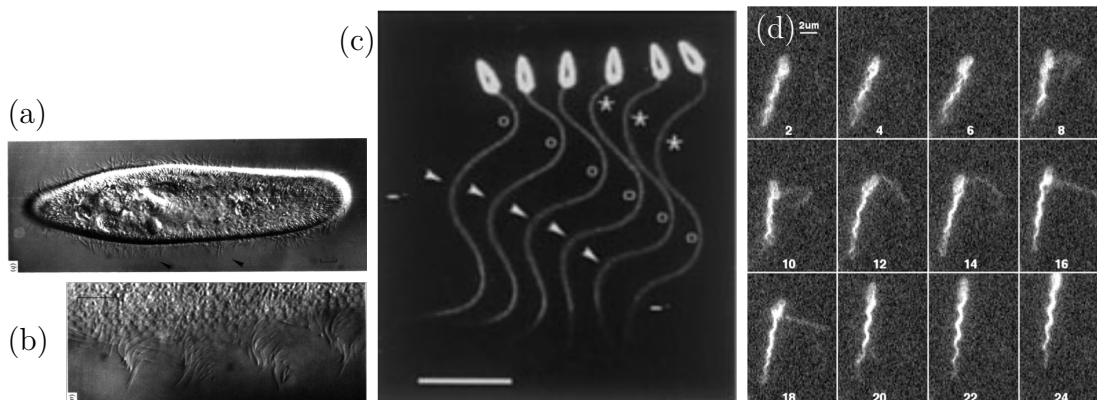
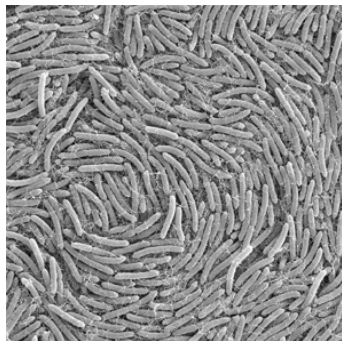


Figure 1.1: Microscope images of several biological microswimmers. **a)** Paramecium bacterium as a whole. **b)** Metachronal wave of cilia on the paramecium's surface; their wave-like motion induces propulsion of the whole bacterium. Both taken from [1]. **c)** Wiggling motion of a sea urchin sperm cell. From [2]. **d)** *E. coli* cell with several flagellar filaments, one undergoing a polymorphic transformation. This leads to their typical run-and-tumble trajectories. From [3].

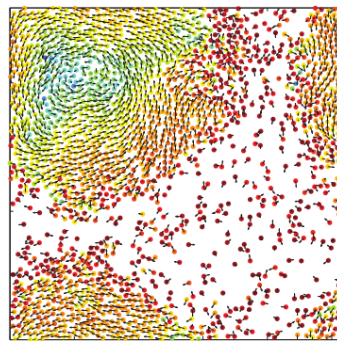
Common to all these organisms is that the motion is *active*. Active in this context refers to the fact that these organisms convert some form of energy, either stored internally or taken up from the environment, into directed motion [4, 5]. This stands in contrast to passive particles, which only move through Brownian

random motion [6]. Due to the motion being active, there is a constant uptake and conversion of energy such that these systems are inherently far from equilibrium. The research field of active matter has received great interest, increasingly so in the past years [7].

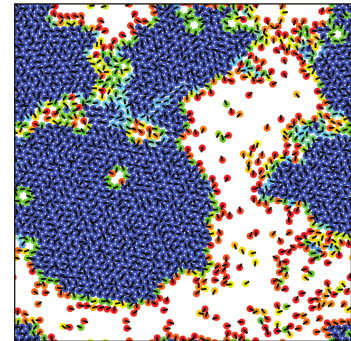
Though the propulsion mechanisms may be vastly different on the micro- to nanoscale from those used by animals on the macroscale, similarities especially concerning their collective motion emerge. The non-equilibrium collective phenomena that occur in groups of actively moving organisms or particles, both on the micro- as well as on the macroscale, include the emergence of swarming behavior, Motility-Induced Phase Separation (MIPS), lane formation, or schooling among others. The observed patterns are similar for both bacterial organisms and macroscopic animals such as birds, fish or sheep. Figure 1.2 illustrates examples of the diverse kinds of collective motion in both microscopic and macroscopic as well as biological and synthetic systems.



(a) Electron microscope image of a vortex formed by the bacterium *P. vortex*.¹



(b) Vortex formation in a simulation of active colloids. From [8].



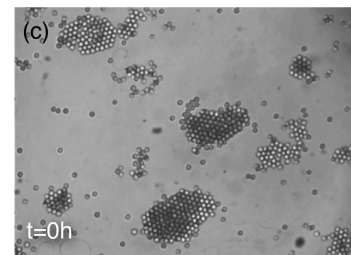
(c) Motility-Induced Phase Separation (MIPS) in simulations of active colloids. From [9].



(d) Vortex formation in a swarm of fish. From [5].



(e) Swarming behavior of fish. From [5].



(f) MIPS of Janus colloids. From [10].

Figure 1.2: Several examples of collective motion of micro- and macroorganisms.

¹This picture is taken from https://en.wikipedia.org/wiki/Paenibacillus_vortex#/media/File:Vortex_fig_2.tif.

The study of the motion of bacteria belongs to the field of *soft matter*. This term also encompasses systems such as gels, polymers, colloidal suspensions, foams, cell

networks etc., often as a suspension of larger particles or organisms in a solvent. Typically, the relevant length scale of these systems lies in the mesoscopic range, i.e. nm to μm , and the relevant energy scales are of order $k_{\text{B}}T$, such that these systems are to a high degree influenced by thermal fluctuations. For suspended particles, solvent-mediated hydrodynamic effects often play a crucial role in determining their dynamics.

In more recent years, there have been efforts to develop artificial synthetic constructs that also show self-propelled behavior on the microscale. The construction of microscale objects with active and controllable motion would offer valuable possibilities in a variety of applications. Targeted cargo transport in microchannels could offer the possibility to precisely distribute drugs to designated areas. Microswimmers could analogously remove harmful substances from fluid environments. Systems with active components may be used to construct materials with controllable properties.

The first microswimmer constructed to mimic a biological mechanism was the one of Dreyfus et al. [11]. They constructed an artificial sperm by attaching a linear chain of magnetic colloidal particles to a red blood cell. With an oscillating magnetic field, they were able to induce a wiggling motion of the artificial filament, making it swim as illustrated in fig. 1.3a. One of the first microswimmers that does not mimic a biological propulsion mechanism was constructed by Paxton et al. [12]. These authors used a bimetallic nano-rod, consisting half of platinum, half of gold, which upon immersion in a solution of hydrogen peroxide showed self-propulsion. The decomposition of hydrogen peroxide is catalyzed by platinum and the resulting interaction of reactants with the gold half is responsible for the propulsion, though the precise details of how this takes place do still have open questions [7].

For spherical particles, a similar type of construction is called a Janus particle, and it is being widely investigated. This term describes colloidal, spherical particles whose one half is covered with or consists of a different material than the other. Catalytic Janus particles employing also the platinum-catalyzed decomposition of hydrogen peroxide have been realized by Howse et al. [13], based on theoretical considerations by Golestanian et al. [14]. Examples for the discussed types of artificial microswimmers are shown in fig. 1.3.

Propulsion based, among others, on the decomposition of hydrogen peroxide takes advantage of what is called a *phoretic* effect. Phoresis ("migration") refers to the fact that colloidal particles react to a gradient of a field of some sort by migrating on average either up (in the philic case) or down (in the phobic case) this gradient. The gradient can for example be an electric, concentration, thermal or magnetic field gradient. In the case of catalytic Janus particles, the gradient may just be a concentration gradient, which by itself is sufficient to produce self-propulsion [16]. Phoresis based solely on a concentration gradient is termed diffusiophoresis. However, other effects due to electrostatics, bulk chemical reactions etc. will also influence the behavior of these particles [17]. A dimeric type of construction, in spirit similar to the Janus particle, was suggested in simulation studies by Rückner and Kapral [18]. This swimmer consists of two closely connected spherical particles,

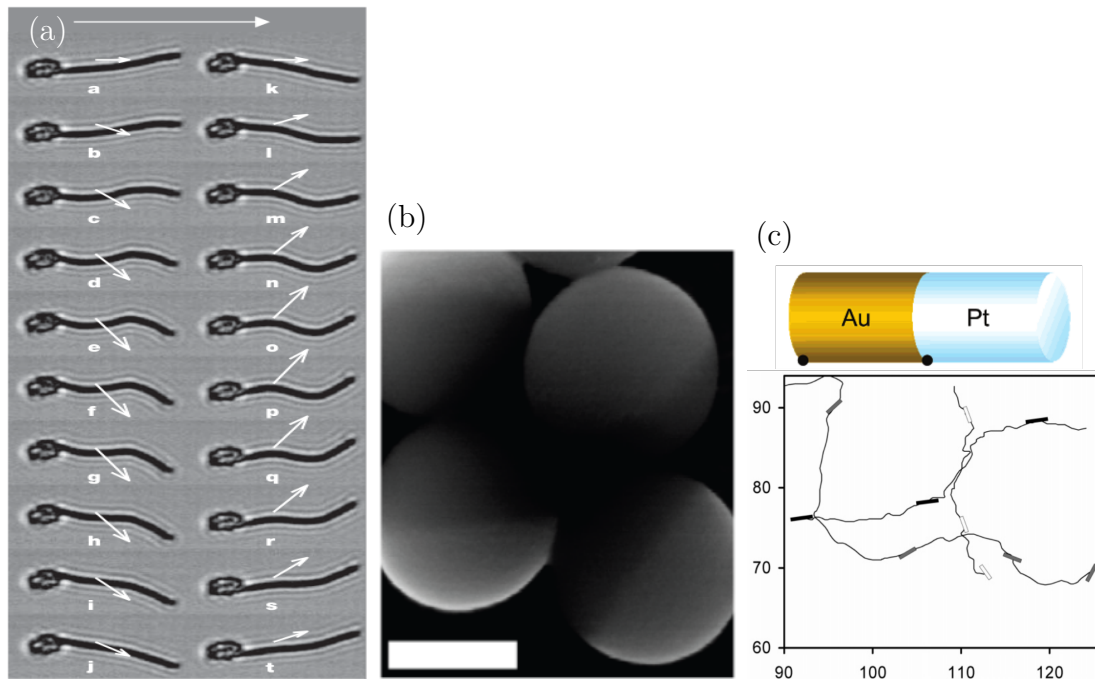


Figure 1.3: Examples of artificial microswimmers. **a)** An artificial microswimmer constructed by attaching a flexible magnetic filament to a red blood cell, mimicking the propulsion of sperm. From [11]. **b)** A colloidal Janus swimmer made of latex, coated half with platinum. From [15]. **c)** Top: Schematic of the bimetallic nanorod. Bottom: Typical trajectory, showing enhanced diffusion due to self-propulsion. From [12].

one of which is phoretically active. An experimental realization of this construction was performed later on by Valadares et al. [19]. Typical velocities reached by phoretically driven microswimmers are in the $\mu\text{m/s}$ range [20].

The focus of this thesis lies on artificial colloidal microswimmers driven by the thermophoretic mechanism. Utilizing thermal gradients, i.e. by heating suitable colloids through laser illumination to propel microswimmers, can be advantageous in real-world applications. Laser sources allow for a very precise control of the applied heating both in space and in time. Furthermore, the mechanism does not require a specific solvent chemistry, i.e. no toxic chemicals are necessary for it to work. Thermophoresis, or the Soret effect, is commonly characterized by the so-called Soret coefficient S_T , describing how a colloid reacts to a surrounding temperature gradient. It may have a positive value, in case of the colloid being thermophobic, i.e. it moves to the cold region, or a negative value when the colloid reacts thermophilic and moves to the warm. More commonly, colloidal particles react thermophobic to temperature gradients. The magnitude, as well as the sign, of the Soret coefficient depend on a multitude of factors, among them the particle's mass, size, charge, moment of inertia as well as the particular interaction details of the particle with the solvent [21]. Furthermore, it is influenced by factors like

the salt concentration in the solvent and the precise details of the particle-particle interactions on the molecular level. The combination of all these factors makes a theoretical description of thermophoresis very complex, and a detailed microscopic description of thermophoresis is still a matter of ongoing research. On the other hand, the multitude of influences also implies that a system making use of the thermophoretic mechanism is highly tunable [22]. For example, the Soret coefficient might change sign when the average temperature is changed, which allows reverting the migration of colloids by heating or cooling the complete sample.

The first application of thermophoresis to microswimmers was done by Jiang et al. [23], who build a Janus particle by depositing gold on polystyrene as well as silica particles. Illumination with a laser lead to a local heating of the gold-coated cap, which in turn induces self-thermophoresis. Simulation studies on thermophoretic microswimmers were performed by Yang and Ripoll on a dimer type of construction [24] as well as on Janus particles by Yang et al. [25].

The dimer type of construction is of considerable interest, as it has an increased inherent complexity in comparison to the Janus particle due to the additional degrees of freedom in construction. Its collective dynamics will be determined by a complex interplay of phoretic effects, steric interactions, hydrodynamics and thermal fluctuations. The temperature field around a hot particle obeys the Fourier law, decaying with distance like $1/r$. For the phoretic effect, that is proportional to the gradient of the field, implying a decay proportional to $1/r^2$. It has been shown in simulation studies that the hydrodynamic flow field of Janus particles decays like $1/r^3$, such that for these particles hydrodynamic effects are likely less important than phoretic effects [25]. In case of the dimer however, hydrodynamic interactions decay with $1/r^2$, i.e. the same as the phoretic effect, such that interesting combined effects may result in the dynamics of swimmer ensembles. The experimental realization of chemical dimers and the simulated flow fields of a thermophoretic dimer and a thermophilic Janus swimmer are shown in fig. 1.4.

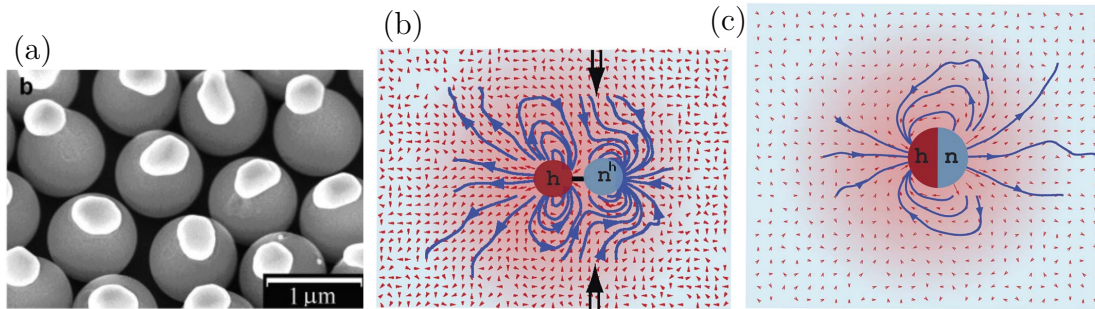


Figure 1.4: Examples of dimeric microswimmers. **a)** Experimental realization of a chemically driven dimeric colloidal swimmer. From [19]. **b)** Simulated flow field of a thermophilic dimer swimmer. **c)** Simulated flow field of a thermophobic Janus swimmer. Both simulated flow fields are taken from [25].

After this general introduction to the subject matter, the following sections will

discuss prerequisites of specific importance to this work in more detail.

1.1 Hydrodynamics

The motion of an incompressible Newtonian fluid is governed by the Navier-Stokes equation

$$\rho \left(\frac{\partial \mathbf{v}}{\partial t} + (\mathbf{v} \cdot \nabla) \mathbf{v} \right) = -\nabla p + \mu_d \nabla^2 \mathbf{v} + \mathbf{f} \quad (1.1)$$

with the incompressibility condition

$$\nabla \cdot \mathbf{v} = 0. \quad (1.2)$$

The velocity field \mathbf{v} , the pressure field p and the external forces \mathbf{f} all depend on position \mathbf{r} and time t . The fluid's dynamic viscosity is denoted μ_d and its density ρ . An adimensionalization of the Navier-Stokes equation is possible by choosing a characteristic length scale l_c , and a characteristic velocity v_c . For flow past a sphere for example, l_c might correspond to the spheres radius or diameter, while v_c could correspond to the fluid velocity at infinity [26]. This choice then leads to a characteristic timescale $t_c = l_c/v_c$. The variables in the Navier-Stokes equation can then be rescaled. Choosing $\mathbf{v}' = \mathbf{v}/v_c$, $t' = t/t_c$, $p' = t_c p/\mu_d$, $f' = l_c^2/(\mu_d v_c) f$ and $\nabla' = l_c \nabla$, one obtains

$$\frac{\rho v_c l_c}{\mu_d} \left(\frac{\partial \mathbf{v}'}{\partial t'} + (\mathbf{v}' \cdot \nabla') \mathbf{v}' \right) = -\nabla' p' + \nabla'^2 \mathbf{v}' + \mathbf{f}' \quad (1.3)$$

for the Navier-Stokes equation. The incompressibility condition reads the same in non-dimensional form, i.e. $\nabla' \cdot \mathbf{v}' = 0$. The prefactor in eq. (1.3) is the Reynolds number

$$\text{Re} = \frac{\rho v_c l_c}{\mu_d}. \quad (1.4)$$

For low Reynolds numbers $\text{Re} \ll 1$, which is characteristic for many soft matter systems, especially microswimmers, this allows neglecting the l.h.s. of eq. (1.3). Then, the fluid dynamics are described by the Stokes equation

$$\nabla p - \mu_d \nabla^2 \mathbf{v} = \mathbf{f} \quad (1.5)$$

with the same incompressibility condition $\nabla \cdot \mathbf{v} = 0$. Interestingly, in the Stokes equation, the variables are no longer dependent on time. Solutions of the Stokes equation depend on the chosen boundary conditions. A discussion for phoretic processes at colloidal surfaces will be given in chapter 3.

1.2 Colloidal Dynamics

The term colloid is commonly used to describe particles with dimensions in the range of roughly 1 nm up to 10 μm , though these limits are not sharp [27]. The lower limit is set by the requirement that the particle should be larger than the surrounding solvent molecules, whereas the upper limit stems from the idea that colloids should be measurably influenced by Brownian motion. Even for the smallest colloid, the difference in length scales with respect to the solvent (ca. one order of magnitude) is large enough that it should be possible to capture the solvent's influence on the colloid by a continuum description. For this to be feasible, the typical time scales of solvent and colloid should also be well separated. Experimentally measured solvent relaxation times are of the order 10^{-14} s, whereas the relevant time scales for colloidal motion start at ca. 10^{-9} s [27], ensuring a large enough separation to account for solvent effects in an averaged way. A (spherical) colloidal particle of mass M immersed in a fluid will then, due to the separation in time and length scales, experience the averaged interaction with the fluid in two ways. For one, it will feel a random force $\boldsymbol{\xi}(t)$, accounting for the random "kicks" it gets through thermal fluctuations of the fluid. Then, it will experience a friction force opposite to its direction of movement and proportional to its velocity \mathbf{v} , with friction coefficient ζ . Together, the resulting equation of motion for the colloid's position \mathbf{r} reads as

$$\ddot{\mathbf{r}} = -\zeta \mathbf{v} + \boldsymbol{\xi} + \frac{\mathbf{F}}{M} \quad (1.6)$$

This is the so-called Langevin equation. \mathbf{F} describes an external force, but in the following discussion it is assumed that none is present. Since the random force should model thermal noise of the solvent, which has no preferred direction, its average should be zero. Due to the large separation in length and time scales between solvent and colloid, the noise is assumed to be Gaussian white noise, which is delta correlated in time, such that

$$\langle \boldsymbol{\xi}(t) \rangle = 0 \quad (1.7)$$

$$\langle \boldsymbol{\xi}(t) \boldsymbol{\xi}(t') \rangle = \mathbf{G} \delta(t - t') \quad (1.8)$$

where \mathbf{G} describes the fluctuation strength, which can be shown, using the equipartition theorem, to be given by

$$\mathbf{G} = 2k_{\text{B}}T\zeta\mathbf{I} \quad (1.9)$$

with \mathbf{I} being the identity matrix. Equation (1.6) and eq. (1.8) then determine the motion of a colloidal particle in random solvent and several characteristic properties may be derived from these equations. The Mean Squared Displacement (MSD) is

given for small times by

$$\langle |\mathbf{r}(t) - \mathbf{r}(0)|^2 \rangle = \mathbf{v}(0)\mathbf{v}(0)t^2 \quad (1.10)$$

and for longer times by

$$\langle |\mathbf{r}(t) - \mathbf{r}(0)|^2 \rangle = \mathbf{I} \frac{2k_B T}{\zeta} t = \mathbf{I} 2Dt \quad (1.11)$$

where D is the diffusion coefficient. Such a relation between a diffusion and friction coefficient, $D = k_B T / \zeta$, is called the Einstein relation.

In the *overdamped* limit, it is assumed that inertial effects do not play a role, therefore the acceleration term drops out of eq. (1.6). The resulting equation of motion is then given by

$$\mathbf{v} = \frac{\boldsymbol{\xi}}{\zeta}. \quad (1.12)$$

This implies that the vanishing of the average velocity is fully determined by the system temperature and realization of the noise. Since most of the systems investigated in this thesis happen to be in the low Reynolds number regime, this is also a reasonable approximation in the description of these.

1.2.1 Active Colloids

For a Brownian colloid at low Reynolds number, the average velocity is zero according to eq. (1.12). However, a driving force \mathbf{F} may act on it, leading to its persistent propulsion. If such driving force is locally produced by the colloid itself, as opposed to an external field like gravity, the colloid is referred to as self-propelled. For self-propelled colloids, the propulsion will typically have an inherent directionality. Therefore, also the orientation of the colloid, along which the self-propulsion force acts, has to be considered in its description. For the reference case of an active Brownian sphere with fixed propulsion velocity v_0 along its orientation vector \mathbf{e} , the Langevin equations describing position and orientation are given by [9]

$$\dot{\mathbf{v}} = v_0 \mathbf{e} + \sqrt{2D} \boldsymbol{\xi} \quad (1.13)$$

$$\dot{\mathbf{e}} = \sqrt{2D_r} \boldsymbol{\xi}_r \times \mathbf{e} \quad (1.14)$$

with D_r the rotational diffusion coefficient and $\boldsymbol{\xi}_r$ the orientational noise, which is also taken to be Gaussian white noise. The orientational autocorrelation of such a particle decays with

$$\langle \mathbf{e}(t) \cdot \mathbf{e}(0) \rangle = \exp\left[\frac{-t}{\tau_r}\right] \quad (1.15)$$

where τ_r describes a characteristic persistence time. For active Brownian spheres, the MSD also takes on a modified form due to the self-propulsion, given by

$$\langle |\mathbf{r}(t) - \mathbf{r}(0)|^2 \rangle = 2dDt - 2v_0^2\tau_r^2t - 2v_0^2\tau_r^2(1 - e^{-t/\tau_r}) \quad (1.16)$$

with d the dimensionality. For small times $t \ll \tau_r$ this takes the form

$$\langle |\mathbf{r}(t) - \mathbf{r}(0)|^2 \rangle = v_0^2t^2 + 2dDt. \quad (1.17)$$

The rotational diffusion coefficient D_r can be obtained through the rotational mean squared displacement, which is given by [27]

$$\langle |\mathbf{e}(t) - \mathbf{e}(0)|^2 \rangle = 2(1 - \exp[-2D_r t]) \quad (1.18)$$

which for small times $2D_r t \ll 1$ can be approximated by

$$\langle |\mathbf{e}(t) - \mathbf{e}(0)|^2 \rangle = 4D_r t. \quad (1.19)$$

1.3 Thermophoresis

Thermophoresis in general describes the effect of an applied temperature gradient on the particle motion of a suspension [28]. Its analogue at the molecular level is thermal diffusion, also called the Ludwig-Soret effect, that refers to the partial segregation of the compounds of a liquid mixture upon application of a temperature gradient. It is a non-equilibrium effect, involving a constant flux of mass in response to the temperature gradient. A colloid immersed in a fluid with a temperature gradient will experience a force due the non-uniform distribution of temperature in the surrounding medium, which leads to a non-vanishing average drift velocity. Non-uniform distributions of temperature may also induce further non-uniformities, for example in the fluid density distribution, which may also affect force the colloid experiences.

1.3.1 Theoretical Description

Van Kampen obtained a general description for the diffusion of a Brownian particle in an inhomogeneous environment [29], which can be connected to thermophoresis of dilute colloidal suspensions [30] leading to an expression for the colloidal drift velocity v_d . The diffusion equation for the probability density $P(\mathbf{r}, t)$ of a particle in a homogeneous medium, including an external potential $W(\mathbf{r})$ that acts on it, is given by

$$\frac{\partial P}{\partial t} = \nabla \cdot [(\mu \nabla W)P + D \nabla P] \quad (1.20)$$

where μ is the mobility and the diffusion coefficient D is given by the Einstein relation $D = \mu T$. In the scenario of an inhomogeneous medium considered by van Kampen, μ , D and T can depend on the spatial coordinate \mathbf{r} . Then, a possible generalization reads as

$$\frac{\partial P}{\partial t} = \nabla \cdot [(\mu \nabla W)P + \nabla DP] \quad (1.21)$$

which is the same as

$$\frac{\partial P}{\partial t} = \nabla \cdot [(\mu \nabla W + \nabla D)P + D \nabla P]. \quad (1.22)$$

Here, the inhomogeneities lead to an additional term ∇DP , referred to as "extra drift". Van Kampen did propose a generalized framework based on consideration of three cases for which the diffusion equation is derived specifically. One of these cases is the diffusion of a Brownian particle in an inhomogeneous surrounding. This can be applied as a model for a colloid situated in a temperature gradient. The Kramers' equation for a Brownian particle describes its dynamics through the evolution of the joint probability of position and velocity $g(x, v, t)$ by

$$\frac{\partial g}{\partial t} = -v \frac{\partial g}{\partial x} + W'(x) \frac{\partial g}{\partial v} + \zeta \left(\frac{\partial}{\partial v} v g + T \frac{\partial^2 g}{\partial v^2} \right) \quad (1.23)$$

where $W' = -f$ denotes the derivative of the potential, i.e. the force f . For high values of ζ , the last term is dominant. Then, one may expand the equation in powers of ζ^{-1} in the spirit of the Chapman-Enskog procedure [31]. To lowest non-vanishing order, with $\mu(x) = 1/\zeta(x)$ and $D(x) = T(x)/\zeta(x)$, the resulting equation is given by

$$\frac{\partial P}{\partial t} = \frac{\partial}{\partial x} \left[\mu W' P + \mu \frac{\partial}{\partial x} T P \right]. \quad (1.24)$$

This can be reformulated in terms of a continuity equation with flux \mathbf{J} as in [29]

$$\frac{\partial P(\mathbf{r}, t)}{\partial t} = -\nabla \cdot \mathbf{J}(\mathbf{r}, t). \quad (1.25)$$

The flux would then be given by [30]

$$\mathbf{J}(\mathbf{r}) = n_\rho \mu(\mathbf{r}) \mathbf{f} - \mu(\mathbf{r}) \nabla [n_\rho(\mathbf{r}) k_B T(\mathbf{r})] \quad (1.26)$$

wherein the notation has been switched from P to particle number density n_ρ and potential V to force $f = -V'$. Assuming validity of local equilibrium and the Einstein relation to hold, one may add and subtract $k_B T(\mathbf{r}) \nabla \mu(\mathbf{r})$ to arrive at [30]

$$\mathbf{J}(\mathbf{r}) = n_\rho(\mathbf{r}) \mathbf{v}_d - \nabla [n(\mathbf{r}) D(\mathbf{r})] \quad (1.27)$$

where the drift velocity of the particle is given by

$$\mathbf{v}_d = \mu \mathbf{f} + k_B T \nabla \mu. \quad (1.28)$$

For a more detailed discussion on interpretation of the involved terms and assumptions see [29] and [30]. Equation (1.27) relates the drift velocity of a particle to its inhomogeneous surrounding given by a spatially inhomogeneous density and value of the diffusion coefficient and/or mobility.

It is interesting to make the connection to the phenomenological expression of thermophoresis. To do so, the phenomenological expression for the mass flux is required. In the framework of non-equilibrium thermodynamics, the entropy production ς in a binary system showing a diffusive mass flux \mathbf{J}_k and heat flux \mathbf{J}_q can be written as [32, 33]

$$\varsigma = -\frac{1}{T^2} \mathbf{J}_q \cdot \nabla T - \frac{1}{T} \sum_{k=1}^2 \mathbf{J}_k \cdot \nabla_T \mu_k. \quad (1.29)$$

Here, ∇T is the thermal gradient, $\nabla_T \mu_k$ is the chemical potential gradient of component k at constant temperature and \mathbf{J}_k the mass flux for component k . The phenomenological equations describing thermophoresis in a binary mixture follow from this as [32]

$$\mathbf{J}_q = -L_{qq} \frac{\nabla T}{T^2} - L_{q1} \nabla_T (\mu_1 - \mu_2) \quad (1.30)$$

$$\mathbf{J}_1 = -L_{1q} \frac{\nabla T}{T^2} - L_{11} \frac{\nabla_T (\mu_1 - \mu_2)}{T} \quad (1.31)$$

where $L_{\alpha\beta}$ are phenomenological coefficients fulfilling Onsager reciprocal relations. A complete derivation can be found in [33]. Taking the solute as species 1, expressing the mass flux in terms of the solute mole fraction $x = n_{\rho,1}/\tilde{n}_\rho$ and the number densities of the two species as $n_{\rho,1}$ and $n_{\rho,2}$ with $\tilde{n}_\rho = n_{\rho,1} + n_{\rho,2}$, the mass flux reads as [28, 30]

$$\mathbf{J}_1 = -\tilde{n}_\rho D_m \nabla x - \tilde{n}_\rho x(1-x) D_T \nabla T. \quad (1.32)$$

Here D_T is the thermal diffusion coefficient and D_m the mutual diffusion coefficient. These are related to the phenomenological coefficients by [33, 34]

$$D_m = L_{11} \frac{\nabla_T (\mu_1 - \mu_2)}{\tilde{n}_\rho T \nabla x} = \frac{L_{11}}{\tilde{n}_\rho (1-x) T} \frac{\partial \mu_1}{\partial x} \quad (1.33)$$

$$D_T = \frac{1}{\tilde{n}_\rho T^2 x(1-x)} L_{1q}. \quad (1.34)$$

In the steady state, the mass flux will vanish: $J_1 = 0$. From this, one obtains

$$S_T = \frac{D_T}{D_m} = -\frac{1}{n_{\rho,1}n_{\rho,2}} \frac{\nabla n_{\rho,1}}{\nabla T} = -\frac{1}{x(1-x)} \frac{\nabla x}{\nabla T} \quad (1.35)$$

as the ratio of thermal diffusion and mutual diffusion coefficient, which is called the Soret coefficient S_T . The Soret coefficient may take on both positive and negative signs, where a positive value of S_T refers to the more commonly observed thermophobic behavior, while a negative sign indicates thermophilic behavior.

In the case when the solute density $n_{\rho,1}$ is low compared to the solvent density $n_{\rho,2}$, the mutual diffusion coefficient D_m is equal to the solute diffusion coefficient D and the mass flux of eq. (1.32) may be compared to eq. (1.27), obtaining [30]

$$\mathbf{v}_d = \nabla D - D\beta_T \nabla T - D_T \nabla T \quad (1.36)$$

with the thermal expansion coefficient $\beta_T = -(1/n_{\rho,2})\partial n_{\rho,2}/\partial T$.

More commonly used is the expression

$$\mathbf{v}_T = -D_T \nabla T \quad (1.37)$$

to express the thermophoretic velocity. This is only equal to the derived drift velocity if the thermal diffusion coefficient is the dominant term in eq. (1.36), such that $|D_T| \gg |dD/dT - D\beta_T|$. The validity of this approximation for colloids in complex fluids has been confirmed in simulation studies on thermal diffusion [35].

Instead of the colloid's velocity, the force acting on it through the temperature gradient may also be used to describe thermophoresis. This thermophoretic force is also linearly related to the temperature gradient through [24]

$$\mathbf{f}_T = -\alpha_T \nabla k_B T, \quad (1.38)$$

where α_T is the thermal diffusion factor.

The characteristic values used to describe colloidal thermophoresis are the Soret coefficient S_T or the related thermal diffusion factor, which is related to the Soret coefficient by [24]

$$\alpha_T = TS_T. \quad (1.39)$$

The Soret coefficient or thermal diffusion factor provides the linear proportionality constant relating the gradients to the response of the colloid.

1.3.2 Experimental and Simulation Results

The thermal diffusion factor α_T is a quantity conveniently used in the description of simulation results, as the forces and temperature gradients are known and directly accessible. More commonly used in experiments to characterize the behavior of colloids is the Soret coefficient S_T of eq. (1.35). As pointed out in the introduction,

S_T depends on a multitude of factors. Notably, it has a complex dependence on temperature and particle size. Experimental results on both temperature and size dependence are shown in fig. 1.5.

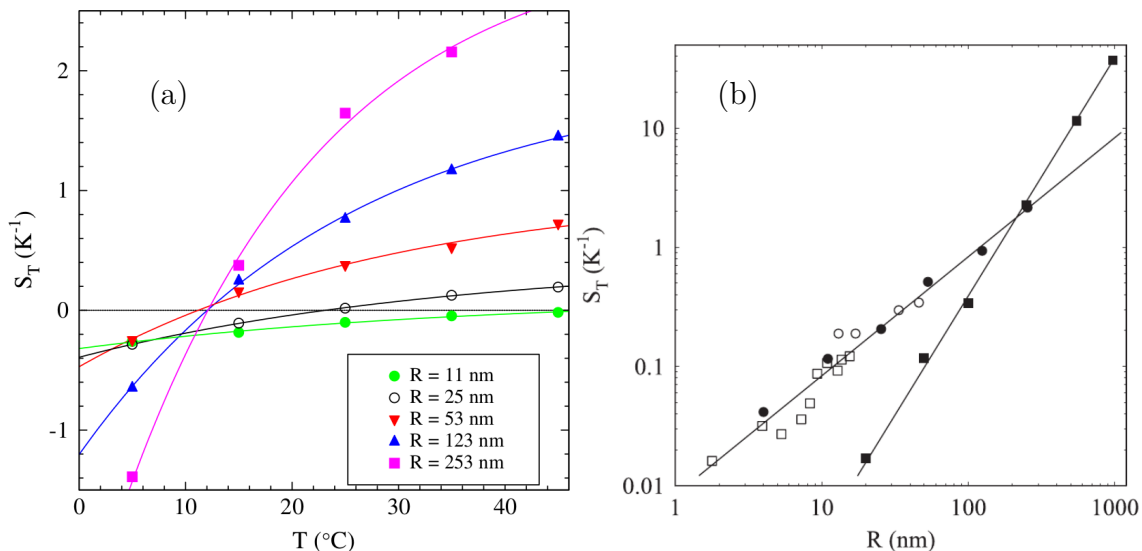


Figure 1.5: Experimental results on the Soret coefficient. **a)** Temperature dependence of the Soret coefficient for polystyrene particles in a dilute aqueous solution. Taken from [36]. **b)** Experimental results on the particle size dependence of the Soret coefficient. Taken from [28]. Experimental data for polystyrene beads from [37] (filled squares), [36] (filled circles), [38] (open circles). Data for water-in-oil microemulsions from [39] (open squares).

Braibanti et al. measured the temperature dependence of the Soret coefficient experimentally [36], obtaining good agreement with the following empirical relation

$$S_T(T) = S_T^\infty \left(1 - \exp\left[\frac{T^* - T}{T_0}\right] \right). \quad (1.40)$$

This expression relies on three material-dependent, adjustable parameters T^* , T_0 , and S_T^∞ . Its functional form describes a particular type of behavior. In the typical case, for low temperatures, S_T is predicted to have a negative sign. Then, the value of S_T will increase with rising temperature as a function of the ratio T/T_0 , eventually becoming positive after T^* . T_0 is a kind of material constant, describing how strong this temperature dependence is. Finally, the Soret coefficient is expected to reach a saturation value of S_T^∞ for high temperatures. The coefficient S_T^∞ may take on both signs. In most cases, it is positive, as in all examples shown in fig. 1.5a, which also corresponds to an always positive slope. But there are systems in which it takes on negative values, which implies that the switching at T^* is from thermophobic to thermophilic behavior instead and the slope is negative throughout [40].

The Soret coefficient of a specific colloid also depends on the particle radius. Two types of dependence have been found, a quadratic and a linear one. It is so

far unclear where this deviation stems from [41].

It is worthwhile to mention here that many colloids carry charges, and that electrostatics have shown to significantly influence colloidal thermophoresis [42]. Still, this thesis will deal with electrically neutral colloids and solvents as a simpler model system of reduced complexity.

2 Simulation Methods

To describe systems of colloidal microswimmers driven by thermophoresis in computer simulations, the complex interplay of swimmer geometry, hydrodynamics, phoresis, molecular-level interactions, and thermal fluctuations has to be accounted for. The dynamics of colloidal systems take place on mesoscopic time and length scales. Atomistic Molecular Dynamics (MD) is suitable mostly for processes on the nanoscale, both in time and space. A full atomistic description of colloidal systems is computationally therefore very expensive and outside the reach of this method. To circumvent these limitations, coarse-grained methods have been developed, aiming at averaging out fast degrees of freedom while maintaining a description of physical interactions precise enough to study mesoscale problems. For colloidal systems, both hydrodynamics and thermal fluctuations are of considerable relevance and a suitable simulation method needs to account for both of these. Simulation studies in this thesis will use Multi-Particle Collision Dynamics (MPC) [43], a mesoscopic simulation method naturally including both hydrodynamic and thermal effects. In MPC, the fluid is described as a collection of point-like particles that only interact through coarse-grained collisions, which due to its efficiency enables simulation on the necessary time and length scales while still describing correct hydrodynamic interactions [44]. MPC includes thermal fluctuations and heat transport by construction, such that in order to study phoretic effects for colloids in a fluid described by MPC, only a suitable way of thermostatting is necessary. The resulting temperature fields, hydrodynamic flow fields and thereby phoretic effects are not imposed but develop naturally, such that one expects to obtain a precise and complete description of phoretically driven swimmers and their mutual interactions, especially as compared to methods in which driving forces are imposed. This chapter will introduce the prerequisites necessary to perform such computer simulation studies on thermophoretic microswimmers.

2.1 Molecular Dynamics

MD simulations are intended to provide a description of the time-resolved properties of many-particle systems. In MD, it is assumed that the many-particle system under consideration obeys the laws of classical mechanics and the corresponding equations of motion are solved numerically to obtain the system dynamics. Each particle i with mass m_i in the system is defined by its position \mathbf{r}_i and velocity \mathbf{v}_i . Then,

Newton's equation of motion reads as

$$m_i \ddot{\mathbf{r}}_i = \mathbf{f}_i \quad (2.1)$$

with the force given as the derivative of the potential energy E

$$\mathbf{f}_i = -\nabla_{\mathbf{r}_i} E. \quad (2.2)$$

The potential energy E is given by the sum of position-dependent individual contributions of the particles in the system as [45]

$$E = \sum_i u_1(\mathbf{r}_i) + \sum_i \sum_{j>i} u_2(\mathbf{r}_i, \mathbf{r}_j) + \sum_i \sum_{j>i} \sum_{k>j>i} u_3(\mathbf{r}_i, \mathbf{r}_j, \mathbf{r}_k) + \dots \quad (2.3)$$

where u_1 accounts for the effect of an external field and the other terms for two-body- (u_2), three-body- (u_3), and eventually also higher order interactions. The most important contributions stem from the external fields and the pair-wise interactions u_2 , and in many situations it is sufficient to only consider those. When the pair-wise interaction is modeled by some empiric potential adapted to reproduce reference values, it may be regarded as an effective potential that implicitly accounts for higher-order interactions. The choice of a suitable pair-wise interaction potential is a crucial step in performing MD simulations. With one at hand, the equations of motion are then solved numerically. In principle, any numerical method to solve differential equations can be used to this aim. The so-called "velocity-Verlet" algorithm has shown to be an efficient method, suitable both in performance and precision for MD, and it is the one also used in this work. With this algorithm, positions and velocities are updated according to

$$\mathbf{r}_i(t + \delta t) = \mathbf{r}_i(t) + \delta t \mathbf{v}_i(t) + \frac{1}{2m_i} \delta t^2 \mathbf{f}_i(t) \quad (2.4)$$

$$\mathbf{v}_i(t + \delta t) = \mathbf{v}_i(t) + \frac{1}{2m_i} \delta t [\mathbf{f}_i(t) + \mathbf{f}_i(t + \delta t)]. \quad (2.5)$$

Besides accuracy and performance, a relevant criterion for the choice of integration algorithm is energy conservation. Though many higher-order algorithms show much better short-time energy conservation, their long-term drifts are in fact higher than those of the simpler Verlet-type algorithms, which feature only moderate short-time energy conservation but not much long-term drift [46].

2.2 Interaction Potentials

Suspended colloids interact both with each other as well as with the solvent particles [27]. Experimentally, colloid and solvent interact through interaction potentials on the molecular level. These may be, depending on the precise type of atoms or molecules, repulsive (poor solvent) or attractive (good solvent). Always present in

colloid-colloid interactions is a repulsive hard core type of interaction, which describes that the centers of two colloids can not overlap. For deformable colloids, this repulsion might be softer. Another type of repulsion in between colloids occurs when they carry surface charges, these are though frequently screened by the solvent, such that this colloid-colloid interaction is short-ranged repulsive as well. There can also be attractive interactions in between colloids, for example due to coating with polymer brushes in a poor solvent, which makes their overlap favorable and induces a short-ranged attraction. Another way to induce short-range attraction in between colloids is through addition of smaller particles, like short polymers. This will induce a so-called depletion interaction.

Atomistic simulations aim at a very precise and complete reproduction of the physical properties of particular substances at specific conditions, and their predictive capability hinges on the quality of the interaction potentials. In contrast, in a mesoscopic simulation scenario, the precise choice of colloid-colloid and colloid-fluid interaction does not aim to have a unique mapping to physical quantities. It merely has to capture the essential physics of a colloidal system, such that there is a certain degree of freedom in its choice. The main requirement it has to fulfill always is that it needs to capture a repulsive core, while the details of surface interactions will depend on the system of interest.

In this work, colloid-colloid interactions are modeled as steeply repulsive interactions. One might use hard-sphere interactions to achieve this, however, it is in a molecular dynamics context more desirable to use a steeply repulsive hard-sphere like potential that can still be numerically integrated. The main requirement of colloid-solvent interactions is to have a repulsive core as well. They are chosen likewise, though not only as purely repulsive but also including short-ranged attraction. In every case, a Lennard-Jones (LJ) type of potential is used. The most commonly used LJ potential reads

$$U_{\text{LJ,standard}}(r) = 4\varepsilon \left(\left(\frac{\sigma}{r} \right)^{12} - \left(\frac{\sigma}{r} \right)^6 \right) + C, \quad r < r_c \quad (2.6)$$

where r is the pairwise distance, ε describes the strength of the interaction, σ the range, r_c is a cutoff beyond which the interaction is zero and C is a shift. The cutoff r_c could in principle be ∞ , but is chosen such that the relevant part of the interaction is maintained while saving computational effort by not calculating the potential in between far-away particles, where their mutual interaction is vanishing. A typical value for the cutoff eq. (2.6) is $r_c = 2.5\sigma$. Choosing $r_c = 2^{1/6}\sigma$, the attractive part of eq. (2.6) is cut off and one obtains a purely repulsive interaction potential, referred to as the Weeks-Chandler-Andersen (WCA) potential. C is usually chosen such that the potential is zero at r_c to avoid discontinuities in the calculated energies when two particles approach each other from beyond r_c . This is done for every potential interaction used in this work and will from here on not be mentioned explicitly.

To obtain more flexibility in the interactions, one can also tune the exponents in

eq. (2.6) and introduce displacements Δ , arriving at

$$U(r) = \begin{cases} \infty, & r \leq \Delta \\ 4\varepsilon \left[\left(\frac{\sigma}{r-\Delta} \right)^{2n} - \left(\frac{\sigma}{r-\Delta} \right)^n \right] + C & \Delta < r < r_c \\ 0, & r_c \leq r \end{cases} \quad (2.7)$$

where the exponent n now allows to tune softness and steepness, while Δ allows to enlarge the pairwise distance without modifying the form of the potential. Purely repulsive interactions (WCA) are now obtained with $r_c = 2^{1/n}\sigma + \Delta$. When using displacements $\Delta > 0$, the effective diameter of a particle is $s = \sigma + \Delta$ and a parameter set is given as $(s, \Delta, \varepsilon, n, r/a)$ where in the last entry "r" indicates a cutoff leading to a purely repulsive interaction while "a" indicates a choice of cutoff giving the full potential including the attractive part. In the latter case it is cut at the value where the energy equals that of eq. (2.6) with $\varepsilon = 1$ at $r = 2.5\sigma$. The precise value of r_c in this case is given by

$$r_c = \Delta + \left(\frac{1}{2\varepsilon} \left(\varepsilon - \sqrt{\varepsilon(\varepsilon + U_{LJ,\varepsilon=1}(2.5\sigma))} \right) \right)^{-\frac{1}{n}} \sigma, \quad (2.8)$$

which is used in this work for every interaction including the attractive part and will not be explicitly mentioned from this point on. The subsets "cf" will be used to denote colloid-fluid interactions, while "cc" will denote colloid-colloid interactions.

2.3 Mesoscale Simulation Techniques

There are several approaches to describe colloidal mesoscale dynamics in computer simulations. Langevin Dynamics (LD) solve the Langevin equation numerically. A distinction is made to Brownian Dynamics (BD), which also solve the Langevin equation, but in the inertia-free limit [47]. LD and BD are in a sense very similar to classic MD simulations, but including a noise and a friction force. For that reason, LD is also used as a thermostat in MD simulations [48]. Since the solvent is treated implicitly, hydrodynamics do not emerge naturally, but may be included through additional forces based on, for example, the Oseen or Rotne-Prager tensor. When hydrodynamic interactions are included, the method is termed Stokesian Dynamics [49].

Instead of the continuum description of the fluid used in these methods, another approach to treat the problem of the large separation in length and time scales between solvent and solute is to consider the solvent not as atomistically resolved, but to treat larger groups or clusters of fluids as units which move on comparable scales as the solute. These coarsened chunks of fluid are then called "dissipative" particles, and their motion is resolved with the method of dissipative particle dynamics (DPD) [50].

Another approach to resolve mesoscale dynamics of polymers or colloidal suspensions is to employ lattice-based methods. Among these, Lattice Boltzmann (LB)

methods are prominently used. These work by solving the Boltzmann equation on a lattice, employing specific models to treat the collision terms [50].

Multi-Particle Collision Dynamics (MPC) [43], which has also been called stochastic rotation dynamics (SRD) [51] and real-coded lattice gas [52], employs an off-lattice description of coarsened fluid particles which interact through effective collision rules. It has the advantage of including thermal fluctuations by construction in its simplest formulation already, which are crucial in the description of colloidal systems. Due to the method conserving energy locally, thermophoretic effects emerge naturally from it. These features make it a suitable method to describe the fluid in the systems treated in this work.

2.4 Multi-Particle Collision Dynamics

MPC was developed in 1999 by Malevanets and Kapral [43]. The method describes a fluid as a collection of point particles i defined by their positions \mathbf{r}_i , velocities \mathbf{v}_i and mass m_i that do not interact with each other through direct potentials. Fluid particle interactions are instead accounted for in a statistical fashion by coarsening them into multi-particle collisions. At its core, the algorithm consists of two steps, which are illustrated in fig. 2.1. In the streaming step, all particles propagate

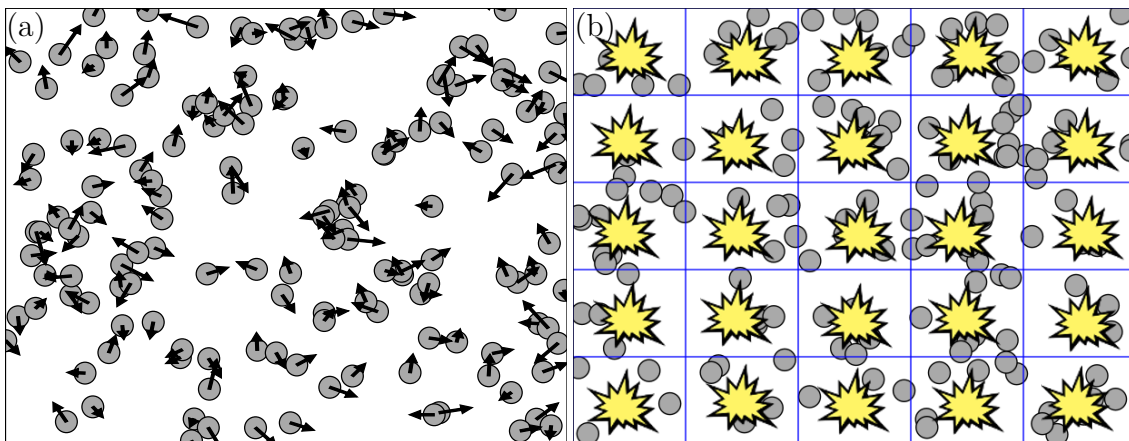


Figure 2.1: Schematics showing the MPC algorithm. In the streaming step **a)**, all particles propagate ballistically. Then, in the collision step **b)**, they are sorted into bins in which multi-particle collisions are performed.

according to their instantaneous velocity for a time h , called the collision time, according to

$$\mathbf{r}_i(t+h) = \mathbf{r}_i(t) + h\mathbf{v}_i(t). \quad (2.9)$$

Then, collisions take place. To perform these, the particles are sorted into bins Ψ of a regular grid of side length a . For each bin, the bin-wise center-of-mass velocity

$\mathbf{v}_{\text{cm}}(\Psi_i)$ is calculated and the velocities of particles inside this bin are rotated around a random axis by an angle α , as [53]

$$\mathbf{v}_i(t+h) = \mathbf{v}_i(t) + \mathcal{R}[\Psi_i(\mathbf{r}_i(t+h)), \alpha] \{ \mathbf{v}_i - \mathbf{v}_{\text{cm}}[\Psi(\mathbf{r}_i(t+h))] \} \quad (2.10)$$

where \mathcal{R} is a rotation matrix and the center of mass \mathbf{v}_{cm} of a bin, or collision cell, is calculated as

$$\mathbf{v}_{\text{cm}}[\Psi(\mathbf{r}_i(t+h))] = \frac{\sum_{k \in \Psi} \mathbf{v}_k}{N_{\Psi,t}}. \quad (2.11)$$

with $N_{\Psi,t}$ being the number of particles in bin Ψ at time t . This collision rule conserves linear momentum, mass, and energy and has been shown to be a computationally very efficient way to obtain correct hydrodynamics [44, 54]. However, in its basic formulation, it does not conserve angular momentum. There exist methods to include angular momentum conservation into MPC, at the cost of longer computation times. In many cases, it is not necessary to include angular momentum conservation [55], though specific scenarios where its importance has been shown were discussed [44].

Several formulations for the rotation matrix \mathcal{R} exist. In two-dimensional systems, one rotates by either $+\alpha$ or $-\alpha$, choosing the sign randomly. Transferring this to three dimensions, one may choose a rotation by $\pm\alpha$ around one of the three main axes, arriving at six possible rotation matrices out of which one is chosen randomly for each collision cell. As the axes are fixed, this collision rule may lead to some isotropy due to the underlying lattice. A modified version constructing a completely random axis for each bin around which the rotation is performed was also developed [56] and is used in this work to minimize up to a negligible degree any spurious isotropy of the imposed grid.

The applied grid however does limit the achievable resolution, and may also introduce unphysical behavior when the mean-free path of MPC particles is lower than the side length of collision cells a . Then, particles may interact with the same partners in multiple successive steps and Galilean invariance is broken. A method to restore Galilean invariance and enable smaller collision times h is to introduce a grid-shifting procedure [57]. With this, the grid is displaced before each collision step by a random shift $[-a/2, a/2]$ or likewise $[0, a]$, on average randomizing the collision partners of each particle and restoring Galilean invariance for arbitrary low mean-free paths.

Simulation units in MPC are defined by the length a , the mass m and the energy $k_B T$, which are typically set to one and constitute the basis for all other units. This choice implies that time is scaled with $a\sqrt{m/(k_B T)}$, so velocities are for example given in units of $\sqrt{k_B T/m}$, diffusivity and kinematic viscosity in $a\sqrt{k_B T/m}$ and density referring to a unit area or volume of a^d with d the dimensionality. These are the units employed in this thesis and will not be explicitly specified from here on.

Independent quantities that determine the MPC fluid behavior are the chosen collision time h , the average number of particles per cell $n_{\text{MPC}} = \langle N_{\Psi}/a^d \rangle$ and the rotation angle α as well as the system size. Simulation boxes are typically quadratic or cubic with edge length L .

Besides the basic formulation presented so far, several variants of the MPC algorithm have been developed. Anderson-MPC [58] and Langevin-MPC [59] provide thermostats directly incorporated into the collision operator \mathcal{R} , for example to account for changes in the system's energy induced by applying external forces. Anderson-MPC can be modified to also conserve angular momentum.

2.4.1 Introduction of Temperature Gradients

Studies on the inclusion of temperature gradients into the MPC method have been performed by Lüsebrink and Ripoll [60]. For confined systems, these authors considered two approaches. One is to rescale the temperature of fluid particles in short layers close to the confining walls to different temperatures, a lower one T_c and a higher one T_h . The second one considers virtual particles. When a random shift procedure is employed, the treatment of confining walls requires additional attention, as collision cells may overlap the walls and are then only partly filled. As the average particle density in collision cells determines the physical properties of the MPC fluid, this leads to deviations at the boundaries. To overcome this problem, it was proposed to include virtual particles in these cells overlapping boundaries, as many as necessary to restore the average density for the cell [61]. Their velocities are drawn randomly from a Maxwell-Boltzmann distribution corresponding to the average temperature of the system. These virtual particles can therefore also easily be used for thermostatting purposes. If one wishes to obtain a temperature gradient in between two confining walls it is possible to draw the virtual particles velocities from two Maxwell-Boltzmann distributions at reduced and elevated temperature. Both described methods lead to stable linear temperature gradients at some distance from the wall.

For periodic systems, a different approach has to be taken. For MPC, it is also possible to use the algorithm of Müller-Plathe for non-equilibrium molecular dynamics [62]. In it, two slabs inside the periodic box are defined. Then, the velocities of the hottest particle or particles in one layer, considered cold, and the coldest particle in the other layer, considered hot, are exchanged. The method conserves total energy and momentum, and is suitable as well for MPC simulations, leading to stable linear temperature gradients as shown in [60].

2.4.2 Coupling to Colloidal Dynamics

There exist multiple ways of coupling the MPC fluid to the dynamics of immersed large particles. One straightforward method is to treat larger particles as "heavy" fluid particles, i.e. having a larger mass than the fluid particles, and letting them take part in the collision step. This variant is called MPC-coupling and has shown

to be a very efficient model for example when applied to linear polymers, rods, or star polymers in shear flow [63], among others. Another possibility is to describe the colloid-solvent interaction through introduction of direct pair-wise interaction potentials as done in MD [64], which, though being computationally far more expensive, has the advantage of allowing a more precise and tunable description of interaction properties. This combination of MPC with MD is called Multi-Particle Collision Dynamics coupled to Molecular Dynamics (MPC-MD). It is the approach adapted in this work, as the molecular interactions determine the response of colloids to temperature gradients.

2.4.3 MPC Fluid Properties

The MPC fluid has the equation of state of an ideal gas,

$$pV = n_{\rho}k_{\text{B}}T. \quad (2.12)$$

The MPC particles' velocities follow a Maxwell-Boltzmann distribution. Their mean-free path is given by $h\sqrt{k_{\text{B}}T/m}$. Analytic predictions for the transport properties of an MPC fluid have been calculated based on kinetic theory for the stochastic rotation rule of eq. (2.10) [44, 65, 66] and have been shown to lead to very good agreement to what is obtained in simulation measurements [44, 67]. The transport coefficients of the MPC fluid have a kinetic contribution, referring to particles carrying momentum along with them as they move through space. The other contribution is a collisional one, referring to momentum being transported through the fluid by interactions of particles rather than their motion. Table 2.1 summarizes the analytic expressions used to characterize fluid properties in this work.

Table 2.1: Analytic predictions, up to $\mathcal{O}(1/n_{\text{MPC}})$ for kinetic and $\mathcal{O}(1/n_{\text{MPC}}^2)$ for collisional contributions, for the kinematic viscosity ν , the thermal diffusivity D_T and the self-diffusion coefficient D_f of an MPC fluid. n stands for n_{MPC} in this table. Taken from [44].

	d	kinetic ($\times k_{\text{B}}Th/(2m)$)	collisional ($\times a^2/h$)
ν	2	$\frac{n}{(n-1+\exp[-n])\sin^2(\alpha)} - 1$	$\frac{n-1+\exp[-n]}{6dn}(1 - \cos(\alpha))$
	3	$\frac{5n}{(n-1+\exp[-n])[2-\cos(\alpha)-\cos(2\alpha)]} - 1$	
D_T	2	$\frac{d}{1-\cos(\alpha)} - 1 + \frac{2d}{n} \left[\frac{7-d}{5} - \frac{1}{4} \csc^2(\alpha/2) \right]$	$\frac{1-1/n}{3(d+2)n} [1 - \cos(\alpha)]$
	3		
D_f	2	$\frac{dn}{[1-\cos(\alpha)](n-1+\exp[-n])} - 1$	-
	3		

Knowledge of the transport coefficients allows characterization of the fluid in terms of hydrodynamic numbers. The MPC parameters used in this work are, besides the choice of simulation units determining $a = 1$, $m = 1$, and $k_{\text{B}}T = 1$, typically

chosen as $\alpha = 120^\circ$, $n_{\text{MPC}} = 10$ and $h = 0.1$. These values are used for the theoretical predictions in the following. This choice determines the fluid properties as the diffusion coefficient $D_f = 0.06$, the kinematic viscosity $\nu = 0.79$ (or dynamic viscosity $\mu_d = \rho\nu = 7.9$) and the thermal diffusivity $D_T = 0.154$ (or thermal conductivity $k_T = \rho c_p D_T = 3.85$) [57, 60].

In order to compare simulation units with real units used in experiments, dimensionless numbers are of great importance. The five dimensionless numbers most relevant to the systems treated in this thesis are therefore discussed in the following.

The *Schmidt number* $Sc = \nu/D_f$ characterizes the rate of diffusive momentum transfer to that of diffusive mass transfer [54]. Gases typically have Schmidt numbers around 1, such that momentum transfer is dominated by the diffusion of mass. Liquids mostly have high Schmidt number in the range of hundreds, such that momentum transfer is dominated by inter-particle interaction processes, i.e. collisions. In order to obtain hydrodynamic behavior corresponding to a liquid-like state, a high Schmidt number is called for. MPC is able to reach these high Schmidt numbers, but at the cost of rather long simulation times. On the other hand, as pointed out by Padding and Louis [54], D_f does not enter directly the Navier-Stokes equations for colloids interacting with the fluid through a potential or stochastic boundary conditions. In that case, a proper separation of time-scales is given when $D_{\text{colloid}} \ll D_f$ and liquid-like hydrodynamics should be obtained. In this work, $Sc \approx 13$ is used, which is smaller than that of most liquids, but still ensuring this separation of time scales, which has been shown to be a suitable and efficient choice to model hydrodynamic interactions [68, 69].

The *Reynolds number* $Re = v_c l_c / \nu$ measures the relative importance of inertial to viscous forces. v_c is a typical velocity, in the context of microswimmers for example the flow velocity of the MPC fluid or a colloid's velocity. l_c is a typical length scale, it could be for example the collision box size a or a colloid's diameter. To describe colloidal dynamics taking place at low Reynolds numbers, in the so-called Stokes regime, it should be accordingly chosen low. MPC will resolve hydrodynamics for any Reynolds number chosen, such that its choice is not a question of the method but rather one depending on the system under consideration. For choices of $Re < 1$, the assumption of Stokes behavior leads to good agreement of predicted and measured flow fields of thermophoretic swimmers [25].

Compressibility effects are measured by the *Mach number* $Ma = v_c / c_f$, where the speed of sound c_f is given by $c_f = \sqrt{(5/3)(k_B T / m)}$. Typically, the Mach numbers of fluids are very low. Coarse-grained particle-based simulation methods most often lead to higher Mach numbers, as the coarsened particles describing chunks of fluid usually have a higher mass than that of the underlying molecules and collide much less frequently, making the methods prone to compressibility artifacts. For the colloidal swimmers under consideration in this work, typical velocities are of order 10^{-2} , leading to Mach numbers around $Ma \approx 10^{-2}$ which should be small enough to avoid compressibility artifacts, especially since these typically scale with Ma^2 [54].

The *Peclet number* $Pe = v_c l_c / D_{\text{colloid}}$ characterizes the importance of convective over diffusive transport for immersed particles [54]. Alternatively, for a self-propelled colloidal particle, it may also characterize the importance of propulsion over noise, taking the definition

$$Pe = v_c / (D_{\text{colloid}} l_c) \quad (2.13)$$

where D_{colloid} is the colloid's diffusion coefficient and l_c its characteristic length scale [70]. Typical values of the Peclet number of experimentally synthesized phoretic Janus particles are in the range 5–200, which is also aimed for in this work.

In situations where thermal processes play a role, the *Prandtl number* $Pr = \nu / D_T$ characterizes the importance of viscous over thermal diffusion. A typical value for water at 15°C is $Pr = 7.82$ [71]. The MPC fluid's Prandtl number is ca. 6 for the simulation parameters chosen in this work, which closely corresponds to the liquid-like regime aimed for.

2.5 Implementation of MPC-MD in LAMMPS

LAMMPS is a versatile, open-source framework for molecular simulation, in its core aimed at classic molecular dynamics simulation, but suitable as well for coarse-grained, mesoscopic, or continuum scenarios [72]. A parallel implementation of the MPC algorithm in its basic formulation is available in LAMMPS, with implementation details discussed in [53]. It features an MPI-based domain-decomposition parallelization scheme that has shown good scaling properties on a Cray XT3 high-performance system.

In this work, it is aimed for to perform large-scale simulation on active colloidal systems based on the MPC-MD algorithm. LAMMPS offers MPI-parallelized MD and basic MPC, but not an efficient coupling between the two to enable MPC-MD simulations. This, along with a variety of other features such as specific thermostats and flow field measurements, was implemented in the scope of this work into LAMMPS and all simulations are performed with it.

The most prominent differences and additional features of the code used for this work are summarized in the following. In the original implementation, the collision step is done with a fixed angle of $\alpha = 90^\circ$ and using a collision operator \mathbf{R} picking one out of six rotations around fixed axes. Within this work, it was adapted to feature a variable angle α and using a random axis to perform rotations with. The existing framework of LAMMPS provided in principle the possibility to run MPC-MD simulations, albeit at the cost of high computation times as no distinction could be made between MPC particles that interact explicitly with the colloids and those that do not, requiring then to use the same time step for propagation of both the interacting and the, typically many more, non-interacting MPC particles. Within this work, an efficient routine to distinguish these two types

was implemented, allowing separate treatment and regaining the original efficiency of the MPC simulation method also in the context of MPC-MD. Furthermore, many functionalities of standard MD hinder performance when not accounting for the ideal-gas nature of non-interacting MPC particles, which in many cases means not including them inside the computational routine. For example, just checking with an if-statement whether a non-interacting MPC particle needs to be considered in the MD neighbor list creation can severely decrease performance due to the sheer number of non-interacting MPC particles. All relevant MD functionalities of LAMMPS were then, if necessary, modified to avoid considering the non-interacting particles.

Strong scaling results of this implementation of MPC-MD on the supercomputer JURECA [73] are shown in fig. 2.2. Parallel efficiency is around 90 % for a variety

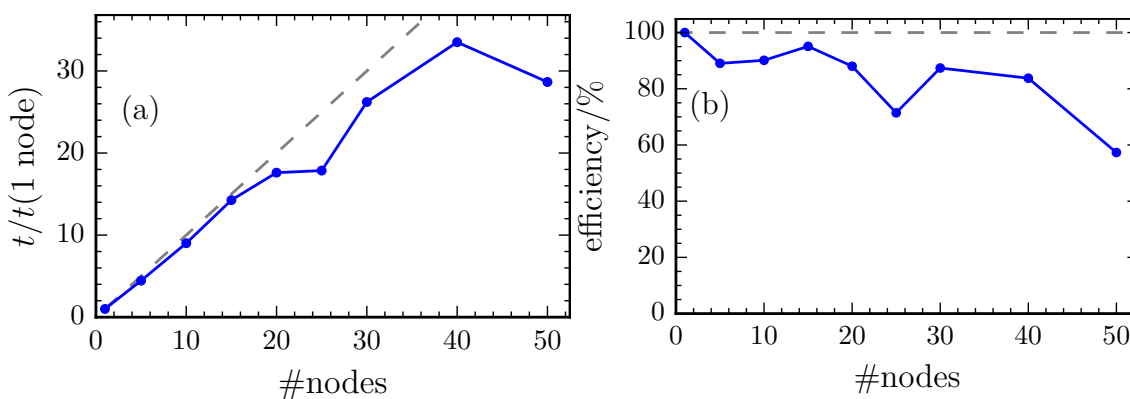


Figure 2.2: Strong scaling behavior of the implementation of MPC-MD in LAMMPS on the supercomputer JURECA [73] in terms of speedup (a)) and parallel efficiency (b)). This test was performed for a system with fixed size of 500 dimer swimmers, and 9.0×10^7 MPC particles (this corresponds to $L = 211$ collision boxes per spatial direction). Data is normalized to 1 node (= 24 cores without hyper-threading).

of reasonable node numbers, then drops off at some point where the domains each processor works on get too small and communication costs start to become dominant. The system shown here is very big and demanding in terms of the MD part. Petersen et al. reported super-linear scaling for their implementation of pure MPC in LAMMPS [53], which was attributed to memory effects on the CPU architecture, such as the list of particles fitting into cache. This has also been observed on JURECA for pure fluid simulations as well as for those with a smaller MD part, such as single colloids in temperature gradients.

3 Theoretical Approach to Thermophoresis

In this chapter, two approaches to phoresis are discussed, with the aim to obtain expressions for the thermal diffusion factor α_T and Soret coefficient S_T in the context of thermophoresis. One route is to obtain the force on a colloid in a gradient through direct evaluation of the force, the other is to find an expression for the phoretic slip velocity. Based on the notion of thermophoresis stemming from the combination of a temperature gradient and the corresponding density gradient, analytic expressions are established for both approaches and tested against simulation results. These are then used to explain the size and temperature dependence of the Soret coefficient observed in simulation studies.

3.1 Phoretic slip velocity

The motion of liquids on the microscale, in the low Reynolds-number regime of an incompressible fluid, is governed by the Stokes equation eq. (1.5), $\mu_d \nabla^2 \mathbf{v} = \nabla p - \mathbf{f}$, where μ_d is the viscosity, \mathbf{v} the fluid velocity field, p the pressure and \mathbf{f} any force density exerted on the fluid [42, 74]. Consider the case of a large spherical particle with radius R suspended in the fluid. The force that particle exerts on the fluid has a range of interaction B , supposed to be short, i.e. $B \ll R$. Then, the Stokes equation can be solved taking advantage of the boundary layer approximation. The particle surface is taken to be flat in the range where \mathbf{f} is significantly large and one can solve the Stokes equation in a local coordinate system (x_l, z_l) attached to the surface, as sketched in fig. 3.1. The Stokes equation in this coordinate system is now dependent only on x_l and z_l . The perpendicular component of the fluid velocity v_{z_l} should vanish close to the particle and the parallel velocity v_{x_l} should not depend on x_l , but only on z_l . This parallel velocity will vary according to the particle-fluid interaction inside the boundary layer and take a constant value outside $v_{x_l}(z_l \geq B) = v_B = \text{constant}$. The two components of the Stokes equation can therefore be simplified to

$$0 = \frac{dp}{dz_l} - f_{z_l} \tag{3.1}$$

$$\mu_d \frac{d^2 v_{x_l}}{dz_l^2} = \frac{dp}{dx_l} - f_{x_l}. \tag{3.2}$$

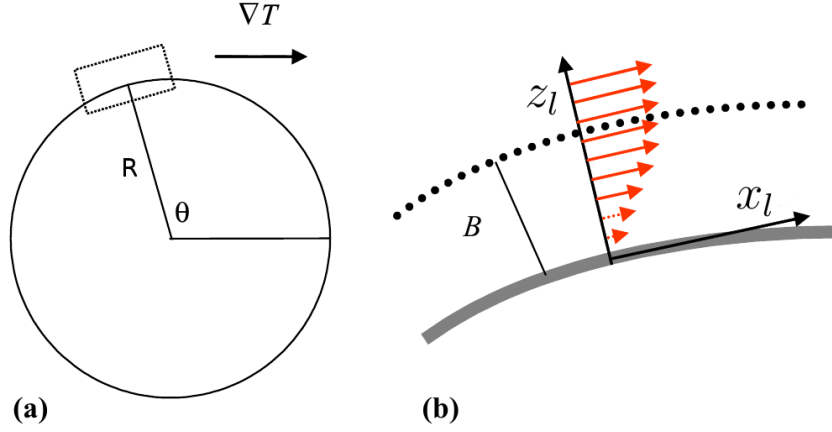


Figure 3.1: Local coordinate system attached to the colloidal surface. Taken from [42].

The integral of eq. (3.1) gives the hydrodynamic excess pressure p . From eq. (3.2), one can obtain an expression for the slip velocity at the colloidal surface. If the slip velocity is known, the velocity of the particle can be calculated, as well as the flow field in the surrounding fluid. Equation (3.2) is integrated twice to obtain an expression for the slip velocity. The first integral disappears at the upper boundary since there are no pressure gradients in bulk fluid, so $dv_{x_l}/dz_l|_{z_l=B} = 0$, and the second integral results, using that $v_{x_l}|_{z_l=0} = 0$ (since there is no slip at the solid surface), in

$$v_{x_l} = -\frac{1}{\mu_d} \int_0^{z_l} dz'_l \int_{z'_l}^{\infty} dz''_l \left(\frac{dp}{dx_l} - f_{x_l} \right), \quad (3.3)$$

which can be rearranged using integration by parts and evaluated at $z_l = B$ to give [42, 75]

$$v_B = \frac{1}{\mu_d} \int_0^B dz_l z_l \left(f_{x_l} - \frac{dp}{dx_l} \right). \quad (3.4)$$

This equation provides a general description of slip velocity at the boundary layer of a colloidal surface, originating in an external force and a surface gradient of pressure. The pressure is linked to the colloid-fluid interaction potentials in order to obtain expressions for a specific realization of diffusio- and thermophoretic effects.

3.2 Diffusiophoresis

Diffusiophoresis describes the phoretic effect resulting from a gradient in density or concentration around a colloid. This may be a gradient in a single fluid species, or

a gradient in a mixture of more than one fluid species. The latter case is used for example in simulation models of chemical swimmers, where one catalytic site converts a fluid species A to another fluid species B , thereby producing a concentration gradient in both [16].

3.2.1 Slip Velocity

The excess pressure p in the boundary layer of a particle interacting with the solvent through a central potential U is given by [42]

$$p = \rho k_B T \left(\exp\left[-\frac{U}{k_B T}\right] - 1 \right). \quad (3.5)$$

Since this kind of interaction potential has no parallel component, $U = U(z_l)$, f_{x_l} in eq. (3.2) is zero, and accordingly also in eq. (3.4). The slip velocity for the diffusiophoretic case, where there is a non-constant density ρ (or concentration c) of neutral solvent species around a colloid, follows when the density ρ of solvent particles depends on x_l . Then, eq. (3.4) is given for diffusiophoresis, with $\frac{dp}{dx_l} = \frac{d\rho}{dx_l} k_B T \exp\left[-\frac{U}{k_B T}\right] - \frac{d\rho}{dx_l} k_B T - \frac{dU(z_l)}{dx_l} \rho \exp\left[-\frac{U}{k_B T}/(k_B T)\right] = \frac{d\rho}{dx_l} k_B T (\exp\left[-\frac{U}{k_B T}\right] - 1)$, by [74]

$$v_B = -\frac{k_B T}{\mu_d} \frac{d\rho}{dx_l} \int_0^B dz_l z_l \left(\exp\left[-\frac{U}{k_B T}\right] - 1 \right). \quad (3.6)$$

For a specific application, this equation needs to be written in the appropriate coordinate system for the system under investigation. For example, for a sphere with outer edge \bar{R} , a density gradient in z -direction and spherical polar coordinates, in which the polar angle $0 < \theta < \pi$ is measured from the z -axis, one obtains

$$\mathbf{v}_B(\bar{R}, \theta) = -\frac{k_B T}{\mu_d} \nabla_{\theta} \rho \int_0^B dz_l z_l \left(\exp\left[-\frac{U}{k_B T}\right] - 1 \right). \quad (3.7)$$

This can be written in a more concise notation, since all terms but $\nabla_{\theta} \rho$ are constant. Introducing $\kappa_{\rho} = (k_B T / \mu_d) A_{\rho}$ with

$$A_{\rho} = \int_0^B dz_l z_l \left(\exp\left[-\frac{U}{k_B T}\right] - 1 \right), \quad (3.8)$$

eq. (3.7) read as

$$\mathbf{v}_B(\bar{R}, \theta) = -\kappa_{\rho} \nabla_{\theta} \rho(\bar{R}, \theta). \quad (3.9)$$

This was for example used in the continuum model description of dimeric colloidal swimmers driven by diffusiophoresis [76].

3.2.2 Phoretic Force

An alternative way to calculate the propulsion velocity of a colloid in a density gradient is possible by directly evaluating the interaction potential, obtaining the force in direction of the gradient (taken to be in z) by solving

$$f_z = \hat{\mathbf{z}} \cdot \mathbf{f} = \int d\mathbf{r} \rho \frac{\partial U(r)}{\partial \mathbf{r}} (\hat{\mathbf{z}} \cdot \hat{\mathbf{r}}). \quad (3.10)$$

Here, $\hat{\mathbf{z}}$ is the unit vector in direction of the gradient and \mathbf{f} the force on the colloid. The density ρ must depend on z , and for pairwise colloid-fluid interactions also on the pairwise distance r , which is $r = |\mathbf{r}|$ when the colloid is taken to be at the origin. For an ideal gas, the solvent density distribution will follow the interaction potential according to

$$\rho(r) = \bar{\rho} \exp\left[-\frac{U(r)}{k_B T}\right] \quad (3.11)$$

when there is no gradient, where the unperturbed equilibrium density is denoted $\bar{\rho}$. For an existing gradient, one may write

$$\rho(r, z) = \rho(z) \exp\left[-\frac{U(r)}{k_B T}\right], \quad (3.12)$$

where $\rho(z)$ describes the density considering only the effect of the gradient. With this density profile $\rho(r, z)$, eq. (3.10) can be solved (numerically) to obtain the propulsion force f_z of the colloid. The friction coefficient ζ relates this force to the colloid's velocity by $v_z = \zeta f_z$. Such an approach was for example used in [77].

3.3 Thermophoresis

3.3.1 Force on a Colloid

In this section, an approach to an analytic microscopic theory for thermophoretic interactions is presented, that can be used to predict the thermophoretic properties of colloids in MPC-MD simulations. Conceptually, it aims at obtaining expressions for both the fluid temperature distribution and the fluid density distribution to apply the idea of eq. (3.10) to the scenario of thermophoresis. The fluid density distribution needs to account for both its dependence on temperature as well as on the colloid-fluid interaction potential.

The starting point for this calculation is knowing that MPC has an ideal gas equation of state, $pV = n_\rho k_B T$. In the work of Lüsebrink and Ripoll, the effect of temperature gradients on the MPC fluid has been extensively studied [60]. Of specific interest for this work is that for a system with dimensions L_x, L_y, L_z , and a temperature gradient $\nabla_z T$ in z -direction, the temperature gradient in between

a cold layer at temperature T_c and a hot layer at temperature T_h is linear and constant everywhere. The temperature distribution can thus be written as

$$T(z) = T_c + \frac{T_h - T_c}{L_z} z = T_c + \nabla_z T z. \quad (3.13)$$

Due to the ideal gas nature of the MPC fluid, the particle number density ρ is position-dependent and follows the temperature gradient, so $\rho = \rho_T(z) = n(z)a^3/V$ with a the MPC length scale, $n(z)$ the number of particles at z and V the box volume. With the ideal gas law, it can then be written as

$$\rho_T(z) = \frac{p}{k_B T(z)}. \quad (3.14)$$

Using that the total number of fluid particles N is constant, as expressed by $\int_V d^3r \rho(z) = N$, one obtains

$$p = \bar{\rho} \frac{k_B(T_h - T_c)}{\ln(T_h/T_c)}, \quad (3.15)$$

where $\bar{\rho} = N/V$ is the average number density in the system. With these, explicit analytic expressions for both the temperature and the density profile are known. Additionally, the expression for the density profile may also be linearized to [60]

$$\rho_T(z) = \bar{\rho} \left[1 - \frac{\nabla_z T}{T} \left(z - \frac{L_z}{2} \right) \right]. \quad (3.16)$$

This form has the advantage that no volume has to be specified for the calculation, but it will only give a good approximation for small temperature gradients. Additionally, taking the derivative with respect to z , one may write the linearized density gradient as

$$\nabla_z \rho = -\frac{\bar{\rho}}{T} \nabla_z T. \quad (3.17)$$

An example for the temperature and density profiles obtained in this setup is illustrated in fig. 3.2a, highlighting also the feasibility of the linear approximation in the typical scenario of small gradients.

As a next step, consider a measurement aimed at obtaining the dimensionless thermal diffusion factor α_T , which is the proportionality factor that linearly relates the force experienced by a colloid located in a temperature gradient to the strength of this gradient through [35]

$$\mathbf{f}_T = -\alpha_T k_B \nabla T. \quad (3.18)$$

In the context of MPC-MD simulations, a colloid is placed in between a cold and a hot reservoir, at temperatures T_c and T_h [35]. The resulting temperature distri-

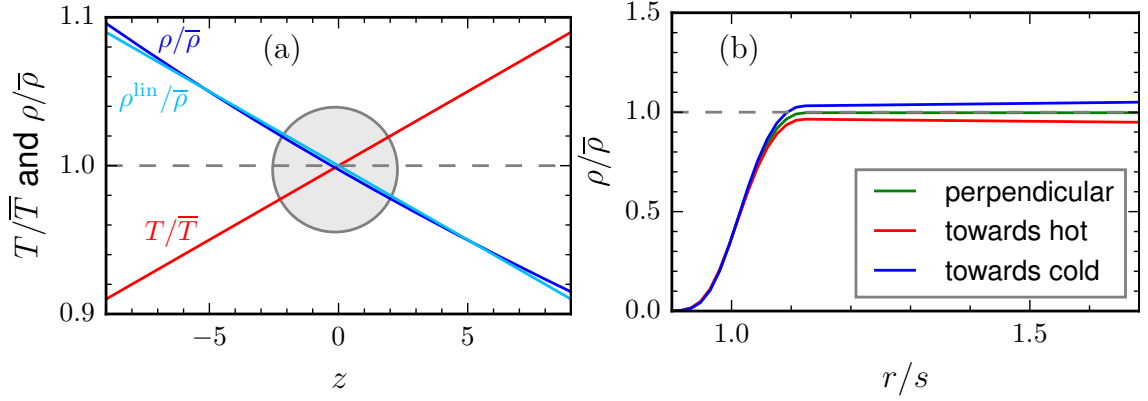


Figure 3.2: **a)** Fluid temperature distribution according to eq. (3.14) (red) for a temperature gradient of $\nabla_z T = 0.01$ in a cubic box with side length $L = 18.0$. The corresponding fluid density distribution according to the full expression of eq. (3.14) is shown in dark blue and the linearized version of eq. (3.16) in light blue. The position of the colloid is sketched with a gray circle. **b)** shows the fluid density distribution according to eq. (3.20) for the same setup, but measured radially from the center of a colloid with radius $s = 3$, described by a purely repulsive potential, in direction perpendicular, along and against the temperature gradient.

bution may show a temperature jump in between the temperature of the boundary and the fluid directly at the boundary, but becomes steady and linear farer away from the reservoirs. α_T can then, for a fixed colloid, straightforwardly be obtained by measuring both the resulting resulting temperature gradient and the resulting phoretic force. Alternatively, α_T might also be extracted from the motion of a colloid freely moving in the temperature gradient. In the analytical approach outlined here, one chooses instead an average temperature \bar{T} and a temperature gradient ∇T , without explicit specification of boundaries.

The scenario of a colloid located in a temperature and density gradient, as sketched in fig. 3.2a, includes several aspects:

1. There is a specific colloid-fluid interaction.
2. There is a temperature gradient.
3. There is a density gradient in response to the temperature gradient.
4. The density distribution will also be influenced by the colloid-fluid interaction.
5. The colloid will induce a flow field.

The temperature and density fields due to the temperature gradient are known. The density distribution $\rho_{\text{colloid}}(r)$ at distance r around a spherical colloid interacting with the MPC fluid through a pairwise potential U is given by

$$\rho_{\text{colloid}}(r) = \bar{\rho} \exp\left[-\frac{U(r)}{k_B T}\right]. \quad (3.19)$$

The full expression for the density distribution that includes both the effect of a temperature gradient as well as that of the colloid then results as

$$\rho_{\text{complete}}(r, z) = \rho_T(z) \exp\left[-\frac{U(r)}{k_B T(z)}\right]. \quad (3.20)$$

The temperature gradient induces an asymmetry in the fluid densities within the interaction volume of the colloid, which is illustrated in fig. 3.2b. Equation (3.20) involves two main approximations, namely that the density and temperature gradients are small, such that the non-equilibrium density and temperature distributions can be expressed as the respective equilibrium distributions plus some additional perturbation terms. This can be seen more clearly when the inhomogeneities in temperature and density are expressed in terms of small perturbations $\Delta\rho$ and ΔT to the equilibrium values \bar{T} and $\bar{\rho}$, such that eq. (3.20) reads

$$\rho(r, z) = (\bar{\rho} + \Delta\rho) \exp\left[-\frac{U(r)}{k_B(\bar{T} + \Delta T)}\right] \quad (3.21)$$

This can be linearized by Taylor expanding, using that for small x , $1/(1+x) \approx 1-x$ and $\exp[x] \approx 1+x$, obtaining

$$\begin{aligned} \rho = & \bar{\rho} \exp\left[-\frac{U}{k_B \bar{T}}\right] + \Delta\rho \exp\left[-\frac{U}{k_B \bar{T}}\right] \\ & + \frac{\Delta T}{\bar{T}^2} \frac{U \bar{\rho}}{k_B} \exp\left[-\frac{U}{k_B \bar{T}}\right] + \frac{\Delta\rho \Delta T}{\bar{T}^2} \frac{U}{k_B} \exp\left[-\frac{U}{k_B \bar{T}}\right], \end{aligned} \quad (3.22)$$

which recovers the equilibrium distribution in the limit of no perturbations, i.e. $\Delta T = 0$ and $\Delta\rho = 0$. This linearized version is only shown here to clarify the approximations, in the numeric calculations the full expression of eq. (3.20) is used.

For a given temperature and density distributions, an expression for the force on the colloid can now be obtained. For symmetry reasons, only the z component, i.e. the component along the temperature gradient, is of interest. The resulting expression in the context of thermophoresis is equivalent to eq. (3.10) with temperature dependent terms and reads

$$\hat{\mathbf{z}} \cdot \mathbf{f} = \int d\mathbf{r} \rho_{\text{complete}}(r, z) \frac{\partial U(r, T(z))}{\partial \mathbf{r}} (\hat{\mathbf{z}} \cdot \hat{\mathbf{r}}). \quad (3.23)$$

This expression is integrated numerically, leading to a value for the thermophoretic force $f_T = \hat{\mathbf{z}} \cdot \mathbf{f}$. Since the temperature gradient ∇T is for this calculation chosen at the beginning, one directly obtains $\alpha_T = -f_T/\nabla T$. For a single colloid in a temperature gradient, the system is cylindrically symmetric, which can be made use of in the numeric evaluation of eq. (3.23).

Conceptually, the underlying interpretation of thermophoresis is illustrated in the sketch in fig. 3.2a. The phenomenon is interpreted as the combined effect of

a density and temperature gradient. The temperature gradient along with the colloid-fluid interaction potentials determines the density distribution, leading to a diffusio-phoretic contribution evident in the position-dependent density. The thermophoretic contribution is included in the position-dependent temperature, that in the force calculation weighs the interaction potential spatially dependent through the Boltzmann factor $1/(k_B T(z))$. A similar approach to obtain α_T was taken by Lüsebrink, but led to systematic deviations [41].

3.3.1.1 Comparison to Simulation

In simulations, the thermal diffusion coefficient α_T can be measured using two schemes [35]. In both of them, the colloid is put into the center of a fluid with a temperature gradient. Employing the so-called Single-Particle Thermal Diffusion Algorithm (SPTA), the colloid is held near its initial position using a spring, and its averaged displacement is related to the thermophoretic force. For pairwise analytic potentials, it is also possible to directly measure the force on a fixed colloid. The second method, which will be referred to as the v_T scheme, does not fix the colloid, but measures its drift velocity and relates it to α_T based on eq. (1.37), through $\alpha_T \approx -v_T \bar{T} / (D \nabla_g T)$ where ∇_g is the derivative in direction of the temperature gradient. This approach requires additional knowledge of the colloid diffusion coefficient D . The two approaches have been shown to lead to nearly identical results [35].

The analytical predictions of eq. (3.23) are compared to simulation results of Lüsebrink et al. [35], who measured α_T using both described methods. The calculated values are given in table 3.1 and are higher than the measured ones, except for the simulation value using a repulsive LJ potential with a colloidal radius $s = 1$. Comparisons are made to the SPTA method in simulations, as more simulation values are available for it and it is closer to the discussed theory in terms of methodology. The average deviation in between predicted and simulated values is ca. 33 ± 12 %, always overestimating the simulation values. All qualitative features are captured however, i.e. the sign depending on the employed potential interaction as well as the trends in obtained values of α_T upon variation of s . The case of small colloids with $s = 1$ is left out in this and the following discussion, as using $s < 2$ in MPC-MD simulations has been shown to lead to deviations from the expected hydrodynamic behavior [54], such that these simulation results are included for completeness, but care has to be taken in drawing conclusions from them.

3.3.1.2 Correction for Finite Size Effects

As discussed by the authors of [35], the measurements of α_T in simulations are significantly influenced by finite size effects. These finite size effects manifest themselves in the presence of a constant backflow of fluid from the boundaries, which compensates the flow induced by the colloid, ensuring that no total net flux is present. The phoretic force will make the colloid drift into one direction, accompanied by a fluid flow in the opposite way. For a fixed particle, which is the case

Table 3.1: Comparison of the evaluation of eq. (3.23), or equivalently eq. (3.34), (α_T^a) to simulation measurements of Lüsebrink et al. [35] using the SPTA scheme (α_T^{SPTA}) and the v_T scheme ($\alpha_T^{v_T}$). α_T^c refers to predicted values including a correction for backflow in simulations. Deviations are given for α_T^c with respect to α_T^{SPTA} . Results obtained using eq. (3.34) match those of eq. (3.23) in every case. The employed colloid-fluid interaction potentials correspond to eq. (2.7) with $(s, 0, 1, 6, r)$ (rep) and $(s, 0, 1, 48, a)$ (att).

Potential	s	α_T^a	α_T^c	α_T^{SPTA}	$\alpha_T^{v_T}$	deviation / %
rep	1	-4.64	-3.61	-5.7	-5.0	-36.7
rep	2	-37.12	-28.86	-29	-24	-0.5
rep	3	-125.10	-97.30	-104	-120	-6.4
rep	4	-295.97	-230.20	-243	-258	-5.3
att	1	10.54	8.20	7.0		17.1
att	2	84.36	65.61	65		0.9
att	3	284.57	221.3	197		12.4
att	4	674.05	524.26	440		19.1

considered in the analytic predictions, the colloid works as a pump. The accompanying flow field for the flow field around a fixed colloid in a temperature gradient is given, when no boundaries are present, by [68]

$$\mathbf{v}_{\text{fluid}}(\mathbf{r}) = -\frac{1}{8\pi\mu_d r} (\hat{\mathbf{r}}\hat{\mathbf{r}} + \mathbf{I}) \cdot \mathbf{f}_T + \frac{R^2}{8\pi\mu_d r^3} (3\hat{\mathbf{r}}\hat{\mathbf{r}} + \mathbf{I}) \cdot \mathbf{f}_T, \quad (3.24)$$

where R is the particle radius, μ_d the dynamic viscosity of the solvent, $r = \mathbf{r}/|\mathbf{r}|$, $\hat{\mathbf{r}} = \mathbf{r}/r$ and \mathbf{I} the unit tensor. The backflow from the boundaries is necessarily opposed to the main flow direction. It has been shown in the studies of Yang and Ripoll that the effect of this backflow is well captured by assuming it as constant, such that the flow field can be calculated assuming no boundaries and its magnitude then shifted downwards by the value at the boundary [68]. Figure 3.3 shows their measurements and analytic calculations of the flow field. The feasibility of just using a downwards shift is highlighted there by the red arrow, which is the shift necessary to match the open boundary case (red dashed line) to the bounded one (simulation values and green dotted line).

Since a fixed colloidal particle does by definition not move, all phoretic force (or the complete slip velocity) induces motion of the fluid and not the colloid. The constant backflow effectively hinders this fluid motion, and reduces thereby the force (or displacement) measured in simulations. To account for it in the analytic calculation of the force here, the flow velocity at a distance corresponding to the system boundary of the simulation system is taken. This velocity is related to a

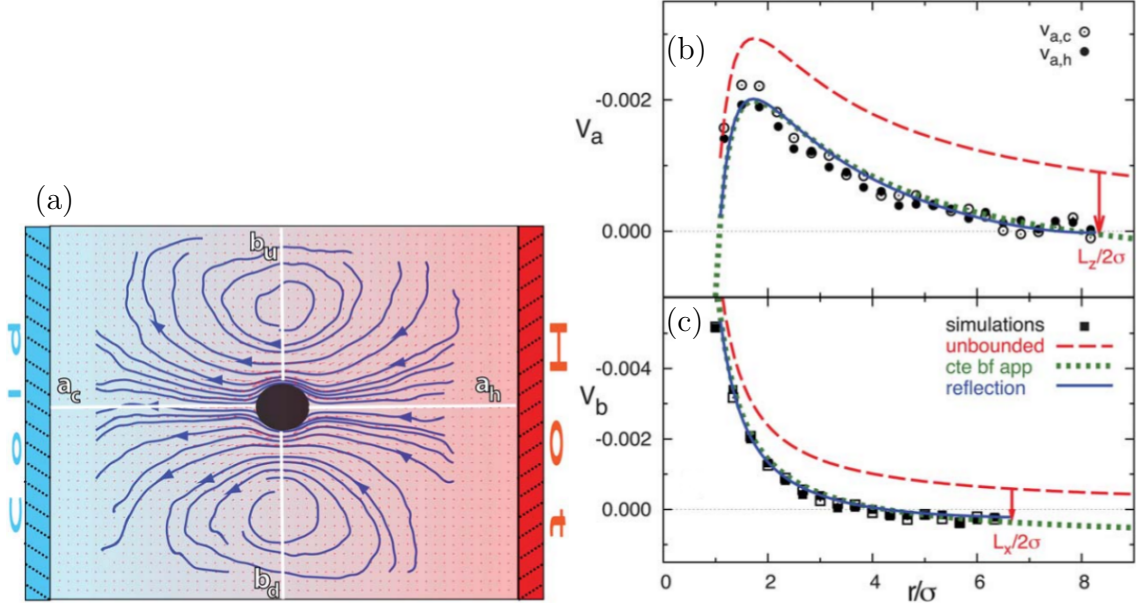


Figure 3.3: **a)** The flow field of a fixed colloidal particle in a bounded system. **b,c)** Velocity of the flow as a function of distance from the colloidal center along the axes $a_{c,h}$ in direction of the temperature gradient (**b**) and the axes $b_{u,d}$ perpendicular to the temperature gradient (**c**); as shown in **a**). Symbols correspond to simulation results, dashed lines to the theoretical calculation in eq. (3.24), dotted lines to the constant backflow approximation, and solid lines to another theoretical calculation based on the reflection method. Arrows indicate the position of the system boundaries.

force f_ζ through the friction coefficient $\zeta = C_\zeta \pi \mu_d r_{\text{colloid}}$ as

$$f_\zeta = C_\zeta \pi \mu_d r_{\text{colloid}} v_{\text{colloid}} \cdot \quad (3.25)$$

The prefactor $C_\zeta = 3$ is used, based on the result of Yang et al. [55] for a MPC fluid that does not conserve angular momentum. The resulting friction force is opposed to the thermophoretic force and an effective thermophoretic force is calculated as the sum of the unbounded solution and this effective friction force, such that a corrected value for the thermal diffusion factor results as $\alpha_T^c = (f_\zeta + f_T)/\nabla_g T$.

These corrected predictions are compared to simulated thermal diffusion factors again in table 3.1. Leaving out the values for $\sigma = 1$, the average deviation to results obtained with the SPTA method is ca. $7 \pm 7\%$. The error bars are not given for the simulation values, but can be estimated from other measurements performed in [35] to be of order $\pm 10\%$ and larger, such that the made predictions agree quite well with the simulated values. Notable deviations larger than 10% occur only for attractive potentials with larger s , deviations for repulsive potentials and attractive with $s = 2$ are around $\pm 3\%$

3.3.2 Slip Velocity due to Thermophoresis

The interpretation of colloidal thermophoresis as a combination of thermophoretic and diffusiophoretic contributions can also be included in the general description of phoretic effects provided by eq. (3.4). This equation is the starting point to obtain an expression for the slip velocity. In it, the excess pressure p will now not only have a position-dependent density term (diffusiophoresis), but also a position-dependent temperature term is introduced according to

$$p(x_l, z_l) = \rho(x_l)k_B T(x_l) \left(\exp\left[-\frac{U(z_l)}{k_B T(x_l)}\right] - 1 \right). \quad (3.26)$$

Again, the interaction potential has no perpendicular component, such that f_{x_l} in eq. (3.4) is zero. The derivative $\frac{dp}{dx_l}$ is now given by

$$\begin{aligned} \frac{dp}{dx_l} = & \frac{d\rho}{dx_l} k_B T \left(\exp\left[-\frac{U}{k_B T}\right] - 1 \right) \\ & + \frac{dT}{dx_l} \left(k_B \rho \exp\left[-\frac{U}{k_B T}\right] - k_B \rho + \frac{U\rho}{T} \exp\left[-\frac{U}{k_B T}\right] \right). \end{aligned} \quad (3.27)$$

Plugging it into eq. (3.4) gives

$$\begin{aligned} v_B = & -\frac{k_B T}{\mu_d} \frac{d\rho}{dx_l} \int_0^B dz_l z_l \left(\exp\left[-\frac{U}{k_B T}\right] - 1 \right) \\ & - \frac{1}{\mu_d} \frac{dT}{dx_l} \int_0^B dz_l z_l \left(k_B \rho \exp\left[-\frac{U}{k_B T}\right] - k_B \rho + \frac{U\rho}{T} \exp\left[-\frac{U}{k_B T}\right] \right) \end{aligned} \quad (3.28)$$

where the density gradient dependent term is exactly equivalent to eq. (3.6). Note that the density gradient here is not an independent function of the temperature field. Rather, it follows directly as a consequence of the non-uniform distribution of temperature through the equation of state of the fluid.

This equation again has to be formulated in appropriate coordinates for the problem of interest. Treating the same setup of a colloid in a temperature gradient as was done in the calculation of the force f_T , the resulting expression reads

$$\begin{aligned} v_B(\bar{R}, \theta) = & -\frac{k_B T(\bar{R}, \theta)}{\mu_d} \nabla_\theta \rho(\bar{R}, \theta) \int_0^B dz_l z_l \left(\exp\left[-\frac{U(z_l)}{k_B T(\bar{R}, \theta)}\right] - 1 \right) \\ & - \frac{1}{\mu_d} \nabla_\theta T(\bar{R}, \theta) \int_0^B dz_l z_l \left(k_B \rho(\bar{R}, \theta) \exp\left[-\frac{U(z_l)}{k_B T(\bar{R}, \theta)}\right] \right. \\ & \left. - k_B \rho(\bar{R}, \theta) + \frac{U(z_l)\rho(\bar{R}, \theta)}{T(\bar{R}, \theta)} \exp\left[-\frac{U(z_l)}{k_B T(\bar{R}, \theta)}\right] \right) \end{aligned} \quad (3.29)$$

which can also be shortened introducing

$$\kappa_\rho(\bar{R}, \theta) = \frac{k_B T(\bar{R}, \theta)}{\mu_d} \Lambda_\rho(\bar{R}, \theta) \quad (3.30)$$

$$\kappa_T(\bar{R}, \theta) = \frac{1}{\mu_d} \Lambda_T(\bar{R}, \theta) \quad (3.31)$$

with

$$\Lambda_\rho(\bar{R}, \theta) = \int_0^B dz_l z_l \left(\exp \left[-\frac{U(z_l)}{k_B T(\bar{R}, \theta)} \right] - 1 \right) \quad (3.32)$$

$$\begin{aligned} \Lambda_T(\bar{R}, \theta) = \int_0^B dz_l z_l \left(k_B \rho(\bar{R}, \theta) \exp \left[-\frac{U(z_l)}{k_B T(\bar{R}, \theta)} \right] \right. \\ \left. - k_B \rho(\bar{R}, \theta) + \frac{U(z_l) \rho(\bar{R}, \theta)}{T(\bar{R}, \theta)} \exp \left[-\frac{U(z_l)}{k_B T(\bar{R}, \theta)} \right] \right) \end{aligned} \quad (3.33)$$

such that eq. (3.28) reads as

$$\mathbf{v}_B(\bar{R}, \theta) = -\kappa_\rho(\bar{R}, \theta) \nabla_{\theta \rho}(\bar{R}, \theta) - \kappa_T(\bar{R}, \theta) \nabla_{\theta T}(\bar{R}, \theta). \quad (3.34)$$

This shows how the effect is split into two additive contributions of a density gradient and a temperature gradient, as already hinted to in the qualitative interpretation based on fig. 3.2a. Comparing to the expression for diffusiophoresis, eq. (3.9), the density gradient contribution takes a more complex form, as the prefactor κ_ρ is now position-dependent. This position-dependence stems from the temperature dependence of the Boltzmann factor, such that this contribution is not solely due to the density distribution. However, a clear distinction between the effects of the temperature and density gradients themselves is possible.

Formulating the phoretic effect in terms of the slip velocity, the velocity of the colloid is now obtained by the orientational surface average of the slip velocity according to

$$v_{\text{colloid}} = -\langle \mathbf{v}_B \cdot \hat{\mathbf{z}} \rangle_S \quad (3.35)$$

where

$$\langle \dots \rangle = \frac{1}{4\pi \bar{R}^2} \int_{S_0} dS \dots \quad (3.36)$$

is the average over the spherical surface considered [78]. For a single spherical colloid in a temperature gradient, the integration can be avoided since the slip velocity can be obtained from its maximum value $\bar{v}_B = v_B(\theta = 90^\circ)$ occurring at

midplane as $v_B = \bar{v}_B \sin(\theta)$ [42]. Then, the colloid velocity results as

$$v_{\text{colloid}} = -\frac{2}{3}\bar{v}_B. \quad (3.37)$$

With the colloid's velocity known, to obtain the thermal diffusion factor α_T through eq. (3.18), the force corresponding to the colloid's velocity is calculated with eq. (3.25).

Calculations using the route of slip velocity have been performed for all cases considered in table 3.1, arriving at the same result in every case. The agreement in between the two routes of direct force calculation with and using the slip velocity with eq. (3.34) is always within numeric error of the integrations performed, typically $\ll 1\%$. It is concluded that the two approaches, using either the force or the velocity to obtain the thermal diffusion factor, present completely equivalent formulations of thermophoresis.

3.4 Analysis of Thermophoresis

The framework developed so far can be used to study the trends observed for the size and temperature dependence of the Soret coefficient $S_T = \alpha_T/T$ in colloidal thermophoresis.

3.4.1 Simulation Results

Lüsebrink performed MPC simulations to characterize the temperature and size dependence of the Soret coefficient and also provided analytical predictions for it, the latter capturing all qualitative trends albeit with some systematic deviations [41]. He studied the size as well as the temperature dependence of the Soret coefficient for different types of colloid-fluid interaction potentials. For all repulsive potentials, the Soret coefficient was found to be negative for all considered temperatures. For the attractive interactions investigated, it was positive at low temperatures, but turned negative at higher temperatures, showing a minimum before converging to zero. This behavior, exhibiting a minimum in the course of the Soret coefficient's dependence on temperature, cannot be captured by the empirical relation of eq. (1.40). The size dependence of the Soret coefficient was found to scale cubic with particle size, which was attributed to the interaction volume scaling the same when non-displaced interaction potentials of the Lennard-Jones type were used. For displaced potentials, which allow keeping the interaction radius σ_{cf} constant while enlarging the particle size, an increase in particle size showed a quadratic scaling of the Soret coefficient, again consistent with that of the interaction volume. An exception from this was found for attractive interactions with higher strengths, that showed a quadratic size dependence even when not displaced.

Table 3.2: Comparisons of exponents b describing the size dependence $\alpha_T(s)$ according to eq. (3.38) obtained with eq. (3.23) to simulation results of Lüsebrink [41]. Results are given for colloids modeled with different potentials according to eq. (2.7) in terms of parameter sets $(s, \Delta, \varepsilon, n, r/a)$.

Potential	b - theory	b - simulation
repulsive		
$(s, 0, 1, 6, r)$	3.0	3.0
$(s, 0, 4, 6, r)$	3.0	3.1
$(s, 0, 1, 12, r)$	3.0	3.1
$(s, 0, 4, 12, r)$	3.0	2.8
attractive		
$(s, 0, 0.1, 12, a)$	3.0	3.2
$(s, 0, 1, 48, a)$	3.0	2.9
$(s, 0, 1, 12, a)$	3.0	2.2
$(s, 0, 4, 12, a)$	3.0	1.8
displaced		
$(s, s - 1, 1, 6, r)$	2.0	1.9
$(s, s - 1, 0.25, 6, a)$	1.76; 1.95	1.8 (theory)

3.4.2 Size Dependence

The trends in scaling observed by Lüsebrink are mainly confirmed by the approach here developed. In the following, the correction for backflow is not taken into account, as it is mainly of concern to the specific simulations that measure α_T or the Soret coefficient and the focus lies on the scaling behavior. Table 3.2 presents comparisons of the exponents b obtained in simulations of Lüsebrink [41] with those obtained using the outlined theory. The functional form used for fitting is given by

$$\alpha_T = \alpha_T^0 \left(\frac{s}{a} \right)^b \quad (3.38)$$

where α_T^0 and b are free parameters. For all repulsive and attractive potentials, as long as no displacements are used, the theoretical predictions agree exactly with the scaling of the interaction volume. For all repulsive potentials, this also agrees to simulation results, with minor differences likely attributable to statistical errors and backflow in the simulations. However, for the two non-displaced attractive potentials with higher interaction strength ε , simulations predict a value around $b = 2.0$. The developed theory does, still in accordance with the scaling of the interaction volume, predict $b = 3.0$ instead. In fact, also for even higher values $\varepsilon = \{5, 10\}$ no deviations in prediction from $b = 3.0$ could be observed here. Considering backflow-

corrected predictions does also not alter that scaling. An explanation that would account for these deviations is that the flow induced by colloidal thermophoresis in the simulations with strong attractive potentials is very fast, such that the behavior becomes non-linear and therefore deviates from the predictions based on considering only small disturbances to the equilibrium distributions of temperature and density.

The introduction of displacements into the colloid-fluid interaction has been observed to lead to an exponent $b = 2$, which is also confirmed by the theory developed here for all repulsive potentials. For attractive displaced potentials, only one theoretical result of Lüsebrink is available, giving $b = 1.8$. Using the same data points at $s = 1, 2, 3, 4, 5, 6$, here also $b = 1.8$ is obtained. However, considering a larger range, $s = 1$ to $s = 30$ in steps of 1 for the fit, $b = 1.95$ results. This indicates that something different is happening here as compared to repulsive potentials. Lüsebrink noted that the chosen cutoff might be an issue, in that a short one will reduce the exponent. Here however, using the standard cutoff $c_{\text{cut}}\sigma_{\text{cf}} + \Delta$ with $c_{\text{cut}} = 2.5$ as well as $c_{\text{cut}} = 2.0$ and 10.0 did lead to the same scaling with $b = 1.95$ when considering the larger data set. Only for $c_{\text{cut}} = 1.5$, a smaller value of $b = 1.91$ was obtained, this however is an unphysical choice of cutoff. When considering the same dataset as Lüsebrink, a choice of larger cutoff $c_{\text{cut}} = 10$ leads to $b = 1.76$, in fact reducing the exponent, in contrast to what is noted in his work.

3.4.3 Temperature Dependence

As a starting point, consider eq. (3.28) in rewritten form as

$$\begin{aligned}
 v_B = & -\frac{k_B T}{\mu_d} \frac{d\rho}{dx_l} \underbrace{\int_0^B dz_l z_l \left(\exp\left[-\frac{U}{k_B T}\right] - 1 \right)}_{=I_1} - \frac{k_B \rho}{\mu_d} \frac{dT}{dx_l} \underbrace{\int_0^B dz_l z_l \left(\exp\left[-\frac{U}{k_B T}\right] - 1 \right)}_{=I_1} \\
 & - \frac{\rho}{T \mu_d} \frac{dT}{dx_l} \underbrace{\int_0^B dz_l z_l U \exp\left[-\frac{U}{k_B T}\right]}_{=I_2} \\
 = & \frac{k_B}{\mu_d} (-T \nabla_{x_l} \rho - \rho \nabla_{x_l} T) I_1 - \frac{\rho}{T \mu_d} \nabla_{x_l} T I_2, \tag{3.39}
 \end{aligned}$$

where the integral terms have been abbreviated with $I_{1,2}$ for ease of notation. There are three additive contributions. The first and second involve the density and temperature gradient and the same integral I_1 . The third term involves the temperature gradient and the integral I_2 , where the colloid-fluid potential U goes in directly. For small temperature gradients, a linear relation in between temperature and density gradient may reasonably be considered, such that eq. (3.17), which linearizes the

density gradient through $\nabla_{x_i}\rho = -\frac{\bar{\rho}}{T}\nabla_{x_i}T$, can be used to simplify eq. (3.39) into

$$v_B = \frac{k_B\nabla_{x_i}T}{\mu_d} \left(\frac{T}{\bar{T}}\bar{\rho} - \rho \right) I_1 - \frac{\rho}{T\mu_d} \nabla_{x_i}T I_2. \quad (3.40)$$

In the scenario of small temperature gradients, the prefactor $T\bar{\rho}/\bar{T} - \rho$ of I_1 will be close to zero, as the local temperature T will be close to the average temperature \bar{T} , as will be the local density ρ to the average density $\bar{\rho}$. The precise values the expressions take on depend of course on the chosen setup. For a colloid interacting with the fluid through a potential according to eq. (2.7) with parameters (3, 0, 0.1, 12, a), typical numeric values for the integrals are $I_1 \approx -1.8$ and $I_2 \approx -3.5$, so these are of comparable magnitude. The prefactor to I_1 evaluates to exactly 0.0 at midplane when the colloid is placed in the exact middle of the box. At the sides, it is of order 10^{-19} . The prefactor to I_2 on the other hand is about 10^{-3} . This clearly shows that the first term in eq. (3.40) gives a negligible contribution. The slip velocity is then mainly determined by

$$v_B = -\frac{\rho}{T\mu_d} \nabla_{x_i}T I_2. \quad (3.41)$$

The colloid velocity results from the surface average of the slip velocity v_B , which is its value at midplane $v_{\text{colloid}} = -\frac{2}{3}\bar{v}_B$ (eq. (3.37)). Since for the value at midplane, it does not matter if the gradient is taken in Cartesian or polar coordinates, $\nabla_{x_i}T$ will have the sign it also has in Cartesian coordinates. For a freely moving particle in a solvent with a temperature gradient in z -direction, the friction force f_ζ and the thermal driving force f_T balance. One may therefore write $f_T = f_\zeta = C_\zeta\pi\mu_d Rv$ and plug in the colloid velocity to obtain, with $f_T = -\alpha_T k_B \nabla_{x_i}T$, the Soret coefficient as

$$S_T = \frac{\alpha_T}{\bar{T}} = -\frac{C_\zeta\pi\mu_d Rv_{\text{colloid}}}{k_B\bar{T}\nabla_z T}. \quad (3.42)$$

Note that this is only an approximation, though a good one, as discussed in more detail in [35].

Based on eq. (3.41), the behavior of the Soret coefficient as a function of average temperature \bar{T} can be understood. Consider first a purely repulsive, i.e. always positive, potential. I_2 will then always be positive as well, such that v_B is always opposite to the temperature gradient. As the colloid velocity results from the slip velocity at midplane as $v_{\text{colloid}} = -\frac{2}{3}\bar{v}_B$, the colloid will always move in the direction of the temperature gradient, i.e. show thermophilic behavior. Equation (3.41) does not depend on the average temperature anymore and no sign change is to be expected from its functional form. It is however still proportional to $\nabla_{x_i}T/T$. As with increasing average temperature, also the local temperature T will rise, this term will lead to the colloid's velocity going to zero for high temperatures. The described behavior is consistent with simulation results on colloidal thermophore-

sis with purely repulsive potentials [24, 25, 35, 41]. The typical behavior of the Soret coefficient as a function of average temperature is shown in fig. 3.4a for a representative case.

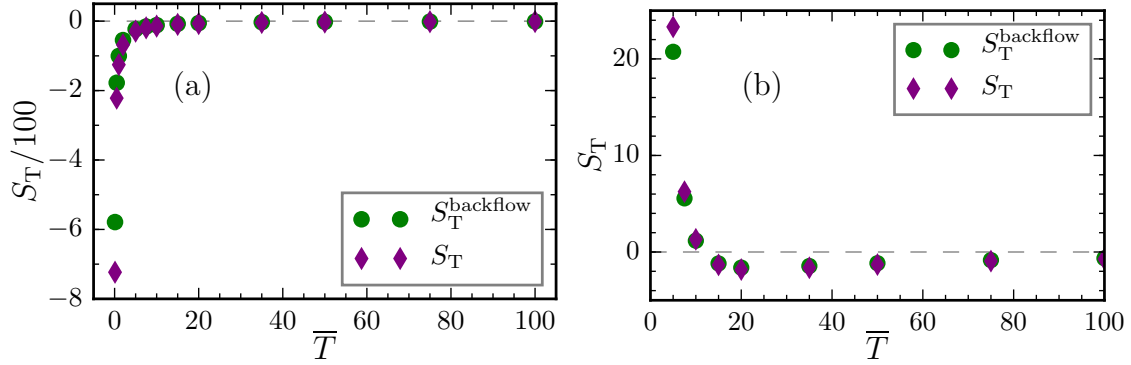


Figure 3.4: Temperature dependence of the Soret coefficient $S_T(\bar{T})$ for a repulsive interaction potential with $(3,0,1,6,r)$ (a) and an attractive one with $(3,0,0.1,12,a)$ (b). Purple diamonds denote the theoretical prediction for S_T , green symbols same but including the correction for backflow.

When the colloid-fluid interaction includes an attractive part, it may take on both positive and negative values, which will in turn determine the sign of I_2 and thereby the Soret coefficient. For a representative attractive interaction potential, fig. 3.5a shows how the integrand of I_2 behaves at different temperatures. There

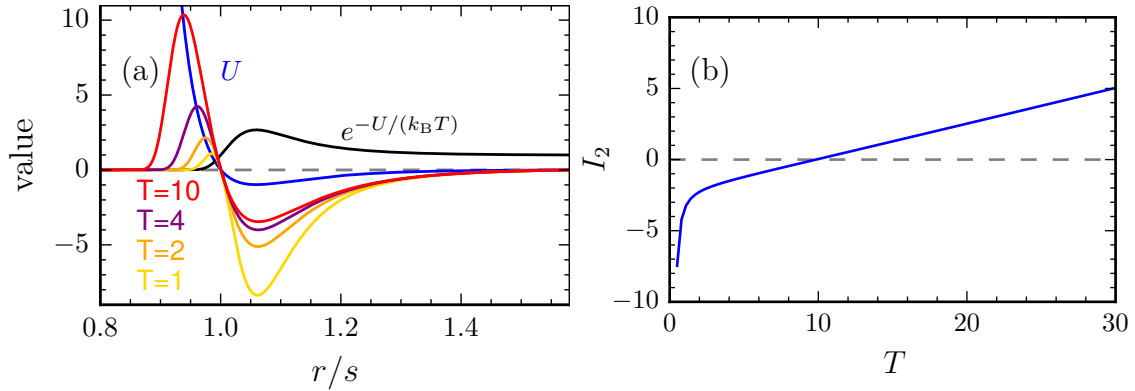


Figure 3.5: Analysis of I_2 in eq. (3.39) for an attractive potential with $(3,0,0.1,12,a)$. **a)** Blue line shows the interaction potential U , black line $\exp[-\frac{U}{k_B T}]$ at $T = 1$. Bright lines show the whole integrand of $I_2 = rU \exp[-\frac{U}{k_B T}]$ at temperatures $T = 1$ (yellow), $T = 2$ (orange), $T = 4$ (purple) and $T = 10$ (red). **b)** The value of I_2 as a function of temperature T .

is a crossover at $r/s = 1$, and the integrals to the left and right of $r/s = 1$ have

opposite signs and will give different relative contributions as a function of temperature. Figure 3.5b then shows I_2 as a function of temperature. The expected sign change is seen at ca. $T = 10$, and the value changes from negative to positive, which means for the Soret coefficient a change from positive to negative values, i.e. thermophobic to thermophilic behavior. This is consistent with the crossover in the evaluation of the complete expression for the slip velocity, shown for the same interaction potential in fig. 3.4b, which indicates that indeed I_2 gives the dominant contribution to the Soret coefficient. In the limiting case of high temperatures, the Soret coefficient will vanish due to the same considerations already discussed for repulsive potentials.

3.4.4 Hard Spheres

It is of interest to also study the limiting case in which the colloid interacts with the fluid through a hard-sphere potential. Then, the interaction potential U is given by

$$U_{\text{HS}}(r) = \begin{cases} \infty, & r < B \\ 0, & r \geq B, \end{cases} \quad (3.43)$$

and eq. (3.39) can be solved analytically. For U_{HS} , the terms $\exp[-U_{\text{HS}}/(k_{\text{B}}T)]$ act like Heaviside functions $H(B)$. Therefore I_1 gives $-B^2/2$. The other integral, I_2 , is zero for $z_l < B$, as the exponential dominates. For $z_l \geq B$, the potential gives $U_{\text{HS}}(z_l \geq B) = 0$, such that I_2 vanishes completely for hard spheres. This leads to, assuming again a linearized density gradient, an expression similar to eq. (3.40) for the hard sphere potential:

$$v_B = \frac{k_{\text{B}}B^2}{2\mu_{\text{d}}} \left(\rho - \frac{T}{\bar{T}}\bar{\rho} \right) \nabla_{x_l} T. \quad (3.44)$$

As discussed in the derivation of eq. (3.41), the term $\rho - \bar{\rho}T/\bar{T}$ will be close to zero, such that only a marginal phoretic response is expected for hard spheres. The Soret coefficient follows from eq. (3.42) as

$$S_{\text{T}} = \frac{\alpha_{\text{T}}}{T} = \frac{C_{\zeta}\pi}{T} \frac{1}{3} B^3 \left(\rho - \frac{T}{\bar{T}}\bar{\rho} \right), \quad (3.45)$$

from which a cubic scaling with colloid size B is expected. To check these conclusions, SPTA simulations of hard spheres were performed, whose results are shown in fig. 3.6. Clearly, the only conclusion that can be justified is that hard spheres show a very low phoretic response. Even though averages are taken over 48 runs, fitting to any functional form is not meaningful due to the large statistical errors, and no conclusion can be drawn on describing the size dependence. The Soret coefficient of hard spheres tends on average more towards positive values, i.e. thermophobic behavior, in these simulations. From the analytic description offered by eq. (3.45),

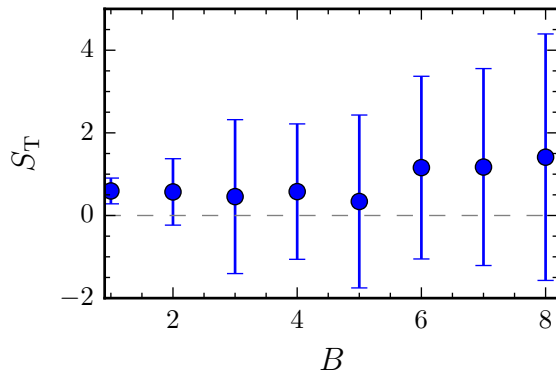


Figure 3.6: Size dependence of the Soret coefficient S_T for hard spheres with radius B .

the sign should depend solely on the small term $\rho - \bar{\rho}T/\bar{T}$, whose sign depends on the local temperature and density and may change depending on where the colloid is located. In the simulations performed here, it was in the mid of the simulation box, where the local values are close to the average values of temperature and density.

3.5 Summary and Outlook

The developed theory provides two consistent formulations to calculate the thermal diffusion factor α_T or Soret coefficient S_T for any colloid-solvent interaction in an ideal-gas like solvent. One way is through a direct evaluation of the potential interactions, making use of the knowledge of the temperature and density distribution according to eq. (3.23). The other way is by taking the surface average of the slip velocity, evaluating eq. (3.28). Agreement to simulation results obtained with MPC-MD shows the feasibility of the approach. The numerical effort to perform such calculations is minimal, especially as compared to performing simulations. Based on the analytic formulation obtained, it can be shown that the dominant contribution to the Soret coefficient in typical setups stems from a term directly involving the interaction potential (I_2 in eq. (3.39)), which also explains the different temperature dependencies seen for purely repulsive and as attractive colloid-fluid interaction potentials. Furthermore, it is shown why hard spheres only show very low phoretic responses. A hard-sphere description of colloid-fluid interactions is therefore not well suitable to study thermophoresis in simulations, though it may be possible to use additional modifications to the hard-sphere interaction that enhance the effect, as was done for diffusiophoretically driven Janus particles in [78]. The simulation results of Lüsebrink [41] concerning the size dependence of the Soret coefficient, scaling mostly cubic for undisplaced and, with only minor deviations, quadratic for displaced potentials, are mostly confirmed by the theoretical approach.

The developed formulation and theory necessarily requires an ideal gas equa-

tion of state of the fluid. This works perfectly to predict MPC-MD simulation results, in which this is the case, but will not as well model a real fluid. Therefore, it might be of interest to consider extensions to different equations of states and their influence on the behavior of the Soret coefficient. Another interesting point is the colloid-fluid interaction potential employed. The description will work for any functional form of the interaction, such that arbitrary potentials can be investigated. Especially potentials adapted to experimental measurements will be of interest. Furthermore, the observed temperature dependencies do not match the empirical relation of eq. (1.40), which may be related to the functional form of the colloid-fluid interaction, the fluid equation of state or both. To find out which kinds of potential reproduce the behavior of eq. (1.40), and if it is at all possible to do so by adapting solely the interaction potential, will give further insight into the phenomenology.

4 Single Swimmer Dynamics

4.1 Dimeric Swimmers

A dimeric colloidal swimmer, for brevity called dimer, is a type of swimmer constructed out of two connected beads featuring different properties. The necessary symmetry breaking for phoretic self-propulsion to work is based on one bead supplying the gradient and the other reacting to it. A thermophoretic dimer therefore has one bead consisting of a material that will absorb energy and produce thereby a steady local temperature gradient, which will be called the hot bead. The other bead consists of a material that does not absorb energy, but experiences a phoretic force due to the local gradient supplied by the hot bead, and will be called the phoretic bead. The first model of dimeric swimmers was created by Rückner and

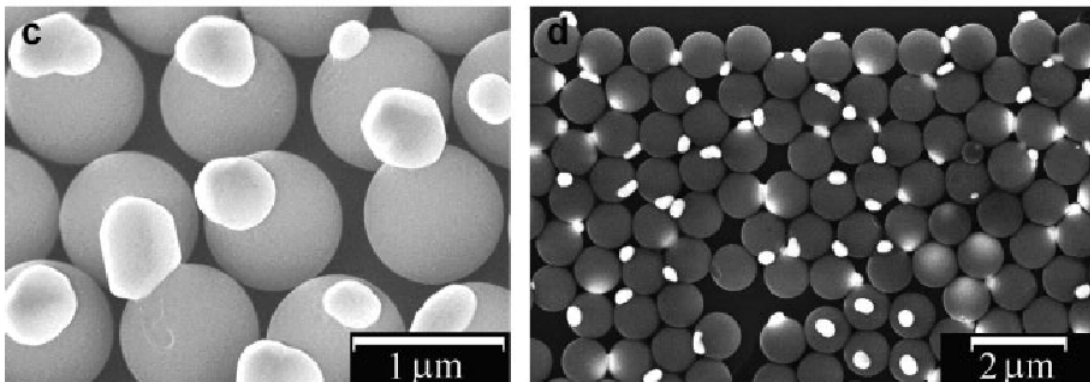


Figure 4.1: SEM images of experimentally synthesized dimer swimmers. Taken from [19]. Another view of these dimers is shown in fig. 1.4a.

Kapral [18], for one driven by chemical gradients. The construction was shown to work also for a thermal driving mechanism by Yang and Ripoll [24]. The flow field of a thermophoretic symmetric dimer, in which both beads have the same size, was calculated and measured by Yang et al. [25]. More recently, for the case of chemical dimers, an analytical continuum theory was developed by Reigh and Kapral [76]. A proof-of-concept experimental realization of chemically driven dimers was performed by Valadares et al. and is shown in fig. 4.1 [19]. The interaction of two of these swimmers with phoretically attractive interactions has been studied by Thakur and Kapral [77]. The same authors later on also studied small ensembles of up to 10 dimers in quasi-two-dimensional confinement, also for the case of phoretically attractive interactions [79].

The comparison of thermally and chemically driven dimers is of interest since the general framework describing phoretic effects is independent of the microscopic details of the driving mechanism [74], which leads to the assumption that their swimming behavior should be similar. This has however not been explicitly confirmed for the simulation models of interest here. Similar results obtained for chemical and thermal dimers therefore also present a mutual validation of the proposed models.

4.1.1 Model

The dimer swimmer is modeled in simulations by two beads, of specified radii s_h for the hot bead and s_p for the phoretic one. To connect them, a strong harmonic bond is used. How the phoretic effect depends on the colloid-fluid interaction of the phoretic bead in MPC-MD simulations was investigated by Lüsebrink et al. [35] and Yang and Ripoll [24], who found that the dimer behaves thermophilic for soft repulsive potentials, as expected by the framework developed in chapter 3, and thermophobic for steep attractive potentials in the cases considered. In this work an optimal potential is chosen based on that study, i.e. the one that leads to the highest propulsion speed. This will reduce computational effort and also lead to more prominent hydrodynamic flow fields. The colloid-fluid interaction of the hot bead does not determine the reaction of the swimmer to the temperature gradient, such that here a steep repulsive potential is chosen, also to minimize computational effort. For every dimer studied in this work, the repulsive form of eq. (2.7) with $n = 24$ and $\varepsilon = 1$ is used to model the hot bead. To obtain thermophilic behavior, eq. (2.7) with $n = 3$ and $\varepsilon = 1$ in the repulsive form is used to model the phoretic bead. Thermophobic behavior corresponds to using eq. (2.7) with $n = 24$ in the attractive form, also with $\varepsilon = 1$. Heating is modeled by rescaling the temperature of fluid particles in a spherical shell around the center of the hot bead in the range $s_h < r < 1.08s_h$ to a desired value T_h , which is, if not explicitly stated otherwise, chosen to be $T_h = 1.5$. It is as well be possible to choose a fixed width d_T for the thermostatting layer, and the influence of these two choices on swimming behavior will be studied. There are two degrees of freedom in the geometric construction of dimer swimmers. One is the size ratio of the two beads $\gamma = s_p/s_h$ and the other is the bond length, which is defined here in terms of an extra separation δ_b , such that the whole bond length is $s_h + s_p + \delta_b$. In this formulation, $\delta_b = 0$ corresponds to the two beads at contact. An illustration of the dimer's construction parameters is shown in fig. 4.2a.

4.1.2 Theoretical Approaches

There are two analytic descriptions available for dimeric swimmers. The approach of Yang et al. [25] uses a superposition of the independent solutions of the Stokes equation for each of the beads to describe the hydrodynamic flow field of the dimer,

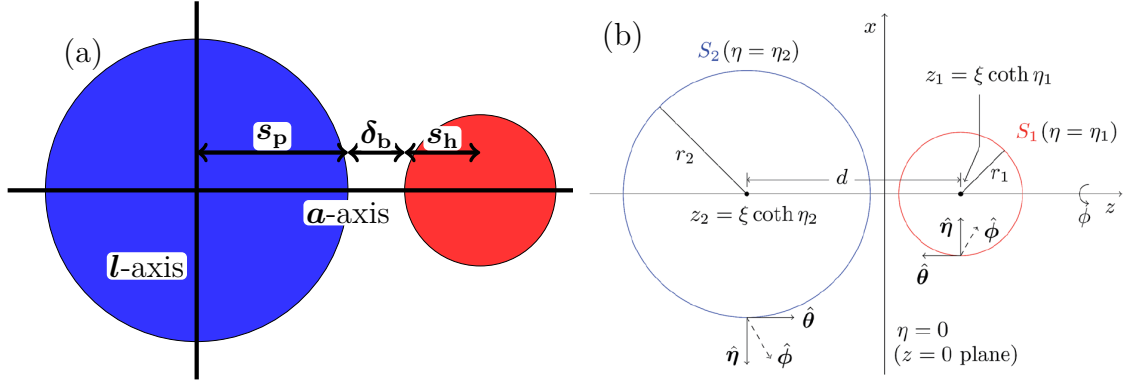


Figure 4.2: **a)** Schematic drawing of a dimer. The axis along which the flow field will be measured, namely the axial (*a*-axis) and a lateral (*l*-axis) are pointed out. **b)** Bispherical coordinate system (θ, η, ϕ) with the base unit vectors, $(\hat{\theta}, \hat{\eta}, \hat{\phi})$, for the sphere-dimer motor. The labels $S_1(\eta = \eta_1)$ and $S_2(\eta = \eta_2)$ represent the surfaces of the hot (or catalytic) and phoretic spheres with radii r_1 (red) and r_2 (blue), respectively. The spheres with centers z_1 and z_2 are separated by a bond distance d . Taken from [76].

obtaining

$$\mathbf{v}(\mathbf{r}) = \mathbf{v}_h(\mathbf{r}) + \mathbf{v}_p(\mathbf{r}) \quad (4.1)$$

$$\mathbf{v}_h(\mathbf{r}) = \frac{s_h}{2|\mathbf{r} - \mathbf{r}_h|} \left(\frac{(\mathbf{r} - \mathbf{r}_h)(\mathbf{r} - \mathbf{r}_h)}{|\mathbf{r} - \mathbf{r}_h|^2} + \mathbf{I} \right) \cdot \mathbf{v}_s \quad (4.2)$$

$$\begin{aligned} \mathbf{v}_p(\mathbf{r}) = & -\frac{s_p}{2|\mathbf{r} - \mathbf{r}_p|} \left(\frac{(\mathbf{r} - \mathbf{r}_p)(\mathbf{r} - \mathbf{r}_p)}{|\mathbf{r} - \mathbf{r}_p|^2} + \mathbf{I} \right) \cdot \mathbf{v}_s \\ & + \frac{s_p^3}{|\mathbf{r} - \mathbf{r}_p|^3} \left(\frac{3(\mathbf{r} - \mathbf{r}_p)(\mathbf{r} - \mathbf{r}_p)}{|\mathbf{r} - \mathbf{r}_p|^2} + \mathbf{I} \right) \cdot \mathbf{v}_s \end{aligned} \quad (4.3)$$

as an expression for the fluid velocity field $\mathbf{v}(\mathbf{r})$, where \mathbf{I} is the unit tensor. The subscripts h and p correspond to the hot and phoretic beads, $r_{h,p}$ to their positions and v_s denotes the dimer's swimming velocity. This approach offers a comparably simple way to obtain an analytical expression for the flow field. Yang et al. considered symmetrically built thermophoretic dimers, i.e. $\gamma = 1$, with bead sizes of $s = 2.5$, and a separation between the beads of $\delta_b = 0.5$. They found very good agreement between predicted and simulated flow fields, both in the thermophilic and thermophobic case [25]. This approach is restricted to a prediction of the flow fields and requires knowledge of the swimming velocity v_s , which was measured in simulations.

A more extensive and accurate description is given by Reigh and Kapral [76], that describes dimer swimmers working on chemical gradients. In the following, an overview over their approach is given. A chemical/catalytic dimer swimmer works

by producing a gradient of some chemical species instead of a temperature gradient at one bead, the catalytic bead, while the other phoretic bead reacts to the steady local concentration gradient. This is the case of the diffusiophoretic effect. The simulation model considers the solvent to be composed of two species A and B . When in contact to the catalytic sphere S_1 , A can undergo conversion to a species B in terms of the chemical reaction $A + S_1 \rightarrow B + S_1$ with intrinsic rate constant k_0 . The interactions are chosen such that species A and B have the same interaction with S_1 , but the interactions of A and B with the phoretic sphere S_2 differ. Far away from the swimmer, a conversion of B back to A takes place to steadily supply reactive species and maintain a stable concentration gradient.

The dimer type of construction can, for some positive value of δ_b , be described in a bispherical coordinate system. Bispherical coordinates are given as (θ, η, ϕ) with

$$0 \leq \theta \leq \pi; \quad -\infty \leq \eta \leq \infty; \quad 0 \leq \phi \leq 2\pi. \quad (4.4)$$

They relate to Cartesian coordinates (x, y, z) through

$$x = \xi \frac{\sin(\theta) \cos(\phi)}{\cosh(\eta) - \cos(\theta)}; \quad y = \xi \frac{\sin(\theta) \sin(\phi)}{\cosh(\eta) - \cos(\theta)}; \quad z = \xi \frac{\sinh(\eta)}{\cosh(\eta) - \cos(\theta)} \quad (4.5)$$

where ξ is a scale factor. Two spheres are described by choosing radii r_1 and r_2 and a separation $d = r_1 + r_2 + \delta_b$. They are then represented by $\eta = \eta_1 (> 0)$ and $\eta = \eta_2 (< 0)$, with the bispherical coordinate parameters given by

$$\xi = \frac{1}{2d} \sqrt{(d^2 - r_1^2 - r_2^2)^2 - 4r_1^2 r_2^2} \quad (4.6)$$

$$\eta_1 = \ln\left(\xi/r_1 + \sqrt{1 + (\xi/r_1)^2}\right) \quad (4.7)$$

$$\eta_2 = -\ln\left(\xi/r_2 + \sqrt{1 + (\xi/r_2)^2}\right). \quad (4.8)$$

A visualization of the coordinate system is shown in fig. 4.2b. For a more extensive discussion of bispherical coordinates and solutions of the Laplace equation in this system see [80]. Roughly speaking, varying θ for a fixed value of $\eta = \eta_0$ allows walking along a circle of radius $\xi|\operatorname{csch}(\eta_0)|$ lying in the xz -plane. This circle is located at negative z for $\eta_0 < 0$ and at positive z for $\eta_0 > 0$. This allows integration over this circle as $\int_0^\pi d\theta$ for fixed η_0 . Additionally considering ϕ then allows integration over the whole sphere. Bispherical coordinates also allow a convenient specification of different boundary conditions for the two spheres, since η is always pointing normal to the surface of the sphere.

The A -concentration field c_A around these dimers follows the Laplace equation

$$\nabla^2 c_A = 0 \quad (4.9)$$

with the boundary conditions

$$(\mathbf{J} \cdot \tilde{\boldsymbol{\eta}})_{\eta=\eta_1} = \bar{k}_0 c_A(\eta = \eta_1) \quad (4.10)$$

$$(\mathbf{J} \cdot \tilde{\boldsymbol{\eta}})_{\eta=\eta_2} = 0 \quad (4.11)$$

where $\mathbf{J} = -D\nabla c_A$ is the flux of the A -concentration field, $\bar{k}_0 = k_0/(4\pi r_1^2)$ is the reaction rate constant, D the (identical) diffusion constant of the A and B species and $\tilde{\boldsymbol{\eta}}$ is the surface normal vector of the spheres. The Laplace equation with these boundary conditions can be solved analytically in bispherical coordinates, leading to an expression for the c_A concentration field. The c_B concentration field is then obtained from the conservation condition $c_A + c_B = c_0$. With those known, it is possible to use the relations derived for the diffusiophoretic slip velocity, introduced in section 3.2, namely

$$\mathbf{v}_B = -\kappa \nabla_{\theta} c_B \quad (4.12)$$

with

$$\kappa = \frac{k_B T}{\mu_d} \Lambda; \quad (4.13)$$

$$\Lambda = \int_0^{\infty} r \left(\exp\left[-\frac{U_{2,B}(r)}{k_B T}\right] - \exp\left[-\frac{U_{2,A}(r)}{k_B T}\right] \right) dr \quad (4.14)$$

to determine the slip velocity \mathbf{v}_B of the fluid at the outer edge of the boundary layer B . In this equation, μ_d is the shear viscosity. Equation (4.14) contains the microscopic model, as discussed in more detail in [74], that relates a chemical gradient to a slip velocity of a colloidal particle. Now, with an analytic expression for the slip velocity describing the hydrodynamic boundary condition at the outer edge of the phoretic bead, one can proceed to solve the Stokes equation without external force

$$\nabla p = \mu_d \nabla^2 \mathbf{v} \quad (4.15)$$

with the incompressibility condition $\nabla \cdot \mathbf{v} = 0$. The fluid velocity field \mathbf{v} can be expressed in terms of Stokes' stream function ψ from $\mathbf{v} = \tilde{\boldsymbol{\phi}}/\rho \times \nabla \psi$. The boundary conditions in the laboratory frame, where the dimer moves with velocity v_s , are

$$\psi + \frac{1}{2} \rho^2 v_s \Big|_{\eta=\eta_1, \eta_2} = 0 \quad (4.16)$$

$$\frac{\partial}{\partial \eta} \left(\psi + \frac{1}{2} \rho^2 v_s \right) \Big|_{\eta=\eta_1} = 0 \quad (4.17)$$

$$\frac{\partial}{\partial \eta} \left(\psi + \frac{1}{2} \rho^2 v_s \right) \Big|_{\eta=\eta_2} = \kappa \rho \frac{\partial c_B}{\partial \theta} \Big|_{\eta=\eta_2}. \quad (4.18)$$

This again can be solved analytically. For a phoretic swimmer on which no external forces act, the surface integral of the stress tensor Π vanishes, so

$$F_z = \int_{S_1} \Pi_Z \cdot \tilde{\mathbf{n}} \, dS + \int_{S_2} \Pi_Z \cdot \tilde{\mathbf{n}} \, dS = 0 \quad (4.19)$$

where $\Pi_Z = \tilde{\mathbf{z}} \cdot \Pi$. Since the dimer is symmetric around ϕ , only the z -direction needs to be considered and one arrives at a full analytic expression for the velocity v_s . For more details and the complete expressions, see [76].

4.1.3 Theoretical Description of Thermophoretic Dimers

The description of Yang et al. can be straightforwardly applied to any dimer construction, independent of the driving mechanism. The outlined framework provided by the approach of Reigh and Kapral [76] may be adapted to thermophoresis, using the expressions for the slip velocity obtained in chapter 3. Instead of the concentration field c , one is then interested in the temperature field T , described by similar boundary conditions. The general thermophoretic framework derived in chapter 3 is more complicated than the diffusiophoretic, as its expression for the slip velocity, eq. (3.34), depends on both the temperature and density field. Furthermore, the prefactors κ_T and κ_ρ are no longer constant but depend on the angular position.

However, in section 3.4.3, it was shown that in a linearized version of the theory, it is no longer necessary to describe the density (or concentration) field separately from the temperature field, and only one main contribution results. This expression for the slip velocity, eq. (3.41), is in full form given by

$$v_B = -\frac{\rho}{T\mu_d} \nabla_{x_l} T \int_0^B dz_l z_l U(z_l) \exp\left[-\frac{U(z_l)}{k_B T}\right]. \quad (4.20)$$

For small temperature gradients, one might approximate ρ and T as constant in the prefactors, such that an expression according to

$$v_B = -\bar{\kappa}_T \nabla_{x_l} T \quad (4.21)$$

results, where $\bar{\kappa}_T$ now is assumed constant and given by

$$\bar{\kappa}_T = \frac{\bar{\rho}}{\mu_d \bar{T}} \Lambda; \quad (4.22)$$

$$\Lambda = \int_0^B dr r U \exp\left[-\frac{U(r)}{k_B \bar{T}}\right]. \quad (4.23)$$

This expression allows application of the framework of Reigh and Kapral to thermophoresis, given suitable boundary conditions for the heat flux q at the hot sphere. Specifically, the boundary condition eq. (4.10), $(\nabla c_A \cdot \tilde{\mathbf{n}})_{\eta=\eta_1} = -\bar{k}_0 c_A(\eta = \eta_1)/D$, is

substituted by a heat flux according to

$$(\nabla T \cdot \tilde{\mathbf{n}})_{\eta=\eta_1} = \frac{q}{k_T} \quad (4.24)$$

where k_T denotes the thermal conductivity. To solve the equation, an approximation of the heat flux q is needed. One can be obtained by considering a constant, uniform temperature field around a single sphere with radius s due to a constant heat flux q at the boundary and constant temperature \bar{T} at infinity. The temperature field also obeys the Laplace equation $\nabla^2 T = 0$; whose solution is given for this symmetric problem by $T(r) = C_1/r + C_2$, where r is the radial distance to the sphere center and C_1 and C_2 are determined by the boundary conditions. The boundary condition $T(\infty) = \bar{T}$ leads to $C_2 = \bar{T}$ and the heat flux boundary $\partial T(r)/\partial r|_{r=s} = -q/k_T$ leads to $C_1 = qs^2/k_T$. Then, the temperature field is given by

$$T(r) = \frac{qs^2}{k_T} \frac{1}{r} + \bar{T}, \quad (4.25)$$

from which the corresponding heat flux as a function of r can be obtained as

$$q(r) = \frac{T(r) - \bar{T}}{s^2} k_T r. \quad (4.26)$$

For a unit sphere ($s = 1$) and temperature T_h at its boundary $r = s$ it follows that

$$q(s) = (T_h - \bar{T}) k_T. \quad (4.27)$$

This is used as an approximation for the flux boundary condition corresponding to a surface temperature T_h . This approximate description is consistent with the simulations performed here, where the constant surface temperature T_h is imposed.

4.1.4 Single Dimer Dynamics

4.1.4.1 Swimming Velocity

The construction parameters $\gamma = s_p/s_h$ and δ_b will influence the swimming behavior of the dimer. Before discussing these, a consideration of finite size effects is in order. The size of the simulation box will influence the propulsion velocity through its effect on the surrounding fluid. Figure 4.3 shows simulation results for a symmetric dimer with $\gamma = 1$ at two bead sizes. The box size dependence is given in terms of the functional form

$$v_s = v_\infty \left(\lambda_L \frac{l_s}{L} + 1 \right) \quad (4.28)$$

where v_s is the propulsion velocity measured along the main axis of the dimer, $l_s = 2s_p + 2s_h + \delta_b$ the length of the swimmer, L the side length of the cubic simulation

box. v_∞ and λ_L are free parameters, the former of which giving a theoretical value for the propulsion velocity in an infinitely large simulation box. The swimmer with

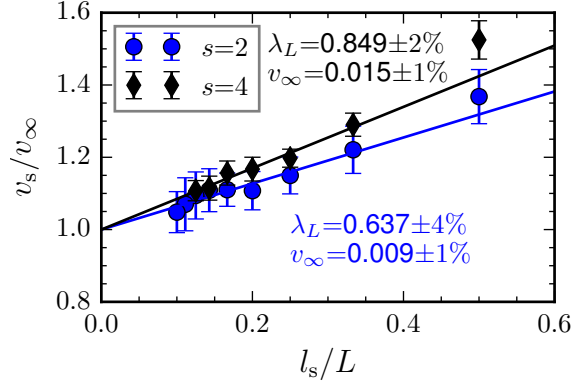


Figure 4.3: Propulsion velocity v_s of a symmetric thermophilic dimer with $\gamma = 1$ and either $s_p = 2$ or $s_h = 4$. v_∞ and λ_L correspond to the free parameters of eq. (4.28).

larger beads propels faster, which in turn leads to a stronger finite size effect, i.e. a higher value of λ_L . In both cases however, with the exception of very small box sizes ($l_s/L = 0.5$), a linear behavior is obtained. A precise quantification of finite size effects is in principle necessary for each different construction of dimers to determine v_∞ . However, as simulations at large box sizes are very expensive and the influence of the box size can be captured with a linear description, such a quantification is not performed for all the cases to be discussed in the following. Instead, for all single swimmer simulations discussed in the following, typically $l_s/L = 0.2$ is chosen as box size, keeping in mind that this will overestimate the theoretical unbounded value around 10 – 20 %. Since this overestimation is systematic and linear, conclusions may still be drawn when comparing different realizations.

In terms of varying size ratio γ , there are two effects determining the velocity. For a fixed size of the phoretic bead, a larger hot bead will lead to a stronger temperature gradient, which will increase the propulsion velocity. At the same time, it will also increase its friction, such that a maximum at intermediate values is expected. For the limiting cases of an infinitely small or large hot bead, the swimming velocity should be zero.

Concerning the bond length, similar considerations hold. A short bond length will put the beads in closer contact, which will increase the gradient at the phoretic bead and with it the swimming velocity. But as soon as the beads start overlapping, the phoretically active area is reduced. These effects are expected to balance out, such that again a maximum is expected. In the limiting case of complete overlap there is no phoretically active area left, while for infinite separation no temperature gradient is felt anymore. Both cases lead to vanishing swimming velocity.

This physical behavior was mostly confirmed for chemical swimmers [76], with the exception that no maximum in the dependency on bond length was found

there, most likely because no overlapping constructions were considered. These are however likely to occur in experiments. Many of the synthesized dimers of Valadares et al. [19] (c.f fig. 1.4a) give the impression that their catalytic bead is partly "molten" onto the phoretic bead, which would in simulations correspond to a certain overlap.

Figure 4.4 shows simulation results on how varying size ratio and bond length influences the swimming velocity, where the qualitative behavior described above is clearly observed. The thermophilic case considers a construction which closely matches that of the chemical swimmer of Reigh and Kapral [76] in order to enable an approximate comparison of results to it. The thermophobic dimer considered in fig. 4.4a is constructed with different parameters for s_p and $\delta_b = 0$, such that their influence on the obtained behavior can be seen.

For a quantitative comparison, consider first the values obtained in simulations, shown with solid symbols in fig. 4.4. Overall, the expected maximum for intermediate values of both γ and δ_b is obtained. Notably, for δ_b it lies about where the beads halfway overlap. In terms of the normalized behavior, no difference is seen for the different parameters employed modeling the thermophilic and thermophobic dimer. To estimate the influence of the thermostatting procedure, it was also checked whether it makes a difference to use $s_h < r < 1.08s_h$ or a constant width $s_h < r < s_h + 0.2$ to apply the thermostat to. The absolute velocities differ then (yellow markers in fig. 4.4b), but in terms of the normalized velocities shown in fig. 4.4a the physical behavior is identical. The chemical swimmers, though leading to identical behavior to that of thermal swimmers in terms of varying δ_b when normalized velocities are considered (fig. 4.4c), show a different course in their normalized velocity's dependence on γ . For the thermal dimers, the maximum lies at around $\gamma = 1.7$ and is very flat, showing a variation of only around 20 % for $0.8 < \gamma < 3$, indicating that their propulsion velocity is not very sensitive to this construction parameter. The chemical dimer shows more pronounced variations around 60 % and a very broad maximum with a peak value at ca. 2.0.

Based on these results, $\delta_b = 0$ was chosen for most of the dimers studied in this work, as it leads to faster swimming which reduces simulation time. Furthermore, the experimental realization of Valadares et al. [19] suggests that in an experimentally realizable system, the beads will be close together or even overlapping.

The theoretical predictions for chemical swimmers follow the course of the simulated measurements quite well in terms of both normalized and absolute velocities, especially concerning variations in δ_b . For thermal dimers, this is not the case in terms of the absolute velocities, as visible in fig. 4.4b. Especially in case of the thermophobic dimer, the predictions differ by a factor of ca. 3 from the measured velocities. These differences are attributed to the quite strong approximations involved in deriving eq. (4.23), which amount to ignoring any spatial variations in temperature and density, except for the temperature gradient, as well as assuming uniform and constant pressure. Better agreement is expected when these factors are accounted for, like in the case of single colloids in temperature gradients discussed in chapter 3, whose predicted drift velocities overall matched quite well those

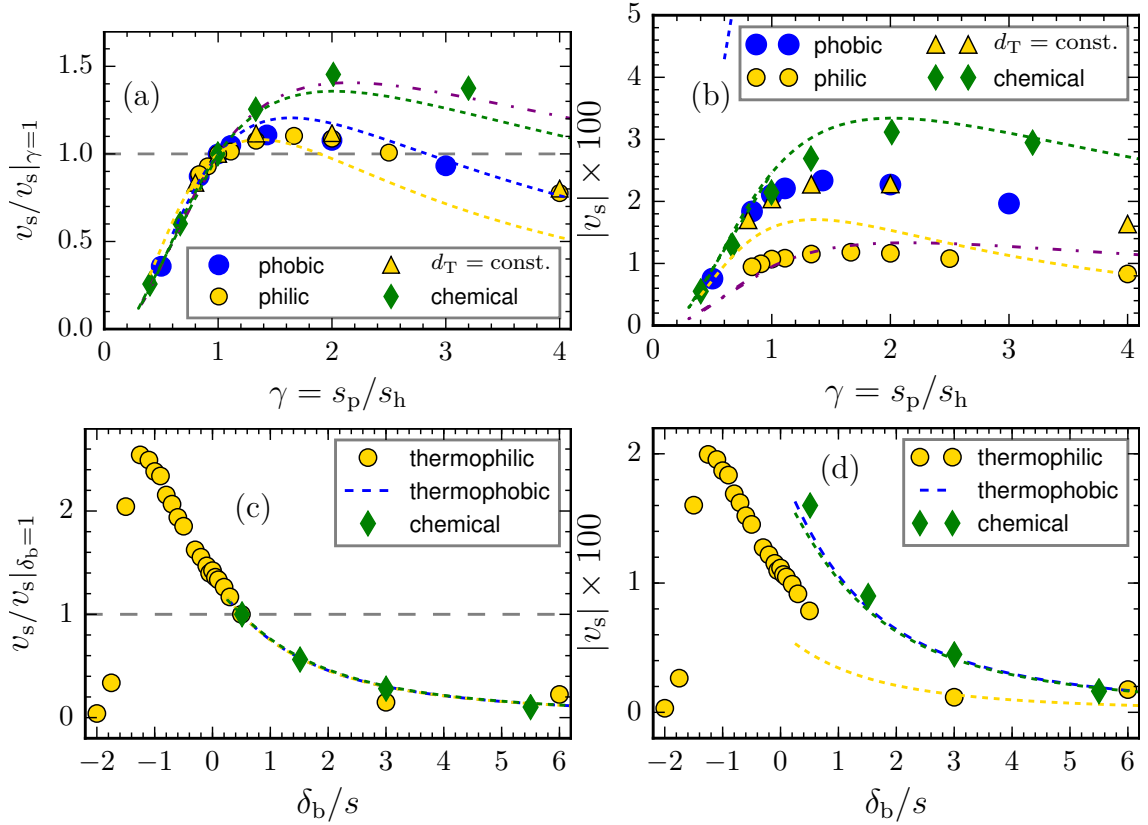


Figure 4.4: Swimming velocities v_s of dimer swimmers as a function of construction parameters γ (a,b) and δ_b (c,d)). Data for thermophobic (blue), thermophilic (gold) and chemically attractive (green) dimers is shown. Dashed lines are theoretical predictions based on the framework developed in section 4.1.3. **a,b)** For the thermophilic dimer, $s_p = 4$, $\delta_b = 0.8$ and $T_h = 1.3$ are chosen. $s_p = 3$ and $\delta_b = 0.5$ have been used for the chemical one¹. The thermophobic dimer has $s_p = 6$ and $\delta_b = 0$. The purple dashed-dotted line uses a thermophilic dimer with a heat flux boundary condition eq. (4.24) matched to the numeric value of that of the chemical one $(\nabla c_A \cdot \tilde{\eta})_{\eta=\eta_1} = -\bar{k}_0 c_0 / D \approx 77.82$, as well as the same construction parameters. **c,d)** The dimers considered have $s_h = s_p = 2$. $T_h = 1.5$ is used for the thermal ones. All theoretical predictions use the same parameters as simulations, except for the thermophobic case where $\delta_b = 0.5$ is used. The corresponding heat flux is approximated using the employed T_h in eq. (4.27). Simulation results on chemical swimmers are taken from [76].

¹In the publication [76], δ_b is not explicitly given for this dataset. $\delta_b = 0.5$ reproduces fig. 3a of that paper and is therefore taken here.

obtained in simulations.

Theory and simulations agree in terms of normalized behavior quite well for thermal dimers, comparable to or even better than observed for chemical dimers.

This indicates that the essential physical mechanism is captured in the theoretical description, and it is merely the quantitative values that are deviating due to the simplifications involved in eq. (4.23).

The course of the normalized velocities as a function of γ is to a high degree dependent on the boundary conditions. These constitute the main difference for the thermophobic and thermophilic dimer shown in fig. 4.4a. Though the simulation results collapse upon normalization, the theoretical descriptions do not. This is due to the different heating temperatures employed, namely $T_h = 1.5$ for the thermophobic and $T_h = 1.3$ for the thermophilic dimer. These lead to the heat fluxes being different, and thereby to different courses. Employing the same values for T_h leads to identical predictions. The property mainly determining the course of $v_s(\gamma)$ in fig. 4.4a is then the ratio of source strength to diffusion, which is given by $\underline{k}_0 c_0 / D$ in case of the chemical swimmer and in terms of q/k_T for thermal swimmers and constitutes the main difference between thermophoretic and chemical swimmers. To illustrate this, one can plug in numerically identical values for the boundary conditions of thermal and chemical swimmers. The absolute velocities then differ due to the different expressions for slip velocity, but a good match in terms of the normalized behavior of $v_s(\gamma)$ is obtained (c.f. green and purple lines in fig. 4.4a).

As the shape of the normalized behavior is to such a large degree dependent on the boundary conditions, approximating them needs careful consideration. Instead of using approximations to obtain them, it is also possible to fit them to the simulation measurements, whereupon near-to perfect agreement can be obtained in terms of normalized behavior (not shown).

From these observations, it is concluded that the differences in the course of $v_s(\gamma)$ are not a question of which phoretic mechanism is employed. Rather, it is the distribution of the phoretic field that determines their behavior. If the numerical values of thermal diffusion and species diffusion were identical, a very similar behavior would be observed. As they are not, the diffusion of the temperature field ($D_T \approx 0.154$) is about a factor three faster than the diffusion of the concentration field ($D = 0.0514$). This leads to less pronounced variations along the phoretic particle's surface when the hot bead's size is changed, such that a flatter course of $v_s(\gamma)$ is obtained.

4.1.4.1.1 Fixed Size of Hot Bead It is as well of interest to consider what happens when instead of the phoretic bead's size, the size of the hot bead is fixed and the phoretic bead's radius is varied. As shown in figs. 4.4a and 4.4b, a fixed size of the phoretic bead leads to a maximum in velocity for intermediate size ratios γ . Reigh and Kapral report an approximately logarithmic increase of velocity with increasing the phoretic bead's size when instead the hot bead's size is fixed [76]. Such behavior is consistent with simulations of thermophoretic dimers, as shown by the red circles in fig. 4.5a. The question this poses is whether there is an inherent difference in between the two, or if there exist a possible normalization capturing both of these behaviors. The main considerations that determined the behavior

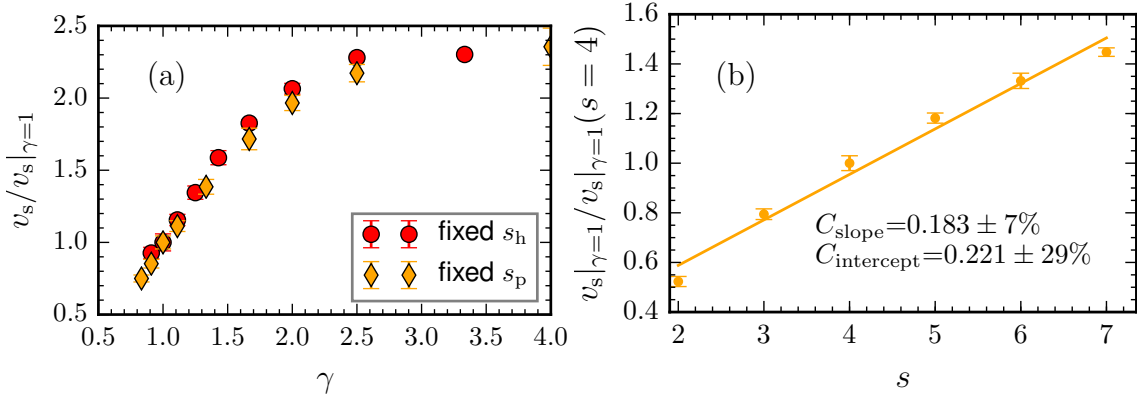


Figure 4.5: **a)** Propulsion velocity v_s of a symmetric thermophilic dimer as a function of γ when the hot bead's size is fixed. Data from simulations with fixed hot bead's size of $s_h = 2$ (red circles) and with fixed phoretic bead's size of $s_p = 4$ (orange rectangles), the latter remapped to the case of fixed hot bead's size. **b)** Dependence of the propulsion velocity v_s on the bead size s of a symmetric ($\gamma = 1$) thermophilic dimer. Solid line is a fit to a linear function $v_s/v_s(s=4) = C_{\text{slope}}s + C_{\text{intercept}}$ with free parameters $C_{\text{slope}}, C_{\text{intercept}}$ given in the plot.

for the fixed phoretic bead size were that, enlarging the hot bead, the temperature gradient is felt more strongly at the phoretic bead while at the same time the friction increases with the bead size as well. These should be the same for every value of γ , independent on whether the hot or phoretic bead is viewed as fixed. The additional effect accounting for the different course when the phoretic bead's size is varied is that the colloid-fluid interaction of this bead determines also the strength of the phoretic effect, such that one measures a curve where the thermal diffusion factor is different at each point. The effect this has on the propulsion velocity should be visible when the overall swimmer size is varied. Simulation results on the overall swimmer size dependence, using a box size of $l_s/L = 0.25$, and a linear fit to it are shown in fig. 4.5b. The size dependence of the swimming velocity is in fact well captured by a linear relation for the (intermediate) sizes considered here, which emerges as a balance between the friction and the thermal diffusion factor, which both rise with the overall size, the latter though only dependent on the phoretic bead.

To compare now the two behaviors of fixed phoretic and hot bead, a common reference point is needed. Such reference is provided by the propulsion velocity of the same-sized dimer with $\gamma = 1$, which is a common point whether the hot or the phoretic bead is regarded as fixed. Two simulation data sets are considered to make the comparison. One is the red data shown in fig. 4.5a, which uses a fixed size of the hot bead of $s_h = 2$ and a box size of $l_s/L = 0.25$. The other uses a fixed size of the phoretic bead $s_p = 4$ when varying γ and a box size of $l_s/L = 1/3$. To map the latter to the behavior of the data set with fixed size of the hot bead, the velocity of each fixed-phoretic data point is divided by the velocity of a same-sized

reference dimer which features a phoretic bead of the same size as the hot bead this data point considers. This velocity is not measured in a different simulation, but obtained from a fit to the same-sized dimer's velocity's dependence on the bead size s of fig. 4.5b. With the fit parameters at hand, the velocity of a same-sized dimer with arbitrary s can be calculated and used to normalize the fixed-phoretic data points. The resulting curve has to be normalized again, accounting for the different velocities that result from the different box sizes used in obtaining the fit parameters from fig. 4.5a and the actual data points. This normalization is given by the ratio of the swimmers' velocities at $\gamma = 1$ and $s_p = 4$.

As a result of this procedure, the (orange) curve, obtained with fixed phoretic bead size, can be converted quite well to that obtained with fixed hot bead size (red) in fig. 4.5a. The same procedure may also be performed in reverse, i.e. converting a data set obtained for fixed hot bead size to the behavior of fixed phoretic bead size. The good agreement obtained in fig. 4.5a, although different values for $s_{h,p}$ and different box sizes indicates the robustness of the simulation results against changes in both bead and box size, as these are well accounted for by normalization. It also confirms the assumption that the seemingly different behaviors obtained for the propulsion velocity as a function of size ratio when the hot or the phoretic bead are fixed can be explained considering that a change in the phoretic bead's also changes the strength of the thermophoretic response.

4.1.4.2 Hydrodynamics

As shown in the last section, the thermal dimer's propulsion velocity is not very sensitive to changes in the size ratio $\gamma = s_p/s_h$ in the most reasonable range of $1 \leq \gamma \leq 3$. However, the size ratio will not only influence the swimming velocity, but also the hydrodynamic behavior. Representative flow fields for several size ratios of both thermophobic as well as thermophilic dimers are shown in fig. 4.6.

Consider first only the simulation measurements in figs. 4.6a to 4.6c and 4.6g to 4.6i. The obtained flow fields show qualitative differences in hydrodynamic behavior upon variation of γ . Visible is first that the flow field adapts to γ by changing mainly its lateral part. Lateral means the flow velocity in direction of the axis crossing the center of the phoretic particle and perpendicular to the propulsion direction, i.e. the l -axis shown in fig. 4.2a. This lateral flow pattern changes from mainly hydrodynamic repulsion for a symmetric construction (fluid flowing away from the bead, see fig. 4.6a) to lateral hydrodynamic attraction for an asymmetric construction with smaller hot bead (c.f. fig. 4.6c). The laterally attractive lobe that develops around the phoretic bead upon shrinking the hot bead's size enlarges with rising γ . The behavior is vice versa for the thermophilic swimmer, though a bit less pronounced as the two lobes around the beads can not be made out as clearly as in the case of thermophobic dimers. The flow changes from being laterally attractive for a symmetric construction to lateral repulsion for the asymmetric build. Additionally, for symmetric thermophobic and, though less visible, asymmetric thermophilic swimmers, a short-range hydrodynamically attractive part is

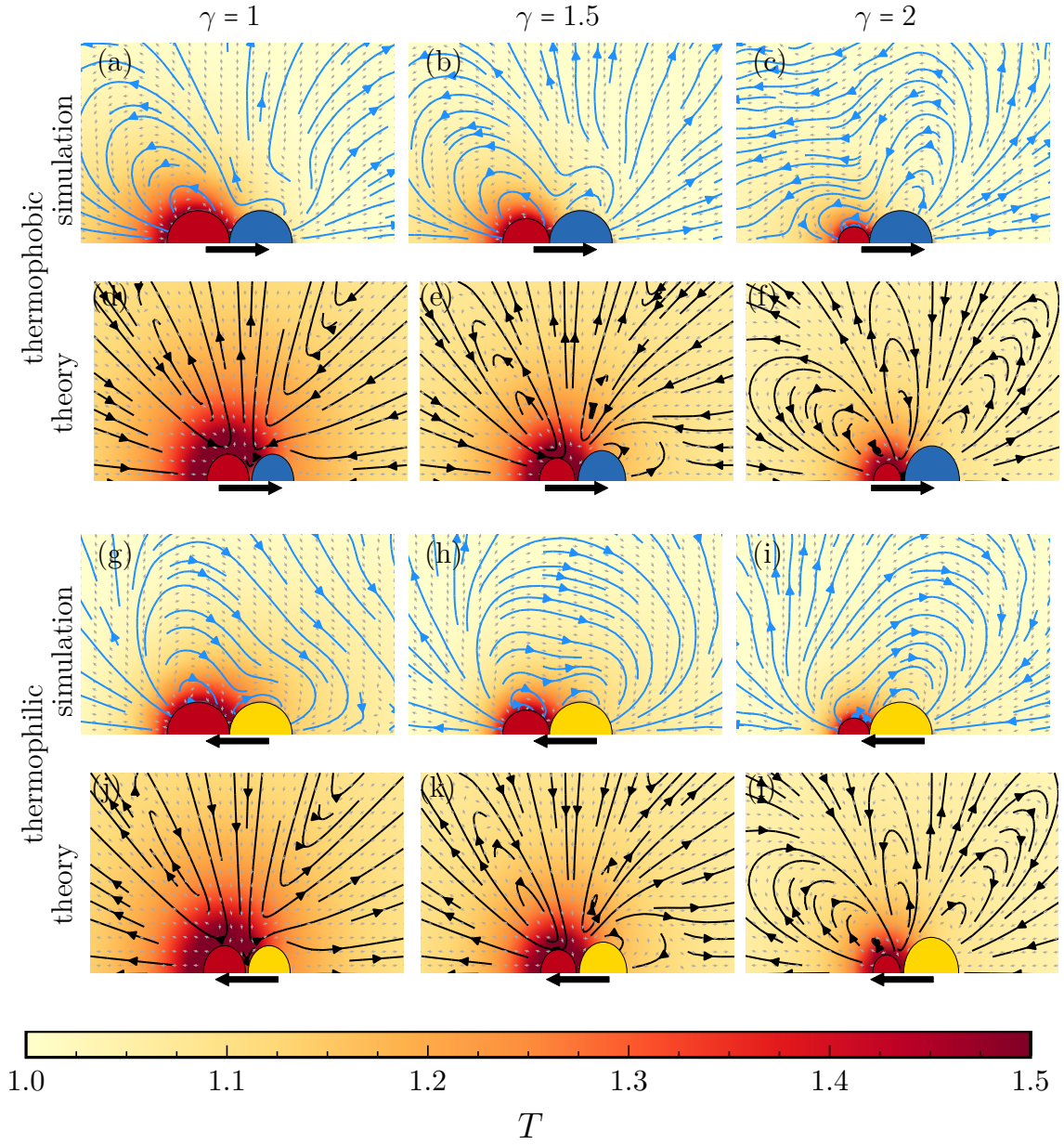


Figure 4.6: Simulated (blue lines) and theoretical (black lines) flow fields of thermophobic (a),b,c) and thermophilic (g),h,i) dimers. The corresponding velocity field is shown with gray arrows, background depicts the temperature field. Black arrows indicate the propulsion direction. The size of the phoretic bead is fixed at $s_p = 4$, while $\gamma = s_p/s_h = 1; 1.5; 2$ (left, middle, right). The rows below the simulation measurements show theoretical predictions based on the thermophoretic variant of the approach of Reigh and Kapral [76], where d),e),f) correspond to a),b),c). j),k),l) correspond to g),h),i).

present as evident from the short lobe at the respective front bead.

The flow fields of thermophoretic dimers are of the force-dipole type [76]. Force-dipole type flow fields are characterized in terms of their axial hydrodynamic flow as either pushers, when fluid is pushed outwards in axial direction, or pullers, when it is pulled inwards [9]. Pusher behavior of a force-dipole means also that the lateral part is hydrodynamically attractive, with fluid streaming towards the swimmer, while the flow of a puller will be laterally repulsive. In terms of their lateral characteristics, the symmetric thermophobic dimer of fig. 4.6a is then mainly a puller-type of swimmer, while the symmetric thermophilic dimer shows behavior more reminiscent of a pusher. Upon shrinking the hot beads size, the main characteristics of lateral hydrodynamics change direction in both cases, such that a thermophobic dimer is converted from puller to pusher while a thermophilic one is converted from pusher to puller.

A quantification of these hydrodynamic behaviors in terms of lateral attraction and repulsion can be obtained by measuring the flow velocity along the l -axis. For further comparison to the theoretical predictions, the flow in axial direction with origin in the dimer center is characterized as well (a -axis in fig. 4.2a). These quantifications are shown in fig. 4.7. In terms of theoretical predictions, consider first the approach of Yang et al. [25], using additive, independent flow fields for the two beads based on eq. (4.1). Its results are shown with dashed lines in fig. 4.7 for different constructions of thermophobic dimers. Thermophilic swimmers show nearly identical behavior, though vice versa in terms of flow direction, and are omitted in the discussion for now. The cases of interest here, as opposed to what has been used by Yang et al., feature no separation in between beads as well as asymmetric types of construction. Figure 4.7a shows the flow field of a thermophobic symmetric swimmer with comparable parameters to those of Yang et al. [25], except for the beads touching and that bigger beads are considered. The quantitative agreement to theory, especially in the lateral part, is worse than previously observed [25]. This is attributed to the assumption of independent flow fields of the two beads breaking down upon close contact of the constituent beads. Agreement also is a bit worse for faster swimming dimers, when the heating temperature around the hot bead is increased to $T_h = 1.5$, as visible in fig. 4.7b for the flow velocity to the rear (light blue). The flow fields of symmetric thermophobic dimers show short-ranged hydrodynamic attraction (negative v_l) close to the phoretic bead, whose range is strongly underestimated by the theoretical prediction (red dashed lines in figs. 4.7a and 4.7b stay positive while simulation data reaches negative values). Overall however, the already pointed out hydrodynamic behavior in terms of lateral repulsion (i.e. mainly positive lateral flow velocities v_l) is predicted correctly with more or less quantitative deviations for symmetric constructions. This changes when asymmetric constructions are considered. As already evident from the visual depictions of the flow fields in fig. 4.6, the hydrodynamic behavior changes from lateral repulsion to long-ranged attraction in the case of thermophobic dimers. This is not captured by this theoretical approach, which predicts lateral repulsion instead of attraction as shown in fig. 4.7c. Even when the two beads are far apart, such that

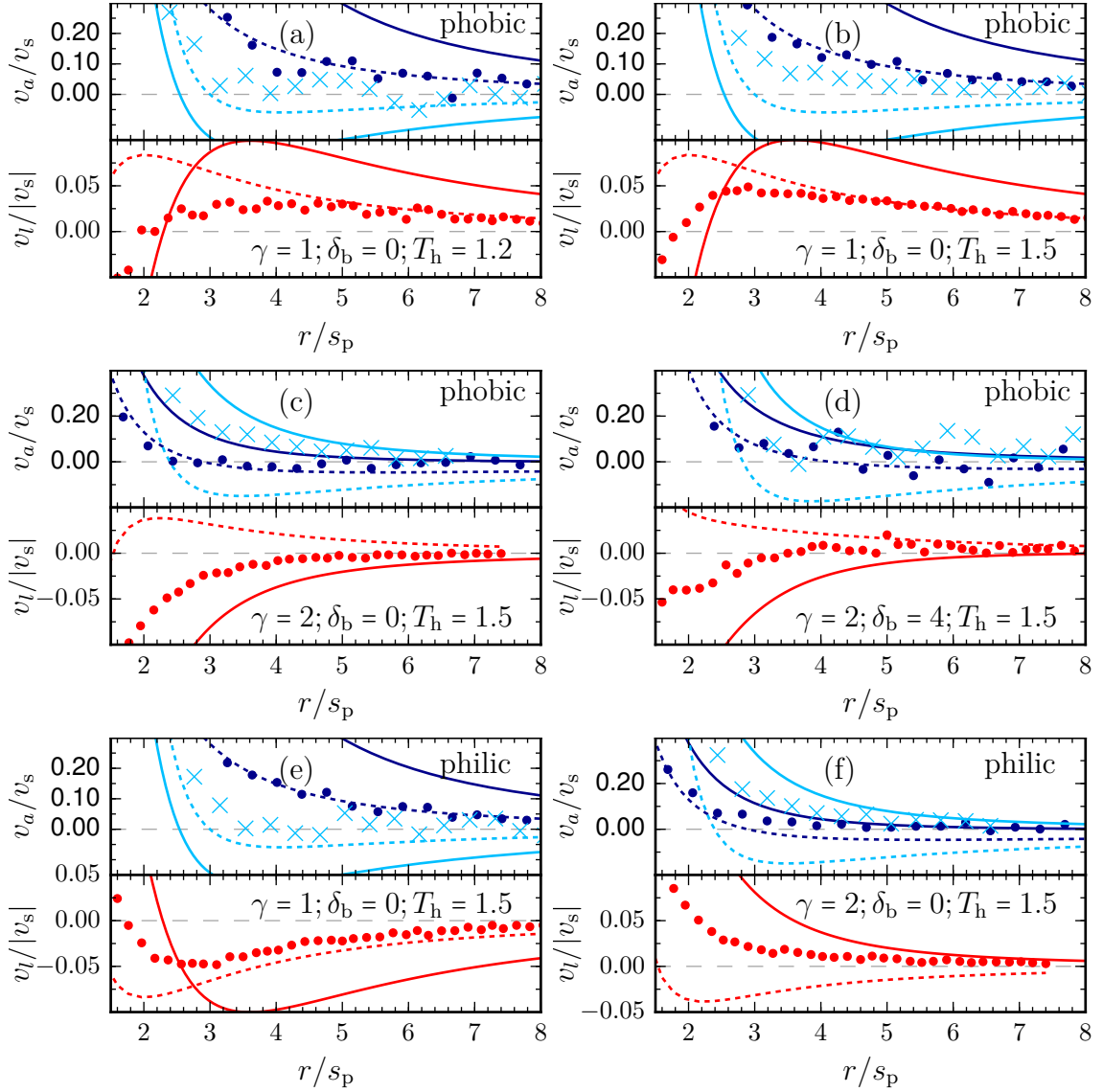


Figure 4.7: Flow velocity around dimers with fixed size of the phoretic bead $s_p = 4$ measured along the a -axis and l -axis as shown in fig. 4.2a. The axial flow velocity v_a is measured in moving direction to the front (dark blue) and rear (light blue) of the dimer. The lateral flow velocity is denoted v_l (red). Flow velocities are normalized by the swimmer velocity v_s and the distance r is normalized by the phoretic bead radius s_p . Theoretical predictions use the approach of Yang et al. (dashed lines) and the thermophoretic variant of the framework of Reigh and Kapral (solid lines). For the latter, $\delta_b = 0.5$ is used. All other parameters used are identical to those employed in simulations. **a)** Symmetric thermophobic dimer with $\gamma = 1$, $\delta_b = 0$ and heating temperature $T_h = 1.2$. **b)** Symmetric thermophobic dimer with $\gamma = 1$, $\delta_b = 0$ and $T_h = 1.5$. **c)** Asymmetric thermophobic dimer with $\gamma = 2$, $\delta_b = 0$ and $T_h = 1.5$. **d)** Asymmetric thermophobic dimer with $\gamma = 2$, $\delta_b = 4$ and $T_h = 1.5$. **e)** Symmetric thermophilic dimer with $\gamma = 1$, $\delta_b = 0$ and $T_h = 1.5$. **f)** Asymmetric thermophilic dimer with $\gamma = 2$, $\delta_b = 0$ and $T_h = 1.5$.

the assumption of independent flow fields is more likely to hold, the change in hydrodynamic behavior is not captured. This is the case considered in fig. 4.7d. The hydrodynamic behavior of asymmetric constructions therefore cannot be predicted with this approach of Yang et al..

The thermophoretic variant of the approach of Reigh and Kapral offers a qualitatively better description of the flow fields. Graphical depictions of the flow patterns are shown in figs. 4.6d to 4.6f and 4.6j to 4.6l, and a quantitative characterization is shown in fig. 4.7 with solid lines. Though the quantitative and even qualitative agreement of this approach to simulation measurements is, in the axial part, in many cases worse than that of Yang and Ripoll, it does capture the change in lateral hydrodynamics qualitatively correct, as already visually evident in fig. 4.6. The quantitative deviations are likely attributable to the strong approximations used in deriving eq. (4.23) as well as in obtaining the boundary conditions, as also discussed in the context of the construction parameters' influence on swimming velocity in section 4.1.4.1. Furthermore, using zero separation in between the beads is not possible in the theoretical approach, such that a short inter-separation has to be chosen for comparison.

In simulations of Yang et al. [25], it was observed that the flow fields of thermophilic and thermophobic dimers are in principle reverse versions of each other, i.e. the streamlines are the same but have inverted directions when the propulsion direction changes. This behavior is also obtained in the analytical calculations, by both theoretical approaches, and visually evident in figs. 4.6d to 4.6f when compared to figs. 4.6j to 4.6l. However, this symmetry is only approximately captured in the simulation measurements, as visible in the comparison of figs. 4.6a to 4.6c to figs. 4.6g to 4.6i. There, the streamlines of thermophobic and thermophilic dimers are not reverse versions of each other, though the general form is similar. Since this symmetry was captured in the simulations of Yang et al., its disappearance stems most likely from the close contact of the beads considered in simulations here.

Another feature of the flow fields that is different in theory and simulations is the existence of a third lobe near the center of the dimer, which is observed in the theoretical predictions for the most asymmetric construction considered. In simulations, the flow lines enclose the whole dimer and no such lobe emerges. Likely, this is also attributable to the close contact of the two beads in simulation.

As already pointed out, the theoretical predictions for the flow fields of thermophobic and thermophilic are just reverse versions of each other. Since this symmetry only approximately obtained in simulations, a quantitative comparison between theory and simulation is also of interest for the thermophilic case and shown in figs. 4.7e and 4.7f. As compared to the thermophobic case, the opposite behavior in terms of lateral hydrodynamics is quite evident. The symmetric thermophilic dimer features mainly lateral repulsion, while the asymmetric features attraction. The main observations made in terms of the agreement of theory and simulations made in the discussion on thermophobic dimers also hold here. While the approach of Yang et al. describes the behavior of symmetric dimers, and in this thermophilic case clearly better than that based on the Reigh and Kapral framework, it fails

to capture the qualitative change in lateral hydrodynamics when asymmetric constructions are considered. Within the Reigh and Kapral framework, this change is seen for thermophilic dimers as well.

4.2 Janus Particle

4.2.1 Introduction

Several models exist to perform simulation studies on Janus particles. A first simple approach is a model of an active particle, introducing an orientation vector with rotational dynamics to a spherical particle and applying either a driving force or defining a constant velocity along that direction to account for self-propulsion, similar to what has been described in section 1.2.1. These systems already show MIPS and can correspond to what is also experimentally observed, for example the catalytic Janus swimmers in [10]. Solvent effects are however not taken into account in such approaches. Hydrodynamics have shown to be a relevant factor in many systems. In particular, the difference between pullers and pushers has shown to result in very different collective dynamics. With this motivation, the squirmer model, originally aimed at a description of bacterial microswimmers, was used to describe Janus particles. In the squirmer model, the hydrodynamic flow field is subscribed to the particle surface by a certain collision rule with fluid particles. This approach was taken for example in [81, 82] for MPC.

Other models more inspired in synthetic colloids include constructing the Janus particle out of many beads and treat both their dynamics as well as the fluid with molecular dynamics [83], DPD [84]. Similar constructions were also considered in MPC [85]. Delfau et al. employ a "smooth-profile" method based on the Navier-Stokes equation to describe squirmers [86].

4.2.2 Model

In this work, the model of Yang et al. is used to describe Janus swimmers [25]. It combines a spherical particle with an orientation vector updated through bounce-back collisions of point-like fluid particles. This is combined with a simultaneous explicit description of colloid-fluid interaction through pairwise potentials. To enable both, bounce-back collisions are performed at a pairwise distance s_{bb} , while the interaction potential's range is chosen a bit longer, in such a way that a significant amount of fluid particles still reaches the bounce-back range. As discussed in section 3.4.4, a pure bounce-back rule corresponding to a hard sphere model is insufficient to produce the desired thermophoretic effect. The introduction of soft potential interactions is necessary to be able to include tunable thermophoretic effects.

The bounce-back collisions are derived from elastic collisions of point-like particles with a rotating large particle's surface. The Janus particle therefore features,

besides position \mathbf{R} , velocity \mathbf{V} and mass M , also an orientation \mathbf{e} and an angular velocity $\boldsymbol{\omega}$. A fluid particle has position \mathbf{r} , velocity \mathbf{v} and mass m . The two particles collide when their separation distance $|\mathbf{S}| = |\mathbf{r} - \mathbf{R}|$ falls below a threshold value, which is taken to be the range of the molecular interaction potential $s = \sigma_{cf} + \Delta_{cf}$. The Janus colloid then has a moment of inertia $I = \xi_I M s^2$ with $\xi = 2/5$. The relative velocity of Janus and fluid particle is given by

$$\tilde{\mathbf{v}} = \mathbf{v} - \mathbf{V} - \boldsymbol{\omega} \times \mathbf{S} \quad (4.29)$$

which is the relevant quantity for the collision process. To conserve linear and angular momentum, the post-collision velocities read as

$$\mathbf{v}' = \mathbf{v} - \mathbf{p}/m \quad (4.30)$$

$$\mathbf{V}' = \mathbf{V} + \mathbf{p}/M \quad (4.31)$$

$$\boldsymbol{\omega}' = \boldsymbol{\omega} + (\mathbf{S} \times \mathbf{p})/I. \quad (4.32)$$

The momentum exchange \mathbf{p} is expressed in terms of the normal and tangential components of the contact velocity $\tilde{\mathbf{v}}$ given by $\tilde{\mathbf{v}}_n = \hat{\mathbf{S}}(\hat{\mathbf{S}} \cdot \tilde{\mathbf{v}})$ and $\tilde{\mathbf{v}}_t = \tilde{\mathbf{v}} - \tilde{\mathbf{v}}_n$, where $\hat{\mathbf{S}} = \mathbf{S}/|\mathbf{S}|$. It is determined by the conservation of energy and stick boundary conditions, i.e. $\tilde{\mathbf{v}}'_n = -\tilde{\mathbf{v}}_n$ and $\tilde{\mathbf{v}}'_t = -\tilde{\mathbf{v}}_t$, leading to

$$\mathbf{p} = \mathbf{p}_n + \mathbf{p}_t = 2\mu\tilde{\mathbf{v}}_n + \frac{2m_r\xi_I M}{\xi_I M + m_r} \tilde{\mathbf{v}}_t \quad (4.33)$$

with the reduced mass $m_r = mM/(m + M)$.

To facilitate both faster production runs for parameter screening as well as offering the possibility to perform simulations of ensembles of many Janus particles within a reasonable amount of time, a parallelized version of this model was implemented in LAMMPS in the scope of this work.

To model thermophobic Janus particles, the soft potential was chosen according to eq. (2.7) with parameters (2.5, 0, 1, 24, a), while to obtain thermophilic behavior, (2.5, 0, 1, 3, r) was used. These are the values also used in [25]. The heating procedure also follows what is described there, i.e. rescaling around the hot side in a layer of $0.08s$ to a fluid temperature of $T_h = 1.25$. The MPC fluid parameters are chosen identical to those for single dimers, as described in section 4.1.1.

4.2.3 Single Particle Dynamics

4.2.3.1 Swimming Velocity

The construction of a Janus particle offers one degree of freedom, which is the coating angle θ_c describing how much of the surface is covered with material reacting to (laser) illumination, i.e. is heated in the context of simulations. Also, the type of material used for the phoretically active side of a thermophoretic Janus will determine the reaction to a temperature gradient, which can again be either

thermophilic or -phobic. Simulations are performed to study the dependency of the single swimmer dynamics and flow fields on the coating angle. Figure 4.8a shows the self-propelled velocity of the Janus as a function of the coating angle θ_c , normalized by the maximum velocity $v_{s,\max}$ reached. The maximum velocities are dependent on the colloid-fluid potential, leading to $v_{s,\max} = 0.00065$ for the thermophilic and $v_{s,\max} = 0.00369$ for the thermophobic Janus. There are two limiting cases in the dependence of self-propulsion on coating angle. For no coating ($\theta_c = 0^\circ$), there is no temperature field produced and the particle is just a colloid performing Brownian motion. For complete coverage ($\theta_c = 180^\circ$), there is no phoretically active surface and the particle is a hot Brownian particle. Somewhere in between, there should be a maximum in propulsion velocity, whose location depends on the precise interplay between the temperature distribution in terms of the gradient and the phoretic effect, which is determined by the interaction potential. High velocities are obtained for both thermophilic and -phobic Janus particles over a rather broad maximum around $\theta_c = 60 - 100^\circ$. The distribution is not symmetric around 90° , but tilted towards smaller coating angles. This implies that for efficient propulsion, it is of greater importance to have more phoretically active surface. The broad maximum in propulsion velocity is similar to what was also observed for thermally driven dimers (c.f. fig. 4.4).

4.2.3.2 Hydrodynamics

Similar to the thermophoretic dimer, the hydrodynamic flow field around a Janus particle also depends on its geometric construction, which is here determined by the coating angle θ_c . For $\theta_c = 90^\circ$, the Janus colloid is encompassed by a single lobe, representing the symmetric flow field of a neutral swimmer. This is identical to that of a phoretic colloid in an external temperature gradient [25], although the self-propulsion and the phoretic drift velocity will be different. Upon changing θ_c , the position of the lobe adapts, since the hydrodynamic boundary conditions are different for the coated and phoretic part of the surface. A characterization of the flow velocities for thermophobic Janus particles is shown in fig. 4.8b and three representative flow fields, both for the thermophobic as well as -philic case, are shown in fig. 4.8d to i. The effects on the flow field seen for thermophobic Janus are more evident than for the thermophilic one. This is due to the lower absolute swimming velocity of the thermophilic one, which in turn also leads to a weaker flow field. The qualitative effects however are comparable. For lower coating angles, the lobe points in the direction of the phoretic side, which is into the propulsion direction for thermophobic Janus and backwards for thermophilic. Then, enlarging the coating angle, the stage of neutral swimmer is passed and for coating angles above 90° , the lobe is positioned at the hot side of the Janus, i.e. pointing backwards for thermophobic and forwards for thermophilic. In [25], a solution of the Stokes equation based on a phoretic particle in an external temperature gradient, originally derived in [68], is used to predict the flow field of a Janus particle with $\theta_c = 90^\circ$ and shows very good agreement to the measured flow fields. The fluid velocity field is

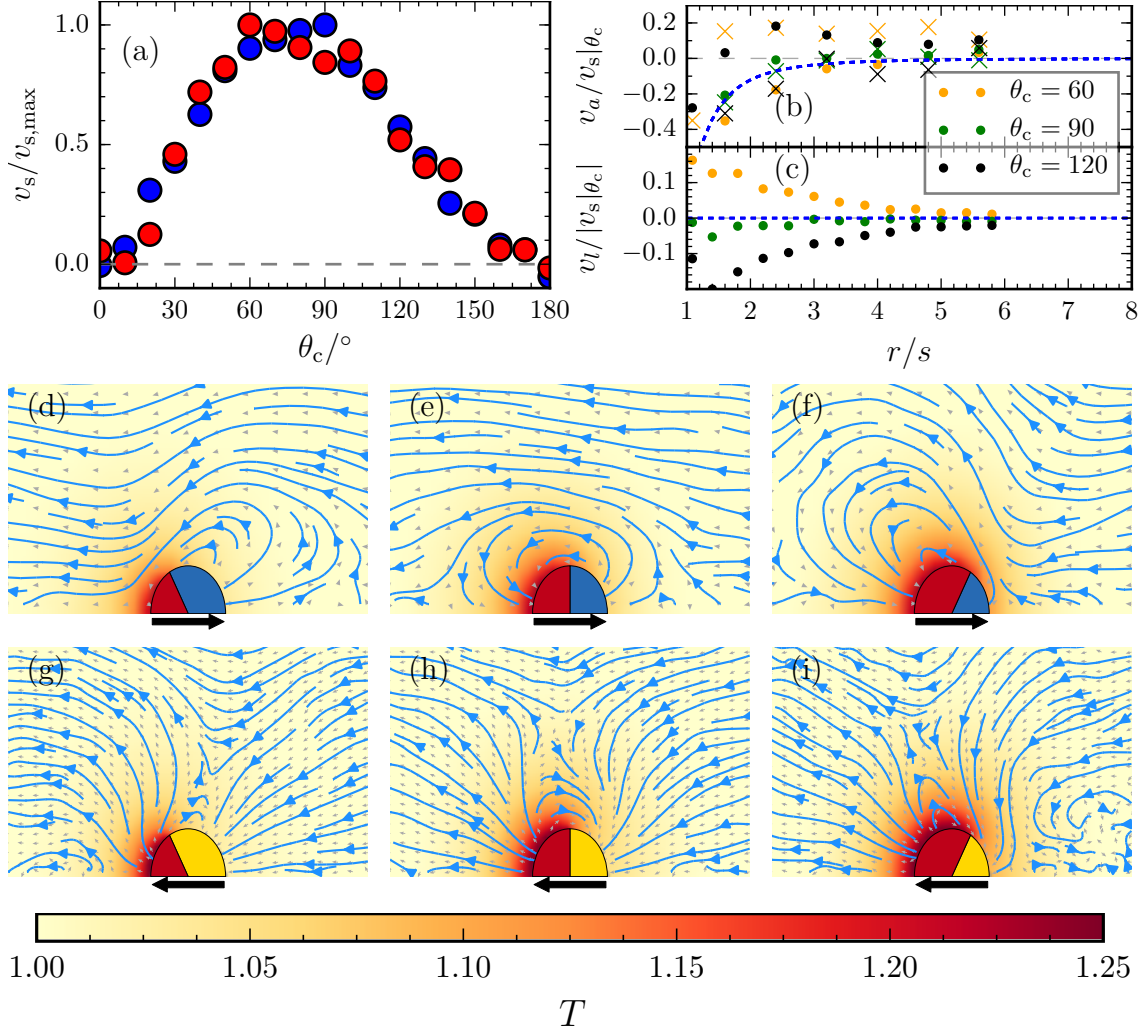


Figure 4.8: **a)** Normalized thermophoretic velocity of thermophilic (red) and thermophobic (blue) Janus swimmer for different surface coverages θ_c .

b,c) Normalized flow velocity along an axis a in propulsion direction (**b**) and perpendicular to the propulsion direction l (**c**), both originating in the center of the Janus particle. Data for thermophobic Janus featuring different coverages. Blue dashed lines are theoretical prediction based on eq. (4.34). **b)** Points denote flow in axial direction to the front, crosses to the rear.

d-i) Flow fields of thermophobic (**d,e,f**); upper row) and thermophilic (**g,h,i**); lower row) Janus swimmers for surface coverage angles $\theta_c = 60, 90, 120^\circ$ (left to right) shown in the swimmer reference frame. Streamlines are shown in blue, the velocity field is depicted with gray arrows. The black arrow indicates the propulsion direction. Background depicts the temperature field.

there given by

$$\mathbf{v}(\mathbf{r}) = \frac{\sigma^3}{2r^3} \left(3 \frac{\mathbf{r}\mathbf{r}}{r^2} - \mathbf{I} \right) \mathbf{v}_s, \quad (4.34)$$

where $r = |\mathbf{r}|$ is the length of \mathbf{r} , the distance from the particle center, and \mathbf{I} denotes the unit tensor. However, that approach could not include any variation of the coating angle and the resulting effect on hydrodynamics, and therefore does not predict the changes observable in the simulations here. It is well visible in fig. 4.8b, that, in agreement to [25], the flow field of the thermophobic Janus with $\theta_c = 90$ is well described by this approach (blue dashed lines match green data). Focusing on the lateral part, the thermophobic Janus changes from lateral hydrodynamic repulsion (puller-like) at low coverages to lateral attraction (pusher-like) at high coverages, with flow velocities at short distances to the particle of about 10 % its propulsion velocity. The magnitude of the change in lateral hydrodynamic behavior suggest that it may have significant influence on the collective behavior of ensembles of Janus swimmers that are not symmetrically coated.

It may be of future interest to obtain better analytic predictions for the flow behavior of Janus particles, and detailed analytic predictions exist already for the flow fields of thermophoretic Janus particles. Bickel and Würger calculated the temperature field around a Janus particle in a continuum model based on solutions of the Laplace equation in two limiting cases [87]. One case considers the hot cap to be so thin as to not have an influence on the resulting field, such that a constant heat flux boundary condition is imposed on that side and no-flux on the phoretic side. The other case considers the thick-cap limit. There, it is assumed that the cap has a thermal conductivity so large it is at constant temperature. The simulation model of Janus particles employed in this work corresponds to the thick-cap limit. Unfortunately, a solution for that is only available when there is heat conduction through the particle, which is not the case in the simulations performed here. Therefore, no comparisons is made in the scope of this work. However, in order to facilitate such comparisons to this theoretical approach, one might change the way in which the Janus particle is modeled. That there is no thermal conduction through the particle is an inherent property of employing pairwise molecular interaction potentials in MPC-MD, such that it is hardly possible to use the thick-cap limit. However, instead of fixing the surface temperature, one could add a defined amount of thermal energy into the fluid in the boundary layer, thereby obtaining a situation that might be well described by the thin-cap limit, in which it is possible to ignore heat transport through the particle just by setting the inner thermal conductivity to zero. This adaption of the computational model is likely much easier than an adapted reworking of the theoretical approach.

4.3 Mapping to Real Units

One of the most important properties of a microswimmer is its self-propelled velocity. Experimentally, these typically lie in the range of $\mu\text{m s}^{-1}$ [20]. Synthesized Janus particles have, depending on the propulsion mechanism, reached velocities in the range of 3 to 110 $\mu\text{m s}^{-1}$. The thermophoretic Janus particle of Jiang et al. has reached around 10 $\mu\text{m s}^{-1}$ [20, 23]. The chemically driven dimer reaches velocities in the range of ca. 2 to 6 $\mu\text{m s}^{-1}$ [19].

In simulation units, the thermophoretic dimers here typically reach velocities around 0.01–0.02. The chemical dimers feature velocities in a very similar range of 0.01–0.03 [76]. Due to the inherent coarse-graining and generality of the simulation approach, all quantities have to be regarded as "typical" for colloidal systems. Still, it is relevant to discuss a possible mapping to real units. Such a mapping provides an estimate of what kind of real-world system can be, or is, modeled with the simulation approach and also validates the simulation approach to some degree. However, there is a certain arbitrariness in choosing reference values and even methods to perform the mapping, as discussed in more detail in [54, 88], and one choice of mapping procedure cannot map all physical quantities to reasonable values in real units at the same time.

To obtain reference values in real units, the one experimental realization of dimeric swimmers of Valadares et al. provides some orientation [19]. The diameter of the phoretically active bead there is roughly 1 μm , which is assumed as a reference size for the simulations as well. Then, a possible approach is to map the mass of the fluid and the temperature to experimental values, enabling the velocity to be expressed in real units. Assuming water as the solvent and taking the corresponding density $\rho = 1000 \text{ kg/m}^{-3}$, the mass of the fluid is calculated as $m_{\text{fluid}} = V_{\text{colloid}}\rho = 4/3\pi r_{\text{colloid}}^3\rho$. From this, assuming an ambient temperature of 300 K, the velocity unit of the simulations is accessible through $v = (k_{\text{B}}\bar{T}/m_{\text{fluid}})^{1/2}$. $r_{\text{colloid}} = sa$ depends on the reference size assigned to it, determining the simulation length scale a . Using $r_{\text{colloid}} = 1 \mu\text{m}$ leads to velocities around 10 to 20 $\mu\text{m s}^{-1}$ for both symmetric and asymmetric dimers. This is slightly faster than the typical velocities reached by the motors of Valadares et al., which are in the range 2.5–6.0 $\mu\text{m s}^{-1}$, though still within the typical range of velocities for microswimmers. The experimental thermophoretic Janus particles feature radii around 1 μm as well, which leads here to mapped velocities in the range of ca. 0.6 to 4 $\mu\text{m s}^{-1}$ which also agrees well with the experimental range. This mapping to experimental velocities leads to a good agreement, which provides a certain validation to the feasibility of the simulation approach.

4.4 Conclusion and Outlook

The behavior of thermally driven dimer and Janus swimmers is discussed in terms of propulsion velocities and hydrodynamic flow patterns. Both change as a function

of the geometric construction of these swimmers, which is the coating angle in case of the Janus or the bead size ratio and inter-bead separation in case of the dimer. The most intriguing feature the variation of these construction shows is their influence on the hydrodynamic behavior, allowing to tune the lateral hydrodynamic in terms of changing between repulsion (puller-like) and attraction (pusher-like). Comparison to theoretical predictions for dimers, as well as to results on chemically driven dimers, show that their behavior is not dependent on the phoretic mechanism used for propulsion, but on the diffusion of the phoretic field, accounting for the different courses observed for thermal and chemical dimers in the dependence of their swimming velocity on the size ratio. It is found that the theoretical approach of Yang et al. [25] does not capture the qualitative change in between lateral hydrodynamic attraction and repulsion, while the thermophoretic variant of the approach of Reigh and Kapral [76] developed here does.

The dimer is chosen for further investigation in the remainder of this work, as its hydrodynamic interactions are stronger and more complex than those of the Janus, featuring for example a cross-over from lateral attraction to repulsion in the flow field of symmetric dimers. The existence of tunable hydrodynamic interactions, especially lateral hydrodynamic attraction, suggest that ensembles of these swimmers may exhibit interesting collective behavior, especially in the thermophobic case, which combines it with axial phoretic repulsion.

5 Dynamics of Pairs of Dimers

5.1 Introduction

Besides a detailed study of single-swimmer properties, the interplay of two swimmers may give valuable hints on what kind of behavior is to be expected for larger systems. Such studies have been done with chemoattractive dimers by Thakur and Kapral [77], characterizing bound states originating from depletion forces. These depletion forces emerge as a simulation artifact of the MPC-MD method, due to the high compressibility of the fluid. They studied what kind of agglomerates chemoattractive (philic) dimers could form when depletion is present, and also inferred a parameter range which can be used to avoid the depletion effects. Since inducing attractive interactions in between colloids by means of depletants is experimentally feasible and a common strategy in colloidal science, the resulting depleted structures are still of interest. In the following, results on bound state formation of pairs of thermophoretic dimers are presented. These serve to make another connection between the two models as well as to see possible differences emerging. Both thermophilic and thermophobic dimers are studied.

5.2 Simulation Setup

The construction parameters determining the dimers' geometry were chosen to be as close as possible to [77]: Colloid-fluid interactions of both beads are modeled using eq. (2.7), with $(d_h/2, 0, 1, 24, r)$ for the hot bead while the phoretic bead has parameters $(4, 0, 1, 3, r)$. The dimer bond length is $s_h + s_p + \delta_b$ with $\delta_b = 0.8$. The heating temperature was chosen as $T_h = 1.3$ and the heating radius as $s_h + 0.2$. The MPC parameter α was set to 130° in these simulations and the timestep to integrate the potential to 0.002. Colloid-colloid interactions between two beads i and j are described using eq. (2.7) with $(s_i + s_j + 0.2, 0, \varepsilon_D, 6, r)$. Then, two dimers are placed inside a cubic simulation box with edge length $L = 6.25s_p$, facing each other with the front beads and a separation distance of ca. $2.5s_p$ in between them. The typical simulation runtime is 15,000. Since the available data for chemical swimmers is restricted to attractive phoretic interactions, the parameters for studying thermophobic swimmers are not chosen to closely match these. Different from the setup for thermophilic dimers no extra separation in between the two beads of one dimer is used and the heating temperature is set to $T_h = 1.5$. The colloid-fluid interaction potential of the phoretic bead is eq. (2.7), with $(d_h/2, 0, 1, 24, a)$.

5.2.1 Quantification of Bound States

Several types of persistent structures may form in these two-dimer simulations, depending on the precise choice of parameters. These structures may be more or less stable, depending on the precise choice of parameters. In order to provide quantitative descriptors to identify them, the time evolution of the internuclear separation of the phoretic beads p_1 of one and p_2 of the other dimer $r_{p_1 p_2} = |\mathbf{r}_{p_1} - \mathbf{r}_{p_2}|$ is considered. Therein, plateaus indicate formation of a bound state. Further structural information may be extracted from the angle θ_1 between the unit vectors along the connection line $p_1 p_2$ and the bond $h_1 p_1$, where h_1 refers to the center of the hot bead of dimer 1. θ_2 is considered accordingly for dimer 2. These definitions are illustrated in fig. 5.1.

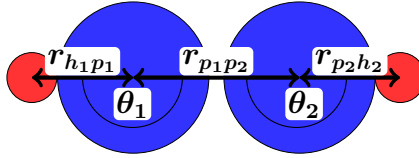


Figure 5.1: Schematic of quantitative descriptors for bound states of two dimers.

5.3 Results

5.3.1 Bound States

For any pair of dimers, when they repel each other strongly enough, no stable bound states are formed. The two swimmers then move around and collide from time to time, a situation referred to as the Independent Pair (IP) shown in fig. 5.2a for thermophilic dimers, but existing the same for thermophobic. Then, neither $r_{p_1 p_2}$ nor θ_1, θ_2 show any plateau values.

The Brownian Pair (BP) configuration is found for both thermophilic and thermophobic swimmers, it represents a state in which the dimers stick together at the rear bead, which is the hot bead for the thermophobic dimer (c.f. fig. 5.3a) and the phoretic one for the thermophilic dimer (c.f. fig. 5.2c). This leads to a configuration that shows no self-propelled motion but only performs Brownian motion as a whole. An example of the corresponding structural features is shown in fig. 5.4. In the depicted realization of the dynamics, the thermophilic dimer does not directly form the BP state, but first the Moving Pair (MP) state for some time, then switching over to BP and staying in this. The different connectivities of BP states are quantified in the angles fluctuating around $\theta_{1,2} \approx 160^\circ$ for the thermophilic dimer, which indicates that the hot beads lie, nearly linearly, on opposite sides of the formation. The thermophobic dimers instead show values of $\theta_{1,2}$ around 0° , consistent with a linear structure connected at the hot beads. This change in connectivity is due to the different directions of the phoretic effect, in the case of thermophobic dimers the

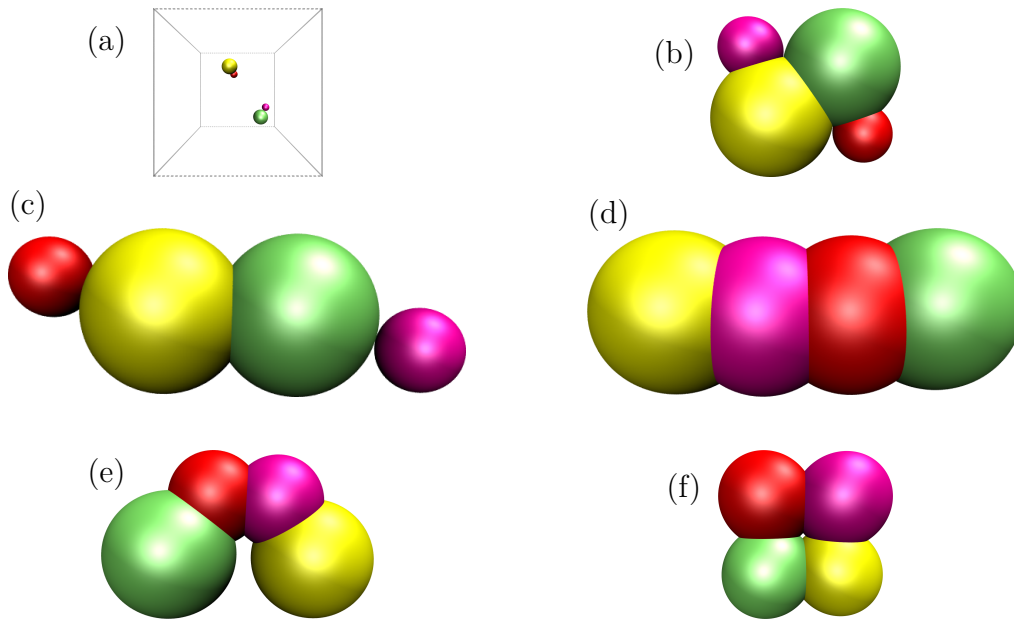


Figure 5.2: Types of bound states observed in simulations of thermophilic dimers. One dimer with red (hot) and yellow (phoretic) bead, the other with pink (hot) and green (phoretic) bead. **a)** Independent Pair (IP). **b)** Rotating Pair (RP). **c)** Brownian Pair (BP). **d)** Reverse Brownian Pair (RBP). **e)** Moving Pair (MP), pyramidal configuration. **f)** Moving Pair (MP), square configuration.

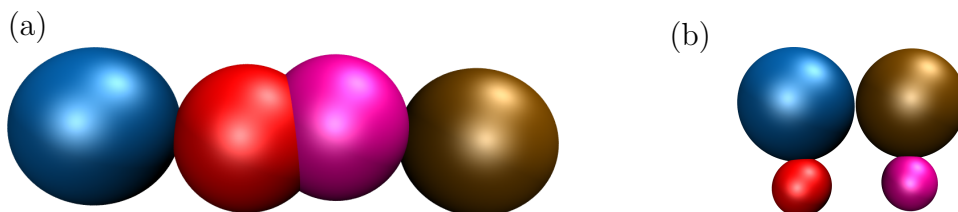


Figure 5.3: Types of bound states observed in simulations of thermophobic dimers. One dimer with red (hot) and blue (phoretic) bead, the other with pink (hot) and brown (phoretic) bead. **a)** Brownian Pair (BP). **b)** Swimming-Together Pair (ST).

phoretic beads prefer to be as far away from the heat sources as possible, while it is vice versa in the thermophilic case. The BP state is furthermore characterized by a constant distance $r_{p_1 p_2}$, which is determined by the colloid-colloid and colloid-fluid interactions, the latter indirectly through the corresponding depletion potential. As the employed colloid-fluid potentials are different for the touching hot beads in the thermophobic case and the touching phoretic beads in the thermophilic case, so is their equilibrium separation $r_{p_1 p_2}$.

With the parameters employed here, the Moving Pair (MP) is formed as an intertwined structure of thermophilic dimers and moves as a whole. Depending on the

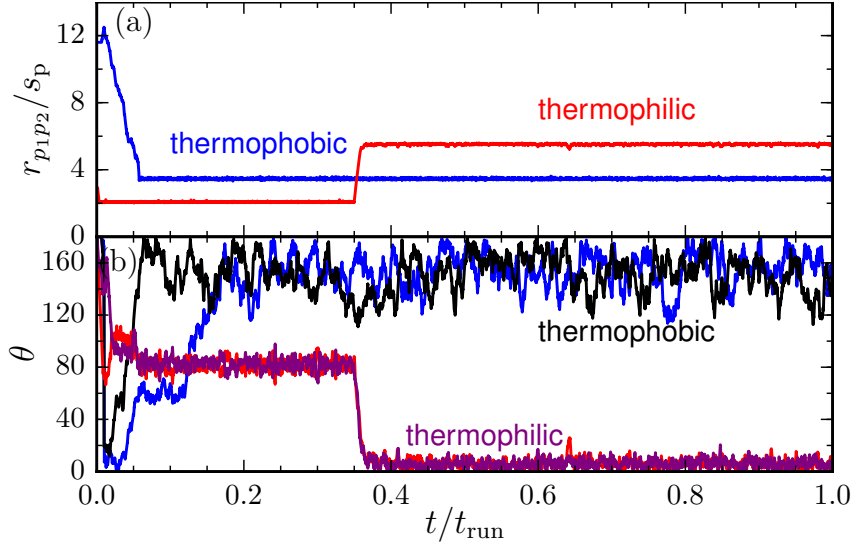


Figure 5.4: Quantification of structural features of the Brownian Pair (BP). **a)** Phoretic-phoretic bead distance normalized by the phoretic bead size s_p . **b)** Angles θ_1 (red, blue) and θ_2 (purple, black). Data is shown for thermophilic (red, purple) dimers with $s_h = s_p/2$, $\varepsilon_D = 3.5$ and thermophobic dimers (blue, black) with $s_h = s_p$, $\varepsilon_D = 1$. Simulation time t is normalized by the overall runtime t_{run} .

size ratio of the beads, square (c.f. fig. 5.2f) formations result for symmetric constructions and more pyramidal-like formations for asymmetric constructions (c.f. fig. 5.2e). These states are characterized by a constant distance $r_{p_1 p_2}$ and angles fluctuating around an average value of $\theta_{1,2} \approx 90^\circ$ for the pyramidal example shown in fig. 5.5. The MP formed and dissolved twice in the example shown. The configuration of thermophobic dimers that moves as a whole is the Swimming-Together Pair (ST) shown in fig. 5.3b, which in contrast to the MP of thermophilic dimers is not intertwined. The example in fig. 5.5 shows a simulation in which this state formed quickly and remained stable for the whole simulation time. The ST state is characterized, besides a distance $r_{p_1 p_2}$ slightly below $2s_p$, by angles $\theta_{1,2} \approx 40^\circ$ for $s_h = \frac{3}{4}s_p$ as shown in the example, indicating a pyramidal structure. For $s_h = \frac{1}{2}s_p$, whose configuration is shown in fig. 5.3b, the distance is the same but the angle is $\approx 90^\circ$, indicating parallel alignment of the two dimers in the formation.

Thermophilic dimers form two additional states, the Rotating Pair (RP) (c.f. fig. 5.2b) and, for very low inter-dimer repulsion strength, the completely intertwined Reverse Brownian Pair (RBP) (c.f. fig. 5.2d). Their characteristics are shown in fig. 5.6. The RP forms, for the construction shown, with constant distance $r_{p_1 p_2} \approx 2$, indicating touching phoretic beads, and constant angles $\theta_{1,2} \approx 45^\circ$. It shows no net propulsion, but rotates constantly. The rotational motion can be observed in the depiction of the components of the vector $\mathbf{r}_{p_1} - \mathbf{r}_{\text{cm}}$ between one phoretic bead and the center of mass of the whole formation, following a sinusoidal-like course. The RBP shows neither net propulsion nor rotation, it represents a

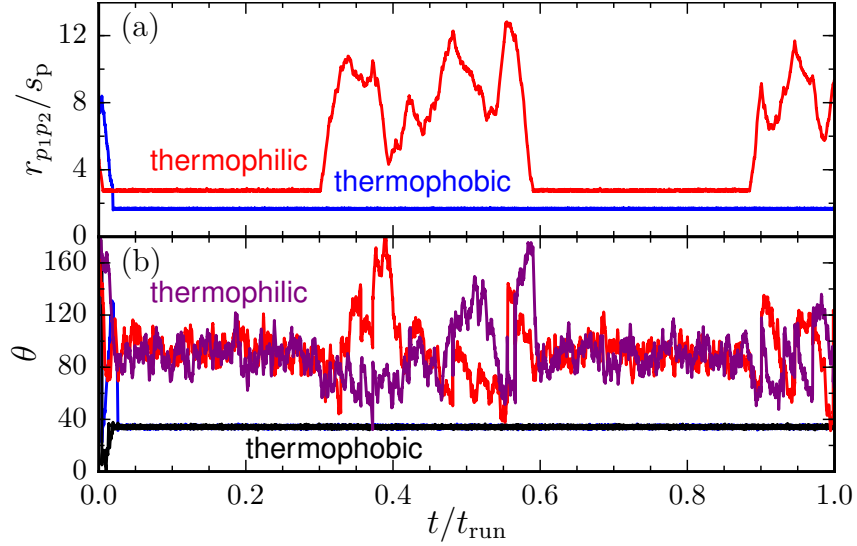


Figure 5.5: Quantification of structural features of the Moving Pair (MP) and the Swimming-Together Pair (ST) bound states. **a)** Phoretic-phoretic bead distance normalized by the phoretic bead size s_p . **b)** Angles θ_1 (red, blue) and θ_2 (purple, black). Data is shown for a thermophilic (red, purple) dimer with $s_h = 3/4s_p$, $\varepsilon_D = 0.1$ and a thermophobic dimer (blue, black) with $s_h = 3/4s_p$, $\varepsilon_D = 2.5$. Simulation time t is normalized by the overall runtime t_{run} .

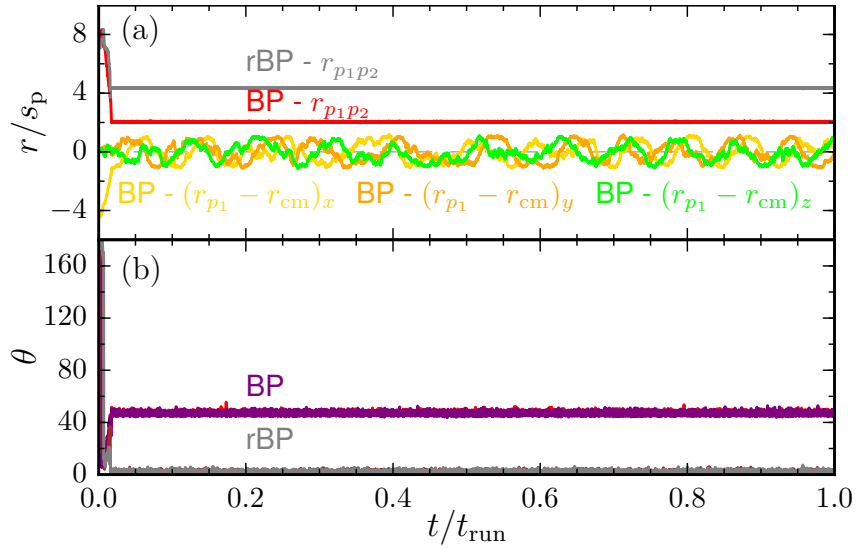
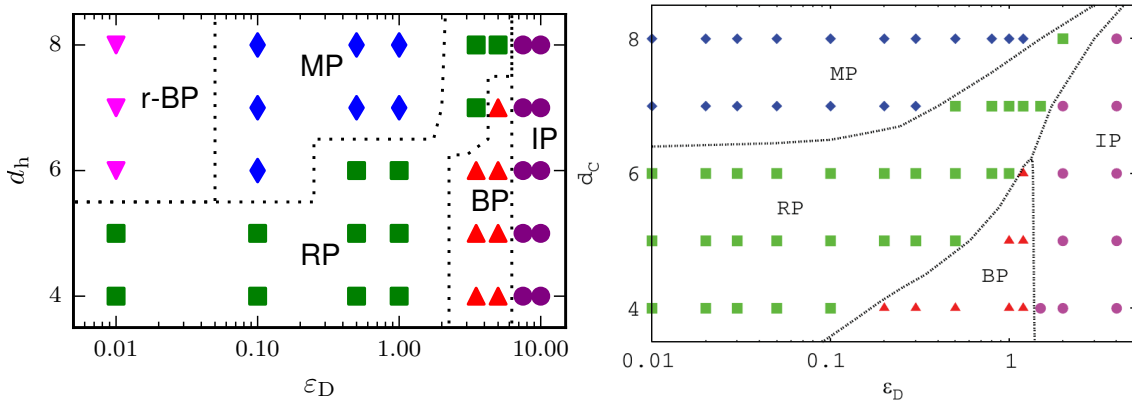


Figure 5.6: Quantification of structural features of the Rotating Pair (RP) and the Reverse Brownian Pair (RBP) bound states of thermophilic dimers. **a)** Phoretic-phoretic bead distance normalized by the phoretic bead size s_p (red, gray). For the RP, the x - (yellow), y - (orange) and z - (green) components of the distance vector $\mathbf{r}_{p_1} - \mathbf{r}_{\text{cm}}$ are also shown. **b)** Angles θ_1 (red, blue) and θ_2 (purple, black). Data is shown for a RP (red, purple, green, yellow, orange) state with $s_h = s_p/2$, $\varepsilon_D = 0.1$ and a RBP state (gray, brown) with $s_h = s_p$, $\varepsilon_D = 0.01$. Simulation time t is normalized by the overall runtime t_{run} .

formation in which, due to the low repulsion in between dimers, the hot bead of one dimer comes in between the two beads of the other. The resulting agglomerate stays stable in a linear configuration, as indicated by $\theta_{1,2} \approx 0$.

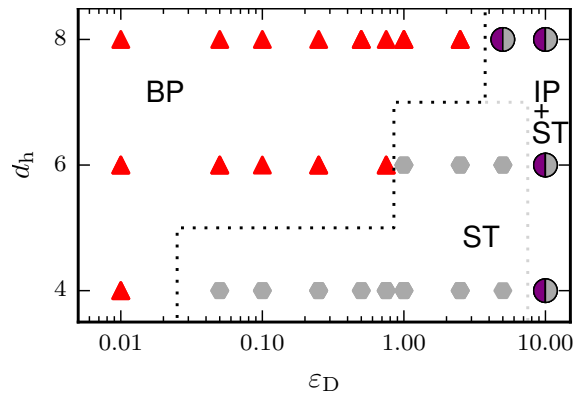
5.3.2 Phase Diagram

A phase diagram of bound states may be constructed taking into consideration variation of the relative size of the constituent beads, here for a fixed phoretic bead in terms of the hot bead's size $s_h = d_h/2$, and the inter-dimer repulsion strength ε_D . Phase diagrams for thermophilic, chemoattractive and thermophobic dimers are shown in fig. 5.7. The assignment to one specific bound state in the depicted



(a) Thermophilic Dimers.

(b) Chemoattractive dimers, from [77].



(c) Thermophobic dimers.

Figure 5.7: Phase diagrams for bound state formation obtained from simulations of pairs of dimers. Abbreviations of bound states are those of fig. 5.3 and fig. 5.2. Notation is chosen to facilitate comparison to chemoattractive swimmers with catalytic bead c and $d_{h/c} = 2s_{h/c}$. $d_{h/c} = 8$ corresponds to symmetric dimers, lower values feature smaller hot beads.

phase diagrams is not unique, in fact in different realizations of the same system

different states might form and also convert into each other. Therefore, it is based on a majority decision, i.e. it represents what happens in most of the realizations. Consider first the diagrams fig. 5.7a and fig. 5.7b for thermophilic and chemoattractive dimers. These are in fact quite similar, the same bound states are observed for the thermal dimers and the qualitative form is also kept with slight shifts of the boundary lines. The only notable exception is that an additional bound state is observed for very low inter-dimer repulsion and size ratios $d_h/d_p = 1$ and $3/4$. This is the RBP (c.f. fig. 5.2d), which represents a highly intertwined configuration, with the bonds of each dimer passing directly through a bead of the other. It is to be expected that a similar state would also be observed for chemical dimers upon further lowering of ε_D , such that the phase boundary would exist but is just not found in the parameter range depicted. Though an exact match of parameters is not possible, the resulting behavior of pairs of thermophilic and chemoattractive dimers is determined by the same effects, the combination of propulsion, phoretic attraction and purely attractive depletion interactions. The observed similarities are to be expected, and emerge even though the depletion forces will not be the same for chemical and thermal dimers due to the different potentials employed. This most of all indicates that the dynamics of two dimers do not greatly depend on the phoretic mechanism they are driven by.

While there is not much difference observed in between pairs of chemoattractive and thermophilic dimers, the dynamics do strongly depend on the direction of the phoretic effect. Figure 5.7c shows the resulting phase diagram for thermophobic dimers, which, except for the independent pairs occurring at high inter-dimer repulsion, bares no resemblance to that of thermophilic or chemoattractive dimers. No MP and RP states are observed here, nor any RBP. Instead, the BP takes up a large area at high d_h and low to intermediate repulsions ε_D , while it was in the region of lower d_h and higher ε_D for thermophilic swimmers. Additionally, a new bound state occurs, the ST state, in which the dimers propel together in an aligned fashion, connected at the phoretic bead, as shown in fig. 5.3b. It bares some resemblance to the MP (see figs. 5.2e and 5.2f), which also propels as one entity. But due to the opposite sign of the phoretic effect, the phoretic beads keep as far away as possible from the hot beads of the other dimer, whereas they are attracted to them in the thermophilic case, which also presents an intertwined configuration. The depletion forces are stronger for thermophobic dimers than for thermophilic, due to the steep attractive colloid-fluid interaction employed to model the phoretic bead (c.f. figs. 6.4 and 6.5), such that even for high repulsions ε_D the ST state can still be observed for very short times. To indicate that for higher ε_D the probability of formation, as well as the persistence, of ST states is significantly reduced, a phase boundary is drawn in lighter color and both IP and ST are shown in the right side of fig. 5.7c.

There are two main differences in between the ST and BP of thermophobic dimers. For one, it is the angle between the beads hot-phoretic-phoretic, being around 90° for the ST with $s_h = s_p/2$ and around 180° for the BP. Then, it is which beads of the two dimers are connected, i.e. persistently at close contact through

the depletion interaction. For the BP, it is the two hot beads that are touching, while for the ST it is the phoretic beads. Considering only the phoretic repulsion, the BP state will be optimal, what makes understandable that for the dimer with the largest considered hot bead ($d_h = 8$), and thereby strongest phoretic effect, no persistent ST states are observed. There will be a balance of two effects when the phoretic beads are connected in the ST that are responsible for it keeping its structure. For one, the two phoretic beads are repelled by the temperature field around the hot beads, which will favor the hot beads being outwards. That the structure moves in a fluid however favors the hot beads being behind the phoretic beads at front, in order to minimize friction. Balancing these two effects, the ST structure forms with the hot beads sticking out as little as possible to the sides, while being away as far as possible from the phoretic beads.

5.4 Summary and Conclusions

By means of MPC-MD simulations, it is shown that phoretic dimers driven by thermophoresis may form stable structures through (artificial) depletion forces. The similarities in structures formed by pairs of thermophilic and chemoattractive dimers suggest that the type of phoretic driving mechanism does not influence the kind of bound state formation to a relevant degree, consistent with what was observed in chapter 4 for the single swimmer dynamics. For the single swimmer case, as shown in fig. 4.4a, a different phoretic effect leads to mostly quantitative differences in swimming behavior, while the overall qualitative behavior is the same for the thermal and chemical driving mechanism.

Concerning thermophobic dimers, reversion of the phoretic effect with respect to thermophilic or chemoattractive dimers leads to very different structures, among them the ST state showing stable, aligned propulsion. This bound state is of specific interest, presenting the only observed formation that propels without having the dimers intertwined, as in the case of the MP. Though its geometry is consistent with what one would expect from the lateral attraction observed in the single swimmer flow fields of asymmetric dimers (specifically, fig. 4.5e), the attraction keeping the dimers together does not originate in hydrodynamics but in depletion. As depletion may be induced as well by adding depletants in experimental systems, the construction of such a state is likely possible.

The phase diagrams obtained can be used to choose parameters for simulations of more swimmers [79]. In this case, one is interested in choosing a region in which no bound states form due to depletion, such that any build-up of structures in larger ensembles can be attributed to collective effects and not artificial depletion. Doing so amounts to counteracting the depletion interaction by a stronger repulsion potential. Thermophobic dimers however feature very strong depletion forces in the parameter range considered, and therefore do not show any region in the phase diagram in which pair formation stops. To enable simulations of larger ensembles of thermophobic dimers, additional care will therefore need to be taken to avoid

spurious depletion forces. The next chapter will examine depletion in MPC-MD in detail, in order to enable a suitable choice of interaction parameters when studying collective systems, especially of thermophobic dimers.

6 Depletion Interactions

6.1 Introduction

Depletion is an effective force that emerges in colloidal systems of at least two constituents of different, but still comparable, size [89, 90]. Adding depletants, like short polymers for example, to a solution is a common procedure to induce attractive depletion interactions between larger suspended particles [91, 92]. An illustrating example is shown in fig. 6.1, depicting an experimentally observed transition from a fluid to a solid clustered state of polystyrene beads upon addition of smaller particles. Depletion forces also arise in MPC-MD simulations, but are there

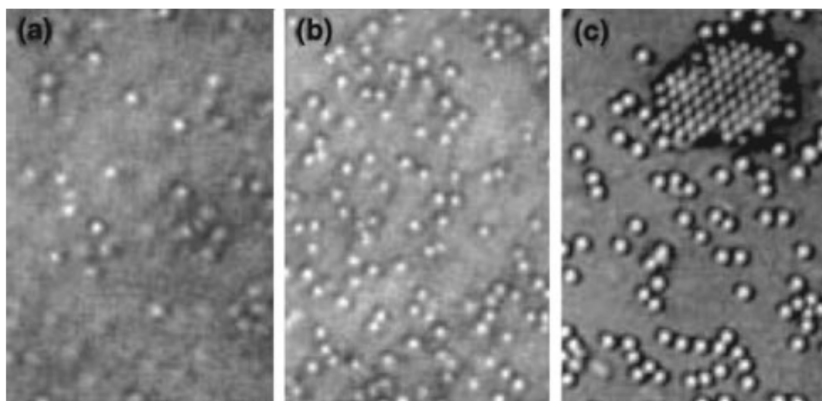


Figure 6.1: Micrographs of polystyrene spheres (radius $0.8 \mu\text{m}$, volume fraction $\phi = 0.02$) at a glass wall with **(a)** no small spheres, and added small spheres (radius 70 nm) with $\phi_{\text{small}} = 0.08$ **(b)** and $\phi_{\text{small}} = 0.16$ **(c)**. Taken from [89], therein from [93].

considered a simulation artifact, since one is with this method aiming at describing an atomic/molecular fluid. There, no such forces should arise for large colloids in the absence of explicit depletants.

6.2 Theory for Penetrable Hard Spheres

In order to present the main concepts of depletion interaction, a general discussion following [89] is given in the following. Consider two large spherical colloids of radius R immersed somewhere in a bath of smaller, also spherical, colloids of diameter σ .

All colloids are viewed as hard spheres that repel each other upon collision, i.e. the interaction potential U_{LS} between large (L) and small (S) spheres is given by

$$U_{LS}(r) = \begin{cases} \infty, & r < R + \sigma/2 \\ 0, & r \geq R + \sigma/2 \end{cases} \quad (6.1)$$

with r being the pairwise center-to-center distance. In equilibrium, on average no force will act on any large colloid due to the symmetry of the LS-interactions. This however changes when the two large colloids approach each other and their so-called depletion layers start to overlap. The depletion layer for a large hard sphere is given by the radius $\sigma/2$ of the small hard spheres. As long as the centers of two big spheres are separated by more than $2R + \sigma$, there is always room for small spheres in between them. Once below that distance, small spheres cannot enter the region in between the two large spheres, called the depletion zone. This induces an attractive force between the two large spheres. From the viewpoint of the large colloids, the osmotic pressure is no longer balanced, because there are more small spheres on one side than on the other. From the viewpoint of the small spheres, the accessible free volume increases due to the overlap of the two large spheres.

The seminal theoretical model for depletion forces is the Asakura-Oosawa (AO) model [94], which is a model for penetrable hard spheres. Therein, hard sphere interactions are only considered in between the large and the small spheres while the small spheres can freely overlap. A sketch of this setup is shown in fig. 6.2. The scenario leads to an effective interaction potential in between the large spheres

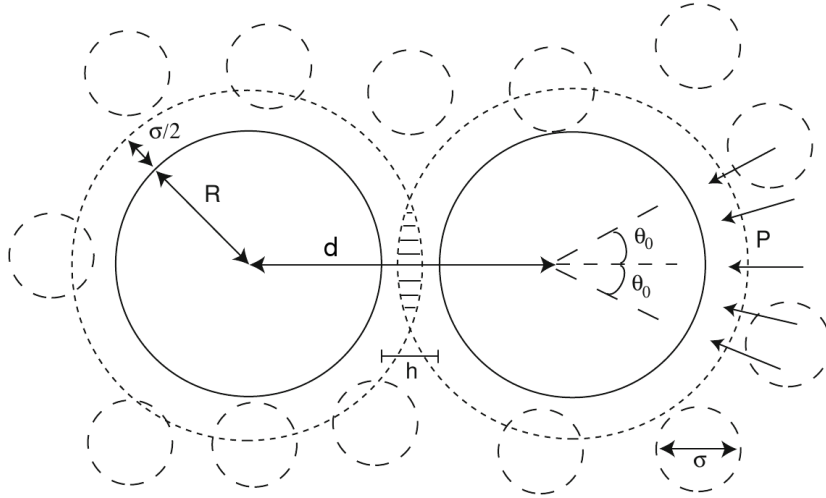


Figure 6.2: Sketch of two large spheres with radius R immersed in a bath of penetrable small spheres with diameter σ . The depletion layer of length $\sigma/2$ is shown by dashed lines. The width of overlap is given by h , and the overlap volume marked as hatched. P denotes here the unbalanced osmotic pressure that leads to depletion forces. Taken from [89].

given by

$$U_{LL}^{(\text{AO})}(d) = -n_S k_B T V_{\text{ov}}(d), \quad (6.2)$$

where n_S refers to the number density of small spheres and the overlap volume $V_{\text{ov}}(d)$ is given by the difference in volume available to the small spheres for the two large spheres at infinite separation $d = \infty$ and for some separation distance d at which the depletion layers overlap, so

$$V_{\text{ov}}(d) = V_{\text{excl}}(\infty) - V_{\text{excl}}(d). \quad (6.3)$$

For hard spheres, this model can be solved analytically, leading to

$$V_{\text{ov}}(d) = \frac{4\pi}{3} (R + \sigma/2)^3 \left[1 - \frac{3}{4} \frac{d}{(R + \sigma/2)} + \frac{1}{16} \left(\frac{d}{(R + \sigma/2)} \right)^3 \right]. \quad (6.4)$$

For a derivation of these results see [89].

6.3 Application to MPC-MD

In MPC-MD, the fluid consists of point-like particles that do not interact with each other except for coarse-grained, elastic collisions. The MPC fluid itself has an ideal-gas equation of state and colloids interact with the fluid particles through soft potentials. For a hard-sphere bounce-back interaction model in between colloids and fluid, no depletion could occur as long as the colloids do not overlap, since the MPC particles would then have only point-like properties. But the soft interactions, along with the high compressibility of the fluid, lead to the method being prone to artificial depletion effects, as pointed out by Padding and Louis [54]. The soft pairwise interactions effectively assign a size comparable to that of colloids to the fluid particles.

The combination of a MPC fluid and colloids that interact through soft potentials with it refers, in terms of depletion models, to a model of penetrable *soft* spheres. The density distribution ρ of MPC particles i around a central potential u_{ij} of a particle j is

$$\rho_i(r) = \bar{\rho} \exp(-\beta u_{ij}(r)) \quad (6.5)$$

where r denotes the radial distance in between i and j and $\bar{\rho}$ is the equilibrium density. For penetrable soft spheres the potential of mean force for the depletion interaction can be written as [54]

$$U_{LL}(d) = \bar{\rho} k_B T [V_{\text{excl}}(d) - V_{\text{excl}}(\infty)], \quad (6.6)$$

with the excluded volume now given by, considering one large sphere at \mathbf{r}_1 and the

other at \mathbf{r}_2 ,

$$V_{\text{excl}}(d) = \int d^3\mathbf{r} f_{\text{LS}}(\mathbf{r} - \mathbf{r}_1) f_{\text{LS}}(\mathbf{r} - \mathbf{r}_2), \quad (6.7)$$

where f_{ij} the Mayer function associated with the colloid-fluid interaction [95]

$$f_{ij} = 1 - \exp(-\beta u_{ij}). \quad (6.8)$$

Multiplying out the full expressions for f_{LS} , one arrives at contributions for the volume of sphere 1, sphere 2, and the overlap volume. Since the single sphere volumes are independent of the separation d , it is sufficient to integrate over

$$V_{\text{excl}}(d) = \int d^3\mathbf{r} \{1 - \exp[-\beta u_{\text{LS}}(\mathbf{r} - \mathbf{r}_1) - \beta u_{\text{LS}}(\mathbf{r} - \mathbf{r}_2)]\} \quad (6.9)$$

as the single sphere volumes cancel out in eq. (6.6) anyways. This formula is more suitable for numeric integration and was also used in this form in [54].

This theory should in principle exactly predict simulation measurements of depletion with no need for any adjustable parameters due to the ideal gas equation of state of the MPC fluid. This was already (implicitly) assumed in [54].

6.3.1 Comparison to Simulations

The validity of eq. (6.6) for a colloidal suspension simulated with MPC-MD can be checked by the usual way of setting up depletion simulations, see for example [90], such that the MPC fluid is treated as a depletant. In this procedure, two large spheres are placed at fixed separation d in a bath of smaller spheres, or, in this case, MPC particles. Then, for varying separations d , the forces on the two spheres are measured. Integration of the so-obtained forces as a function of d yields the interaction potential.

The setup described above was used to measure depletion forces for a variety of parameters in order to verify agreement of simulation results with the outlined theory for penetrable soft spheres. For this discussion, consider the generalized Lennard-Jones (LJ) potential as given by eq. (2.7).

A first important consideration is to see whether the character of the MPC solvent plays any relevant role. All properties that distinguish MPC from a pure ideal gas are due to the performed multi-particle collisions. The strength of their influence is given by the rotation angle α , where $\alpha = 0$ means that no collisions are performed and the fluid is a pure ideal gas with no correlations in between constituent particles. Simulations are performed for different rotation angles α and compared to the case where a pure ideal gas is simulated. Results for utilizing repulsive colloid-fluid interactions are shown in fig. 6.3a. They show that there is no effect on the obtained depletion forces, independent of whether the MPC algorithm is used or the fluid is just described as a pure ideal gas. Agreement to the theoretical predictions is close to perfect, except for some minor fluctuations due to the statistical accuracy of the

simulations. Such agreement was to be expected from the equation of state, but to the best of my knowledge not yet explicitly confirmed [54, 77, 96]. For completeness, and to also see in how far the numeric integration of eq. (6.6) is stable, other parameters were also checked, especially those concerning the potential interaction. Depletion forces for varying σ , ε and ρ are presented in figs. 6.3b to 6.3d. Depictions here are mostly restricted to showing the depletion forces, since one is for MPC-MD mostly interested in avoiding depletion and obtaining a full depletion interaction potential is computationally costly. In all cases, the agreement with theory is near

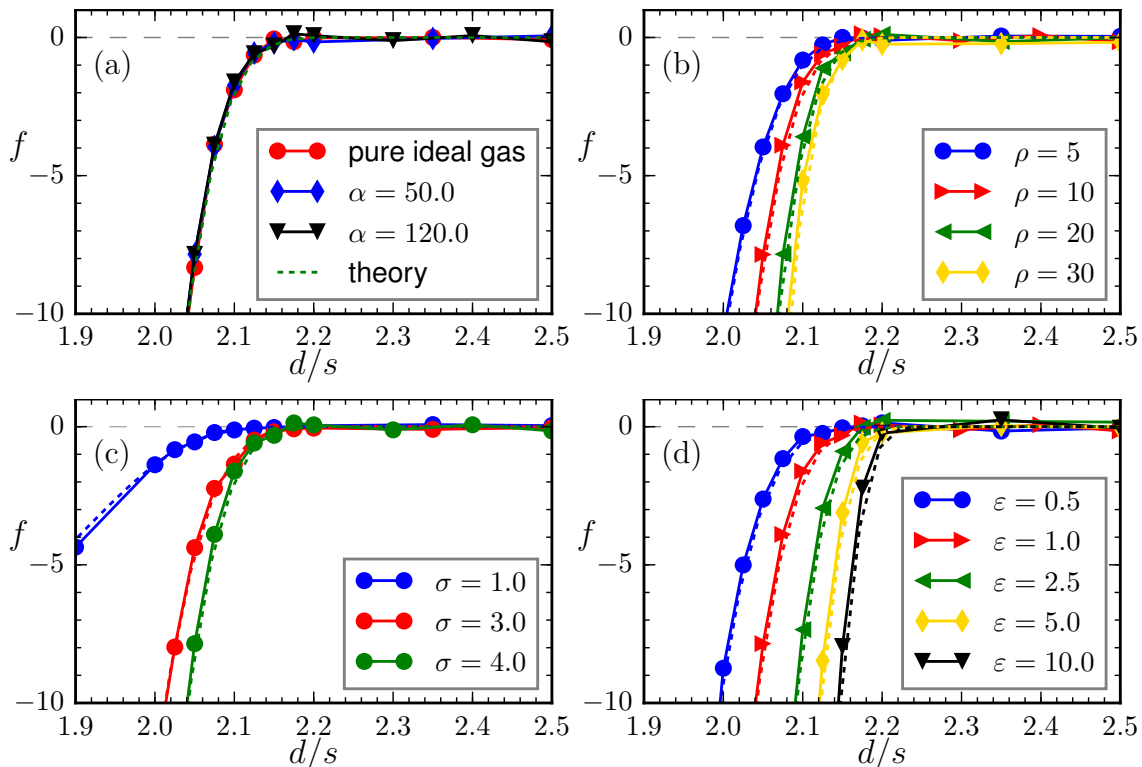


Figure 6.3: Depletion induced forces on two fixed spheres of radius s as a function of their separation d and their dependencies on the MPC fluid parameters α (a) and ρ (b) as well as on the interaction parameters σ (c) and ε (d). The colloid-fluid interaction potential employed corresponds to eq. (2.7) with $(s, \Delta, \varepsilon, n, r) = (4, 0, 1, 6, r)$ such that $\sigma = s - \Delta$. Dashed lines correspond to theoretical predictions based on eq. (6.6). Curves in figs. 6.3b and 6.3c can also be normalized by the varied parameter.

to perfect. Note that it is also possible to normalize the depicted curves for σ and ρ such that they fall together, though this is not done here to give a better impression on how the parameter of interest changes the depletion forces.

6.4 Colloid-Colloid Interaction Tuning to Avoid Depletion

The characterization of depletion forces is of great help to design strategies to avoid artificial depletion. Depletion interactions solely depend on the form of the colloid-fluid interaction potential and are, according to the considerations above, exactly as long ranged as this potential. The depletion layer for any colloid-fluid interaction is thereby given by the cutoff of the colloid-fluid interaction. Therefore, introduction of an extra separation δ into the colloid-colloid interaction will reduce depletion. The interaction range for two colloids i, j is then given by $s_{cc} = s_{cf,1} + s_{cf,2} + \delta$. Using a short extra-separation δ , as also discussed in [54], is beneficial anyhow to resolve lubrication forces with the MPC algorithm. For $s_{cc} > 2r_{cut,cf}$, the depletion layers can in principle no longer overlap. However, due to the soft nature of the interactions, colloids may overlap farther than s_{cc} and then again suffer depletion forces. Padding and Louis used undisplaced repulsive colloid-colloid interaction potentials with ranges larger than two times the colloid-fluid interaction range, $s_{cc} > 2s_{cf}$ [54]. Although their parameter choice was close to $s_{cc} > 2r_{cut,cf}$ they still saw some remaining depletion artifacts, which is most likely due to the soft nature of colloid-colloid interactions. Even though they in principle advised against it, they then decided to use an additional counter-potential $U_{counter} = -U_{depletion}$ based on eq. (6.6) to counteract depletion, which worked well for the equilibrium properties they were interested in. There are several problems inherent in using a counter-potential [54]. For one, it is a pair-wise interaction and therefore will not account for higher-order contributions. Then, it will be instantaneously applied while depletion requires some time to build up, thereby overcompensating. Lastly, it will also not account for possible anisotropies in the density distribution induced by some external field.

Whitmer and Luijten followed in their work the discussion of Padding and Louis, choosing s_{cc} larger than $2s_{cf}$ to avoid artificial depletion [96]. Thakur and Kapral discussed depletion forces as well in their studies on colloidal swimmers [77, 79]. They also chose a certain inter-separation distance δ and proceeded then to tune the colloid-colloid repulsion strength ε . For low values of ε depletion-induced bound states of the swimmers formed. When the repulsion strength ε reached high enough values, no such states could be observed anymore, from which it was concluded that artificial depletion is avoided and the corresponding parameters were then used for further simulations [79, 97].

Summarizing, the ingredients to avoid artificial depletion forces that have been used so far are:

- Introduce a colloid-colloid extra separation δ , such that $s_{cc} = 2s_{cf} + \delta$. δ should be large enough to avoid overlap of the depletion layers.
- Tune the parameters ε and/or n of the chosen colloid-colloid interaction potential to avoid colloids overlapping into each others depletion layer due to

thermal fluctuations.

- Counteract depletion that is still present for distances smaller than the chosen s_{cc} with a compensating potential.

Except for using counter-potentials, which is inherently problematic, these approaches all require that depletion is short-ranged. Otherwise, the effective colloid-colloid interaction range might become too large as compared to other relevant length scales. This requirement is fulfilled for the colloid-fluid interaction potentials that are discussed in the literature, which are mostly undisplaced WCA potentials with exponent $n = 6$. For this choice, depletion is only relevant up to colloid-colloid separations of roughly $2.2s$, which can be inferred from the measurements shown in fig. 6.3. However, using colloid-fluid interaction potentials with short-ranged depletion layers presents a restriction on the possible form of these potentials, and thereby also on the physical effects that can be reproduced by them. When potentials with longer ranges are needed, like attractive colloid-fluid interactions of the Lennard-Jones type necessary in this work to reproduce thermophobic colloidal behavior, this will inherently also lead to longer depletion ranges. Furthermore, the depletion forces induced by using steep attractive potentials are stronger than those induced by soft repulsive interactions. Additionally, they have a more complex form and are typically attractive for longer separations, then start to be repulsive close to $r = 2s$ and get attractive again for high overlaps. Purely repulsive colloid-fluid interactions induce purely attractive depletion forces. Two representative cases are shown in fig. 6.4 to give an impression on the functional form of depletion potentials and forces stemming from of attractive and purely repulsive colloid-fluid interactions.

Stronger depletion forces can be counteracted by accordingly tuning the colloid-colloid repulsion to avoid even small overlaps. A longer range might be more problematic, as it may interfere with the aforementioned relevant length scales. A relevant example in the context of this work is the interaction between thermophobic dimeric swimmers. For a symmetric construction, this swimmer shows short-ranged hydrodynamic attraction, which is considerably reduced when using a colloid-colloid extra separation appropriate to avoid depletion, as is the phoretic effect that is strongest at close contact. This will be shown for a relevant construction in the next chapter, by the gray lines in fig. 7.3.

Through introduction of displacements Δ_{cf} in the potential interactions given by eq. (2.7), the issue of long depletion layers can be reduced. Since depletion is only dependent on the colloid-fluid potential, displacing it while keeping the colloid-fluid interaction range σ_{cf} fixed will make it possible for colloids to approach each other more closely with respect to their so-enlarged diameters. This would in principle solve the problem, but enlarging colloids is computationally very costly. Therefore, one can try to introduce the shift Δ_{cf} while keeping the colloid radius $s = \sigma_{cf} + \Delta_{cf}$ constant. This will not change the functional form of the interaction, but may reduce any effects related to the range of the colloid-fluid interaction. In the context of this work, the most relevant property scaling with the range and strength of the

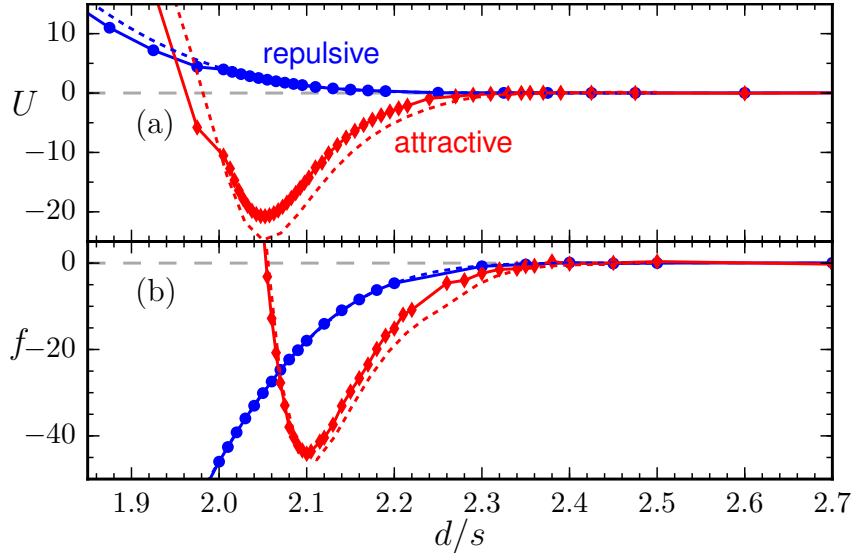


Figure 6.4: Measured (solid) and predicted (dashed) depletion potential U (a) and forces f (b) in between two colloids for a soft repulsive (blue) colloid-fluid interaction potential according to eq. (2.7) with $(4, 0, 1, 3, r)$ and a steep attractive (red) one with $(4, 0, 1, 24, a)$.

colloid-fluid interaction is the phoretic effect, and it has to be taken care that this will not be diminished, but only reduced by an acceptable amount. This effect will be discussed for a reference construction in the next chapter.

The effect the introduction of displacements has on depletion forces is shown in fig. 6.5. It can there be seen that, for the chosen attractive potential in fig. 6.5a, a value of $\Delta = 0.5s$ reduces the depletion range from around to $0.5s$ to a more suitable value of $0.2s$. Since the phoretic driving force is not significantly reduced by this displacement, its choice presents a good compromise between the need to avoid depletion and being computationally efficient. For the repulsive interaction shown in fig. 6.5b, depletion is shorter-ranged and also much weaker as compared to the attractive interaction. Still, to be sure that no residual depletion may effect the simulations, the choice of a displacement $\Delta_{cf} = 0.5s$ can also be considered here.

Due to the soft nature of the interactions, there may always be residual effects of depletion, even though displaced potentials are used. In consequence, a test should be performed to make sure that the properties of interest are not afflicted by depletion. The precise choice of test case depends on the problem one wishes to study. For example, Thakur and Kapral [77] checked the formation of bound states of colloidal swimmers to choose a parameter range that did not show their formation anymore. Padding and Louis [54] measured the equilibrium radial distribution function and compared it to results of Brownian Dynamics simulations. In the collective systems under investigation in this work, there is strong clustering observed when depletion forces are involved. As any clustering in thermophoretic systems should be due to the effect of thermal gradients and the resulting popul-

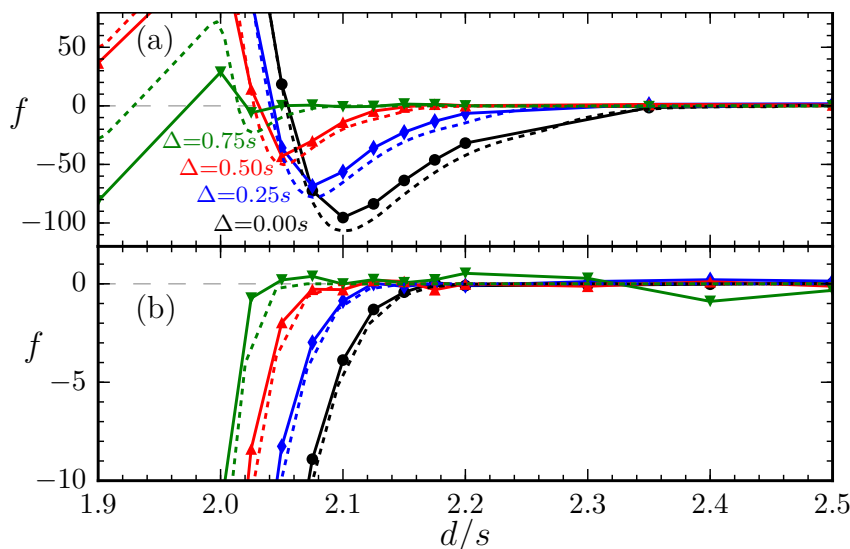


Figure 6.5: Depletion forces obtained by employing displacements in the colloid-fluid interaction potentials of eq. (2.7). **a)** Step attractive interaction with $(6, \Delta, 1, 24, a)$. **b)** Standard WCA repulsive interaction with $(6, \Delta, 1, 6, r)$. Displacements used are $\Delta = \{0 \text{ (black)}, 0.25s \text{ (blue)}, 0.5s \text{ (red)}, 0.75s \text{ (green)}\}$ in both **a)** and **b)**.

sion induced by them, these clusters should dissolve upon switching off the heat sources. When depletion forces are responsible for clustering, cluster dissolution barely happens. This phenomenology was used as a check here, showing that upon choosing suitable parameters, cluster dissolution due to Brownian motion readily takes place when the heat sources are switched off. It also confirms the assumption that one can use the simple depletion measurements of two spheres without any temperature gradients involved to choose reasonable parameters for more complex situations.

Avoiding Depletion The necessary steps to obtain a parameter region where artificial depletion is negligible are here summarized.

- Calculate or measure the depletion forces for two spheres, interacting with the fluid through the desired potential.
- If the range in which the depletion forces go to zero is too long for the physical effects under consideration, introduce a displacement into the colloid-fluid interaction and calculate/measure again.
- Tune the colloid-colloid interaction to avoid the depletion region by adjusting the range s_{cc} and the strength ε accordingly.
- Identify and perform a suitable test to check whether it worked in the system of interest.

6.4.1 Combination with Bounce-Back

That one needs to adapt the colloid-colloid interaction to avoid depletion might be disadvantageous, depending on the physical system under consideration. For the colloids investigated in this work, a strongly repulsive interaction representing pure excluded-volume interactions is used. In this case, the interaction is inherently suitable to avoid depletion. However, there might be cases where it is desirable to use a different interaction, for example to include electrostatic attraction. Then, it can be more problematic to model the desired physical behavior and avoid depletion artifacts at the same time. It might be possible to use a combination of a hard-sphere bounce-back rule that hinders colloids from overlapping each others depletion layer in combination with an arbitrary potential. One could then choose the colloid-colloid interaction freely but for the minimum distance determined by the depletion layers. A problem with this approach can be that a bounce-back rule affects the positions of colloidal particles, introducing discontinuities in the forces when soft potentials are also present. Whether this is a negligible disturbance of the dynamics will depend on several factors, foremost the colloids' velocities, as these determine the amount of possible penetration when the bounce-back kicks in. For any system, the applicability of such a method should always be checked with a suitable test case.

6.5 Summary and Conclusion

The emergence of artificial depletion forces in MPC-MD simulations is reexamined in the context of colloidal systems. These depletion forces can be obtained using standard methodology, by varying the distance in between two fixed colloids and measuring the force the surrounding fluid exerts on them. The numeric calculation of depletion forces agrees perfectly to these measurements. This is to be expected from the equation of state of MPC-MD and confirmed by the simulations performed. Since the precise choice of colloid-fluid interaction parameters matter, as exemplified in the inclusion or diminishing of short-range hydrodynamic effects, a careful consideration of depletion interactions is necessary and a framework to do so provided. Specifically, introduction of displacements into the colloid-fluid interactions is presented as a means to enable closer contact of colloids without suffering artificial depletion forces. Although the occurrence of artificial depletion makes it necessary to always use extra separations, a careful tuning of interaction parameters enables these to be small enough to take into account all relevant colloidal interactions like hydrodynamics, phoresis, and others.

7 Collective Swimmer Dynamics

7.1 Introduction

Active systems of both artificial and biological microswimmers show a variety of collective behaviors. Vortices, Motility-Induced Phase Separation (MIPS), and swarming were already introduced in chapter 1. The following will provide an overview over other known collective behaviors, before discussing the phenomenologies observed in simulations of many dimer swimmers.

Clustering and Living Crystals of Self-Propelled Spheres Many active systems show density-dependent clustering and living crystals. [20] Qualitatively speaking, when two or more self-propelled spheres collide head-on, they block each other. It takes some time for the spheres' propulsion directions to reorient and thereby to dissolve this transient structure. If during this reorientation time other particles collide with the aggregates, larger clusters may form and the system may phase-separate into a gas-like phase of propelling particles and a dynamic crystalline phase of particles whose propulsion is hindered. This phenomenology can be described with the concept of MIPS [98] and does not require any alignment mechanism [9]. It has been shown by several authors that hydrodynamics may influence this phase behavior [82, 99]. MIPS can take place in both two- and three-dimensional systems. In two dimensions, crystalline and gas-like phases form, while in three dimensions liquid-like and gas-like phases coexist [8]. Simulation and experimental examples of spherical microswimmers in two dimensions with a gas-solid phase separation were shown in chapter 1 (figs. 1.2c and 1.2f), as well as a simulation example of gas-liquid phase separation in three dimensions (fig. 1.2b). A simple experimental model system of active spherical particles that shows MIPS is that of Buttinoni et al. [10] based on light-activated Janus particles with negligible phoretic and electrostatic interactions. When additional inter-particle interactions are present, the phase behavior may change further. Theurkauff et al. [100] report experimental observation of a dynamic kind of clustering even at very low densities, where smaller clusters form, dissolve and constantly exchange particles, referred to as living crystals. This behavior has been attributed to chemotactic interactions among the spherical colloidal particles confined to a two-dimensional plane. Smaller agglomerates of these Janus-type particles show a non-vanishing net propulsion, slower than the single-particle velocities, likely since the propulsion velocities of the constituent particles do not cancel completely within a single small cluster.

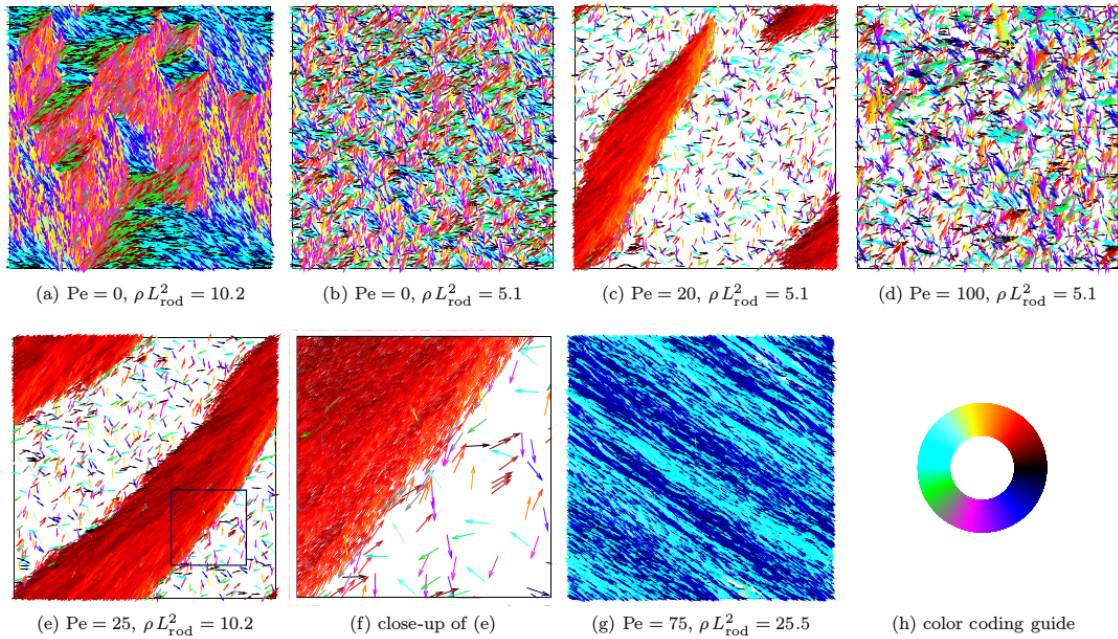


Figure 7.1: The collective structures of self-propelled rods in two-dimensional confinement feature isotropic states, small-scale clustering, giant clusters and lane formation dependent on Peclet number and density. Taken from [101].

Collective Behavior of Active Rods Systems of active rods display a more complex phase behavior than active spheres. In addition to clustering and jamming, giant clusters and lane formation have been observed as a resulting collective behavior [101]. The combination of self-propulsion and activity leads to an enhanced alignment of rods when they collide with acute angles. Figure 7.1 illustrates the behaviors observed for elongated rods in [101].

Swarming Swarming behavior, a general term encompassing the directed and coordinated motion of entities, is often observed in biological systems on the macroscale. Figure 1.2e shows an example of a fish swarm. Birds and many quadrupeds show swarm behavior as well, in these contexts often referred to as flocking and herding. In the scope of this work, let swarming refer to a type of collective motion that leads to a net displacement of the swarm, distinct from vortex formation. Vortex formation, illustrated for elongated bacteria, fish and active colloids in figs. 1.2a, 1.2b and 1.2d describes a type of collective motion in which the constituents propel circularly in a swirl type of structure.

Others Besides those here discussed, there are other types of different collective behaviors observed. For example, sperm cells feature a variety of patterns including trains of many cells [102, 103], vortex arrays [104] and coordinated aligned swarming structures when the beating frequencies are synchronous [105]. Hydrodynamic synchronization of beating cilia is another example, though then the constituents

are spatially fixed and do not migrate collectively.

For a more complete overview on collective behavior in biological and synthetic systems, see [4, 5, 7, 9, 20].

7.2 Collective Behavior of Dimers

In the following, results on the collective behavior of thermophoretic dimers are presented. The pair formation discussed in chapter 5 indicated that dynamics of colloidal swimmers modeled with MPC-MD may suffer from depletion. Using the procedures explained in chapter 6, care is taken that no artificial depletion will influence the dynamics of the collective systems discussed. The collective dynamics of thermophilic and thermophobic dimers show vastly different behaviors, such that they will be discussed separately. However, they share common features in their single-swimmer behavior and the same physical considerations determine their collective behavior, just to different extents.

When many dimers are immersed in a hydrodynamic solvent, their dynamics are determined by an interplay of phoretic effects, hydrodynamics, excluded-volume effects and thermal fluctuations. The phoretic effect will lead to the phoretic bead of a dimer being attracted to the hot bead of another dimer in the thermophilic or repelled by it in the thermophobic case. The hydrodynamic flow induced by the dimers' motion may induce a lateral repulsion or attraction, depending on the geometric construction details discussed in chapter 4. Excluded-volume effects in combination with self-propulsion can lead to MIPS. Jammed structures present the dense phase in MIPS, their stability depends on the time it takes a particle to reorient and leave the cluster again, and their process of formation will be called 'jamming' in the following.

A second kind of effect emerging from the interplay of excluded-volume and self-propulsion is specific to elongated swimmers. When two propelled rods collide at acute angles, they will align for some time. This enhanced lateral alignment effect [101, 106] will here be referred to as motility-induced attraction. The build-up of clustered structures is destabilized by two kinds of fluctuations, namely those stemming from the thermal nature of the solvent and those from other swimmers randomly colliding with the structures.

To predict and characterize the collective dynamics for different types of dimer construction requires knowledge of the relative importance of these effects, which is provided in the following sections by analyzing different simulation realizations of dimer ensembles.

7.2.1 Simulation Model

MPC-MD simulations of many dimers are computationally very costly. Therefore, a choice has to be made based on the known results on single dimers as to which parameters will be used. The dimer constructions of interest are chosen to feature

the size ratios $\gamma = s_p/s_h$ of 1 (symmetric) and 3 (asymmetric) as reference cases, as these show a most pronounced qualitative difference in their hydrodynamic behavior. A choice of $s_h = 2$ as the minimal size of the hot bead, for the $\gamma = 3$ dimer, is necessary to correctly resolve hydrodynamic flow fields [54]. This makes $s_p = 6$ necessary for $\gamma = 3$. As hydrodynamic interaction strength scales with the size of the colloids, in order for this to be of similar strength for both size ratios, $s_p = 6$ is chosen for $\gamma = 1$ as well, determining $s_h = 6$.

Artificial depletion is avoided by introducing displacements into the colloid-fluid interactions and tuning the inter-dimer interactions accordingly. As discussed in chapter 6, any chosen parameter set always presents a compromise between computational cost and the need to avoid depletion interactions. The influence the introduction of displacements Δ into the colloid-fluid interaction has is shown in terms of the propulsion velocity in fig. 7.2a and in terms of lateral hydrodynamic attraction in fig. 7.2b for the example of the thermophobic dimer with $\gamma = 3$. The

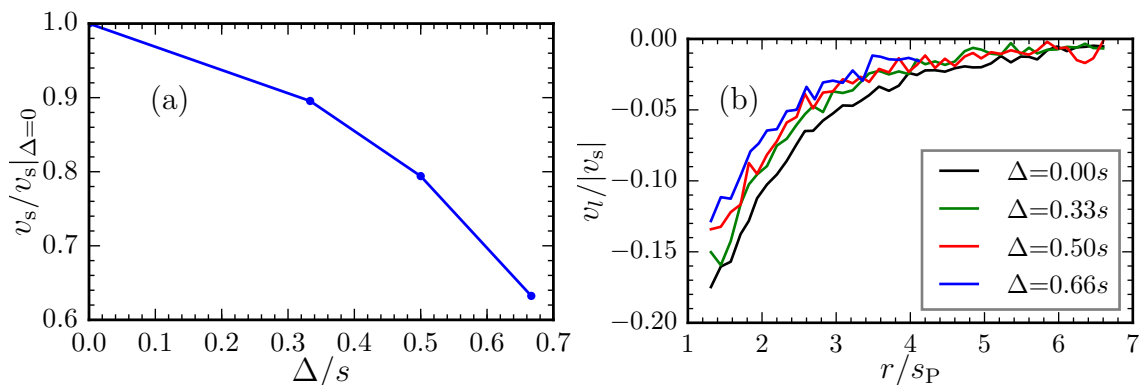


Figure 7.2: Properties of the reference thermophobic dimer with $\gamma = 3$ and fixed $s_p = 6$ when displacements Δ are introduced into the colloid-fluid interaction of the phoretic bead. **a)** Normalized propulsion velocity. **b)** Normalized fluid flow velocity along the lateral axis l .

qualitative features of the flow field are not influenced by the introduction of displacements. A certain reduction of thermophoretic propulsion velocity is to be expected, since the thermal diffusion factor depends on the colloid-fluid interaction range as discussed in section 3.4.2. In direct consequence, a slower swimmer will also feature a weaker flow field. Employing a displacement of $\Delta = s/2$ only reduces the propulsion velocity by ca. 20 %. Hydrodynamic lateral attraction is reduced as well, but only to a degree such that a significant influence on collective behavior is still to be expected. These observations lead to the choice of $\Delta = 0.5s$ as a standard value for choosing displacements.

Based on the choice of displacement, the other parameters of the reference dimers can be chosen. All interactions are modeled based on eq. (2.7). The colloid-fluid interaction of the phoretic bead of thermophilic swimmers has parameters $(s, \Delta, \varepsilon, n, r/a) = (6, 3, 1, 3, r)$ while that of thermophobic swimmers uses

(6, 3, 1, 24, a). The hot bead is modeled using parameters (2, 0.5, 1, 24, r) for $\gamma = 3$ and with (6, 3, 1, 24, r) for $\gamma = 1$. Modeling the hot bead with $s_h = 2$ using $\Delta = 0.5s_h = 1$ lead to integration errors in the simulations, such that here a smaller displacement of $\Delta = 0.5$ is chosen, which still enables avoiding depletion artifacts.

Colloid-colloid interactions in between bead i and j are described with parameters $(1.2(s_h + s_p/2), 0, 2.5, 24, r)$, i.e. with an additional separation $\delta = 0.2(s_h + s_p/2)$ to resolve lubrication and to avoid artificial depletion forces.

Heating is modeled by rescaling the temperature of fluid particles around the hot bead in a small layer of width $0.08s_h$ around the hot bead to $T_h = 1.5$ while keeping the overall fluid temperature at $\bar{T} = 1$. For collective systems, this choice will neglect any *shadowing effects* [107]. Shadowing could occur due to the light source not reaching certain hot beads as they are in the shadow of other colloids. Ignoring it corresponds to imagining colloids to have the same light refraction index as the solvent. Shadowing is expected to only have an important influence at high packing fractions and for dense clusters.

Simulations are performed in cubic boxes with periodic boundaries. Dimer swimmers are initially put on a grid, but with random orientations. Due to the high computational cost of the simulations, reference cases are chosen using a number of dimers $N = 100$ and a volume fraction of $\phi = 0.05$. Based on the results obtained there, other parameters may be checked. Typical runtimes are of the order 70,000 – 100,000 in simulation units.

7.2.2 Properties of Reference Dimers

The choice of reference constructions requires a re-examination of single swimmer properties. The single swimmer flow fields are shown, along with a characterization of lateral hydrodynamic interactions, in fig. 7.3 for both thermophilic and thermophobic dimers. As already discussed in chapter 4, the hydrodynamic interactions are reversed for thermophobic and thermophilic dimers. Thermophilic asymmetric dimers show long-ranged lateral hydrodynamic repulsion (c.f. figs. 7.3b and 7.3c), while thermophobic asymmetric dimers show long-ranged hydrodynamic lateral attraction (c.f. figs. 7.3d and 7.3f). Symmetric swimmers switch their lateral hydrodynamic behavior at short ranges, from repulsive to attractive in the case of thermophilic dimers (c.f. figs. 7.3a and 7.3c), while thermophobic symmetric dimers switch from short-range attractive to long-range repulsive (figs. 7.3d and 7.3e).

As evident from figs. 7.3c and 7.3d, the strength of hydrodynamic effects in the phobic and philic swimmers are similar. The thermophilic swimmers propel a bit slower than the thermophobic ones, with swimming velocities (measured along the bond direction towards the hot bead) of 0.013 in the asymmetric and 0.014 in the symmetric case, while the thermophobic ones reach -0.020 and -0.021 in the asymmetric and symmetric case, respectively. An overview of single dimer properties is given in table 7.1. Diffusion and rotational diffusion coefficients, obtained from measurements of the MSD and rotational MSD, are in a comparable range for all reference constructions with values in between 6×10^{-4} and 1.5×10^{-3} for the diffu-

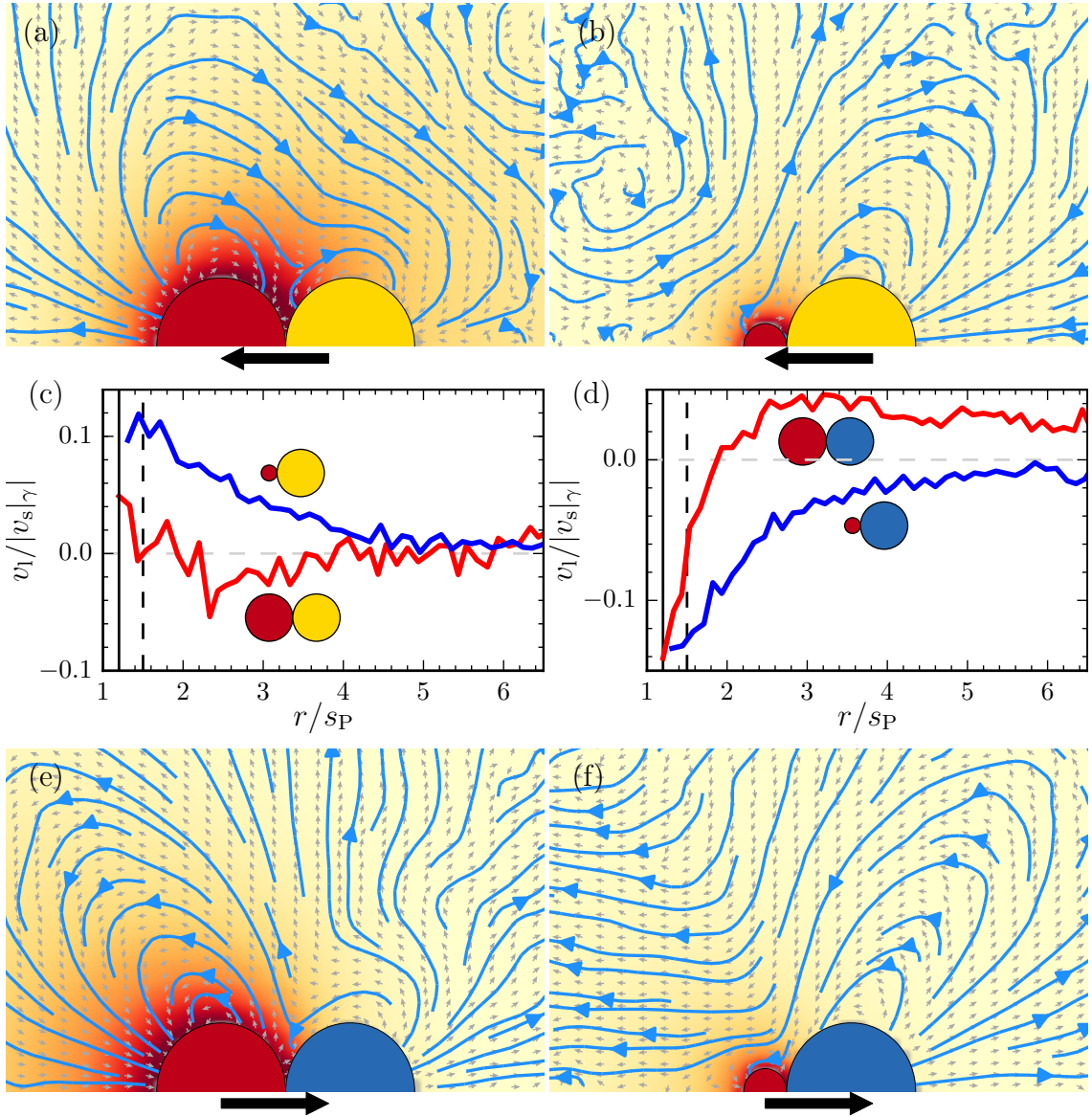


Figure 7.3: Flow fields and temperature fields for thermophilic (a),b),c)) and thermophobic (d),e),f)) dimer swimmers. **a,e)** same-sized beads, $\gamma = 1$. **b,f)** asymmetric beads, $\gamma = 3$. **a,b,e,f)** Black arrows indicate the propulsion direction. Background depicts the temperature field, blue lines and gray arrows show the flow field. **c,d)** Measurement of the flow velocity along the radial axis perpendicular to the swimmer orientation with origin in the center of the front bead (l -axis). Only values in the range accessible to other colloids are shown. Vertical solid and dashed black lines indicate colloid-colloid extra-separation distances of $\delta = 0.2$ and $\delta = 0.5$, the latter indicates the colloid-colloid extra-separation necessary to avoid artificial depletion when no displacements are used in the colloid-fluid interactions. Note that **a)** and **e)** only differ in the bead sizes from figs. 4.6g and 4.6a and are included here for clarity.

sion coefficient. Rotational diffusion coefficients lie in between 2×10^{-5} and 3×10^{-4} . The asymmetric swimmers feature higher values of both coefficients than the symmetric ones, which is consistent with their overall smaller size. The Peclet numbers are in the range 7–70, where the Peclet number Pe has been calculated as the ratio of propulsion to noise as $Pe = v_s/(D_r l_c)$, with l_c a characteristic length [70]. Typical values for the Peclet number of diffusiophoretic Janus particles, which are comparable to the phoretic dimers, lie in the range 5 – 200 [20, 70], which is consistent with the simulations.

Table 7.1: Single dimer properties for the two reference constructions of thermophobic and thermophilic dimers. Peclet numbers are calculated using eq. (2.13).

property	phobic $\gamma = 1$	phobic $\gamma = 3$	philic $\gamma = 1$	philic $\gamma = 3$
v_s	-0.021	-0.020	0.014	0.013
D	6.29×10^{-4}	1.15×10^{-3}	9.61×10^{-4}	1.41×10^{-3}
D_r	2.92×10^{-5}	9.89×10^{-5}	4.57×10^{-5}	2.46×10^{-4}
Pe	69	22	26	7

In addition to measuring the single swimmer properties of the reference constructions, simulations of pairs of these dimers were performed. The thermophobic swimmers used here did not show any formation of bound pair structures. Asymmetric thermophilic dimers did not show any formation of stable pairs either. Symmetric thermophilic dimers on the other hand, due to the larger phoretic attraction through the bigger hot bead, cling together in pair simulations for small times. No long-time stable configurations were observed though, the general behavior there is more akin to a slow-down upon contact, i.e. when the swimmers come close, their swimming velocity reduces and they slide along each other slowly, but always disconnecting again. Note that for colloids with a larger thermophoretic response these behaviors can be different.

7.2.3 Analysis of Clusters

In all collective simulations, some sort of clustering behavior is observed. To identify clusters, a distance based criterion is used. Two beads are here considered to belong to one cluster when their distance reaches a value lower than $1.32(s_i + s_j)$, which is 1.1 times the minimum colloid-colloid interaction distance. This distance criterion is complemented with a time criterion, only counting dimers as clustered when the distance criterion is fulfilled for times longer than 300.

The main cluster orientation is obtained by averaging all single dimer axes \mathbf{n}_i . The cluster velocity v_c is the average of the dimer velocities projected on this cluster orientation. Alignment is characterized by measuring the correlation of all dimer orientations in a cluster $\langle \mathbf{n}_i \cdot \mathbf{n}_j \rangle$. The radial distribution function $g(r)$ is measured

according to [45]

$$g(r) = \frac{V}{N_b^2} \left\langle \sum_a^{N_b} \sum_{b \neq a}^{N_b-1} \delta(\mathbf{r} - \mathbf{r}_{ab}) \right\rangle, \quad (7.1)$$

where V is the box volume, N_b the number of beads and $r_{ab} = r_a - r_b$ the vector connecting beads a and b . The $g(r)$ provides insight into structural properties. Angular alignment can be characterized by the spatial distribution of the mutual dimer-dimer orientation angle $\theta(r)$ [79], which is measured as

$$\theta(r) = \left\langle \sum_{j < i=1}^N \arccos[\hat{\mathbf{n}}_i(\mathbf{R}_i) \cdot \hat{\mathbf{n}}_j(\mathbf{R}_j)] \delta(R_{ij} - r) \right\rangle \quad (7.2)$$

where \mathbf{R}_i denotes the center of mass of dimer i . A value of 90° corresponds to perpendicular orientations, while 0° and 180° indicate perfectly parallel and antiparallel alignment. Random uncorrelated orientations also correspond to 90° .

Structural properties of clusters can also be obtained from the gyration tensor. This is defined as

$$S_{mn} = \frac{1}{2N^2} \sum_{a=1}^{N_b} \sum_{b=1}^{N_b} (r_a^{(m)} - r_b^{(m)})(r_a^{(n)} - r_b^{(n)}) \quad (7.3)$$

where $r_a^{(m)}$ is the a -th bead's position vector component m . \mathbf{S} is 3×3 matrix, that can be diagonalized to obtain the eigenvalues of the the gyration tensor Ξ_k^2 with $k = \{1, 2, 3\}$ which are chosen in a way such that $\Xi_1^2 \geq \Xi_2^2 \geq \Xi_3^2$. There are several shape descriptors that can be derived from the principal moments. More important for this work is that their respective ratios offer a measure for the cluster shape in terms of planarity. For example, a structure in which the three eigenvalues are very similar relates to a sphere, whereas one with the first two eigenvalues significantly higher than the third will be flat.

7.2.4 Langevin Dynamics

In order to estimate the influence hydrodynamic and phoretic effects have on the behavior of swimmers studied with MPC-MD, it is desirable to compare to a system that is very similar, but does not include these contributions. Such a system is provided when using Langevin Dynamics (LD), i.e. a numeric solution of eq. (1.6), $\ddot{\mathbf{r}} = -\zeta \mathbf{v} + \boldsymbol{\xi} + \frac{\mathbf{F}}{M}$. LD describes colloidal dynamics with an implicit background solvent, whose effect on colloidal motion is encoded in the friction coefficient ζ , the (thermal) noise $\boldsymbol{\xi}$ and the external force \mathbf{F} . The idea is now to choose parameters such that the system dynamics are as close as possible to those obtained with MPC-MD. M is the mass of the colloid, which is just chosen the same as in MPC-MD. As the viscosity $\mu_d = 7.92$ is well known to hold for the MPC fluid with the specified parameters, the friction of a colloidal particle can be estimated by using the Stokes-

Einstein relation as $\zeta = 6\pi\mu_d s$ and a damping force \mathbf{F}_{damp} be calculated considering the colloid's velocity \mathbf{v} . The thermal noise $\boldsymbol{\xi}$ is a Gaussian white noise defined by its fluctuation strength in eq. (1.9), $\mathbf{G} = 2k_B T \zeta \mathbf{I}$, and is applied considering the average temperature \bar{T} of the MPC-MD simulations to contribute a random force $\mathbf{F}_{\text{random}}$. From the swimmer velocities v_s obtained in MPC-MD, the corresponding driving force $F_{\text{propulsion}} = v_s \zeta$ is calculated and applied to the phoretic particle along the bond direction \mathbf{n} .

The total force $\mathbf{F}_{\text{total}}$ on a colloid in LD is then given as the sum of all these contributions as

$$\mathbf{F}_{\text{total}} = \mathbf{F}_{\text{pair}} + \mathbf{F}_{\text{damp}} + \mathbf{F}_{\text{random}} + \mathbf{F}_{\text{propulsion}} \quad (7.4)$$

where \mathbf{F}_{pair} includes all contributions from direct pair-wise interactions with other colloids and

$$\mathbf{F}_{\text{damp}} = -\frac{M}{\mu_d} \mathbf{v}, \quad (7.5)$$

$$\mathbf{F}_{\text{random}} = \sqrt{2k_B \bar{T} \mu_d} \boldsymbol{\xi}. \quad (7.6)$$

The propulsion force is only applied to the phoretic particle along the dimer orientation \mathbf{n} . To reach the desired propulsion velocity, the friction of both colloids of the dimer has to be accounted for and $\mathbf{F}_{\text{propulsion}}$ is therefore given by

$$\mathbf{F}_{\text{propulsion}} = (\zeta_h + \zeta_p) v_s \mathbf{n} \quad (7.7)$$

where the subscripts refer to the hot (h) and phoretic bead (p). The directionality accounting for the propulsion direction of thermophilic and thermophobic dimers results from the sign of the swimming velocity v_s .

7.2.5 Collectives of Thermophilic Dimers

Simulations of large ensembles of thermophilic dimers show clustering into unmoving aggregates. After an initial phase in which the dimers freely propel, they start to form large, unmoving and long-time stable clusters, which continuously grow by new dimers colliding and getting attached. In the limit of long simulation times, one giant cluster including nearly all dimers remains. Snapshots from simulations illustrating the observed behavior are shown in fig. 7.4. The clustering dynamics do not differ much between dimers with the two chosen size ratios. Figures 7.4a and 7.4b show snapshots from a simulation of $\gamma = 3$ dimers. Two unmoving structures have formed there. The remaining free dimers will in the end also attach to either one, and the two structures eventually combine to one giant cluster. This process will take a long time, as the formed structures only move by Brownian motion. Depending on the initial configuration and the randomness induced by the noise, single giant clusters were observed in different realizations. Such an example

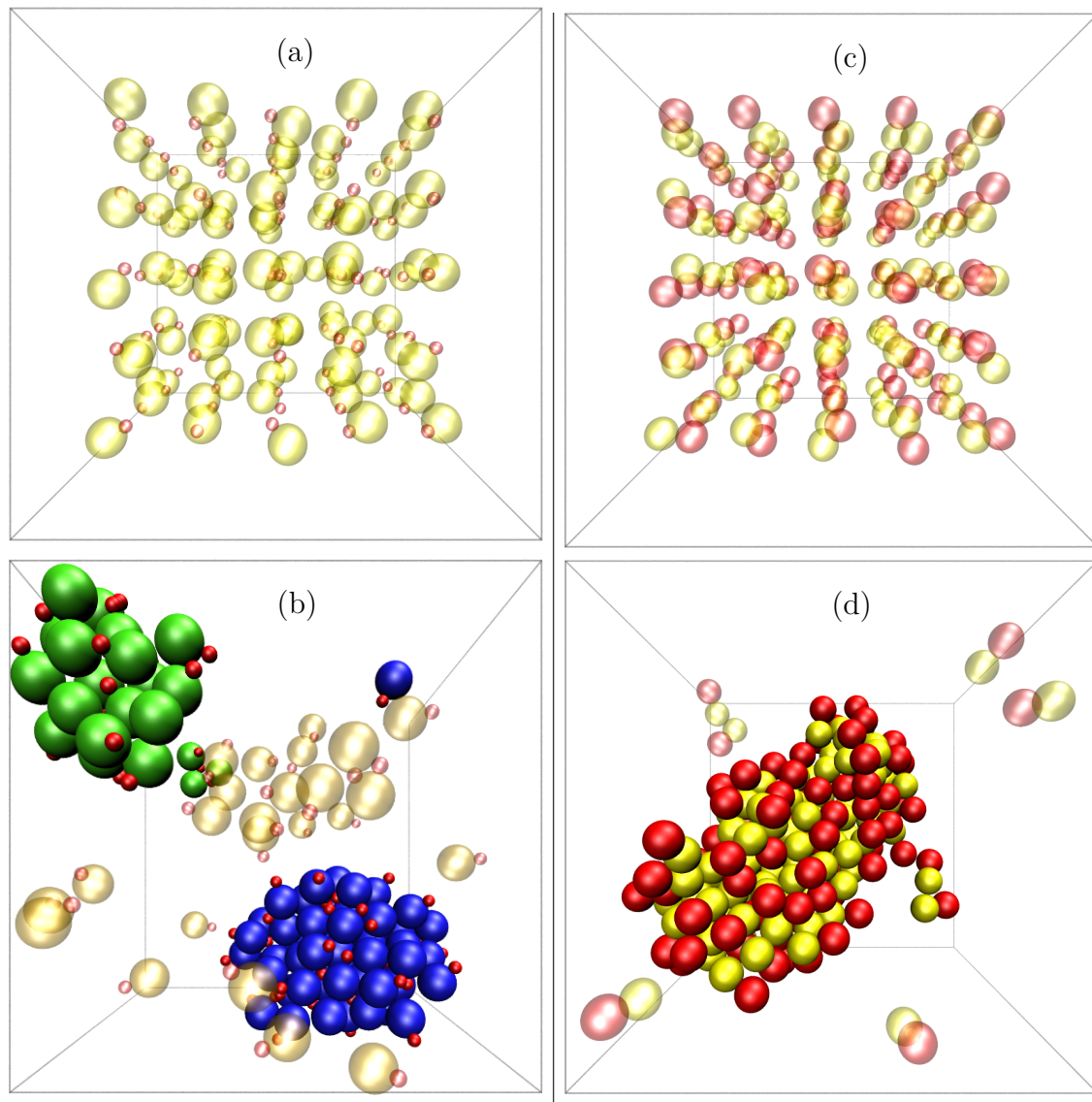


Figure 7.4: Collective systems of thermophilic dimers. Hot beads are colored red. Free dimers are depicted translucent, with yellow phoretic beads. Clustered dimers are colored solid, with phoretic beads colored according to cluster identity. Top picture shows initial state, bottom picture a representative configuration of unmoving clusters at a later stage. **a,b)** Asymmetric dimers with $\gamma = 3$. **c,d)** Symmetric dimers with $\gamma = 1$.

is shown in figs. 7.4c and 7.4d, though for the symmetric $\gamma = 1$ dimer. Only a few free dimers still remain there, which will soon attach to the large structure.

The most important physical features of these systems are already evident from the snapshots. Thermophilic dimers move with the hot bead at front. However, many dimers in the clustered structure have the hot bead pointing outwards, but still remain attached to the cluster and do not just swim away. This shows that the clustering is not induced by jamming or motility-induced attraction, as these steric effects would not hinder a dimer pointing outwards from just swimming away. As the structures are unmoving, no hydrodynamic flow fields can build up, such that related effects can only play a very minor role. The only effect left that can explain the freezing of dimers into unmoving clusters with hot beads pointing outwards is then the phoretic attraction. Phoretic beads are drawn towards the hot beads of other swimmers, and will aim at being surrounded by as many of them as possible. This leads to the swimmers stopping to propel, due to two simultaneous effects. For one, a phoretic bead between, for example, two opposite lying heat sources will not move, as the driving forces cancel. Secondly, the temperature distribution around the phoretic bead will become more uniform since the heat sources are close to the phoretic bead, leading to its surface getting more or less uniformly hot. As the phoretic driving force is induced by the gradients of temperature along the surface, this will diminish it. The hot bead will not react to any exterior temperature field, but the phoretic bead of the swimmer will be drawn towards the hot beads of another dimer, be it free or already part of a cluster. If the temperature field then is uniform enough, the driving force is diminished sufficiently and the dimer stays part of the cluster, though its front bead is pointing outwards. Note that, in contrast to the structures resulting from depletion presented in chapter 5, artificial depletion does not play a role in the formation of the structures here, but their stability solely stems from the phoretic effect.

Structural properties of the formed clusters are obtained by averaging over different realizations, typically 3 to 5, at a later stage of the simulation, where the clusters are already formed and mostly stable. The dimer and cluster dynamics can be characterized by considering the cluster velocity v_c , i.e. the average dimer's velocity projected on the cluster orientation, as a function of cluster size, as shown in fig. 7.5a. For both symmetric and asymmetric dimers, the cluster velocity decays very steeply and reaches zero already for cluster sizes between five and ten. This represents that unclustered dimers move freely and shows that even small agglomerates suffer a significant penalty in terms of propulsion speed due to the reduction in phoretic driving force. The decay is a bit faster for symmetric dimers, most likely because the relative importance of the phoretic effect is stronger here due to the larger hot beads.

The crystal-like structure of formed clusters is seen in the radial distribution function, shown in fig. 7.5b for phoretic-phoretic beads and in fig. 7.5c for hot-hot beads. The sharp peaks, especially in fig. 7.5b, are typical for solid-like structures. For symmetric swimmers, both the phoretic-phoretic and the hot-hot radial distribution functions show peaks at contact and at around $2(s_i + s_i)$, indicating a

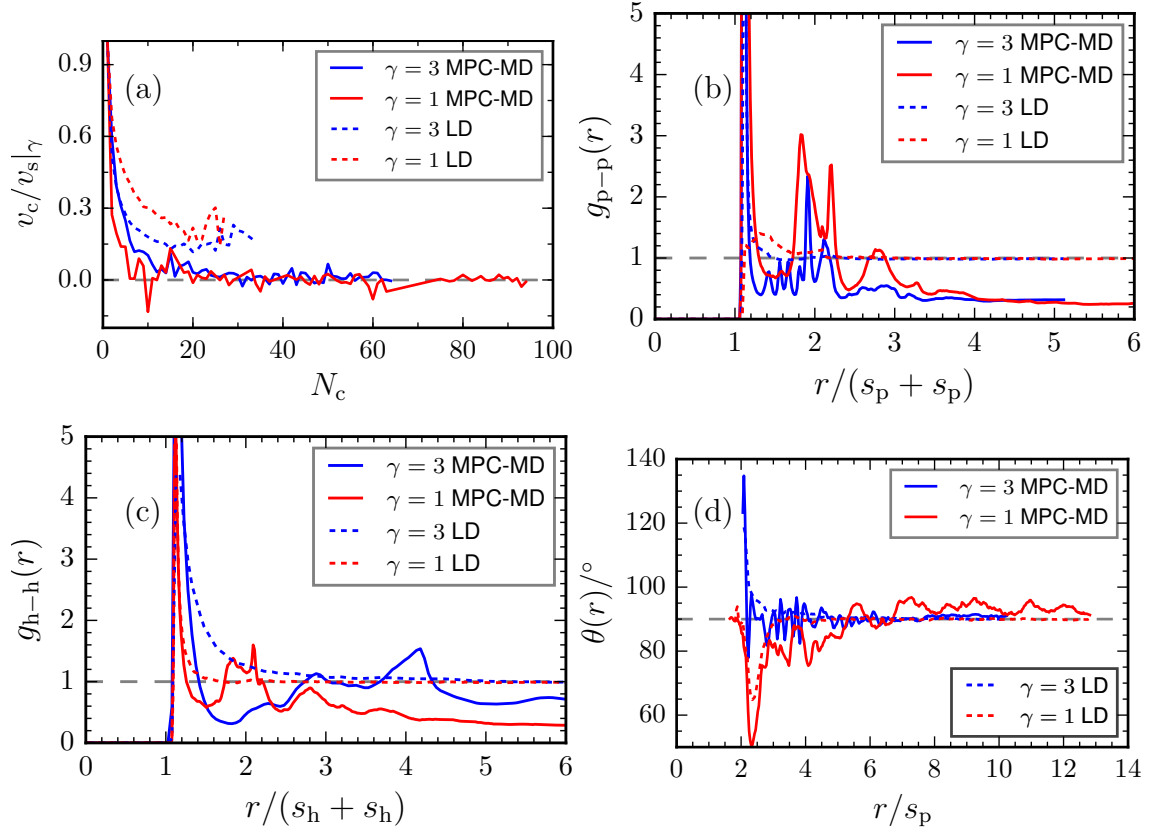


Figure 7.5: Properties of ensembles of $N_c = 100$ thermophilic dimers with $\gamma = 1$ (red) and $\gamma = 3$ (blue) at volume fraction $\phi = 0.05$. Solid lines correspond to results obtained with MPC-MD, dashed lines to those obtained with LD. **a)** Cluster velocities v_c normalized by single dimer velocity v_s . **b,c)** Radial distribution functions considering phoretic-phoretic beads (**b**) and hot-hot beads (**c**). **d)** Spatial distribution of dimer-dimer angle, according to eq. (7.2).

second coordination layer one bead farther away. The asymmetric dimers' phoretic beads show the same peak at $2(s_i + s_i)$, whereas it is missing in their hot-hot radial distribution function. If a hot bead of an asymmetric dimer with $\gamma = 3$ is mostly surrounded by phoretic beads, the next hot bead will be behind the phoretic bead and appear as a peak at $r/(s_h + s_h)$ in the hot-hot $g(r)$, and such a peak is indeed visible in fig. 7.5c. However, though the highest value is very close to $4(s_h + s_h)$, the peak is broad, going roughly from 2.8 – $4.3(s_h + s_h)$, which indicates that the hot beads are rather randomly distributed around the phoretic beads. Angular alignment is characterized by the spatial distribution of the mutual dimer-dimer orientation angle $\theta(r)$, which is shown in fig. 7.5d. The quick decay to 90° in both cases indicates that there is not much alignment in any of the crystalline structures. The opposite lying first peaks around 2.0 to $2.5r/s_p$ indicate that there is a tendency to have symmetric dimers rather parallel and asymmetric dimers anti-parallel aligned at close distances.

Studying the same system using LD leads to a completely different behavior of dimers. This is in fact expected since no explicit attractive interactions are present and the dimers only cluster through collisional processes. Characteristics of the resulting dynamic and structural properties are shown by the dashed lines in fig. 7.5. Figure 7.5a shows that smaller clusters with non-vanishing average velocity form in LD, which confirms a very different behavior as compared to MPC-MD. Nearly no structural properties but for the peak at contact are evident in the radial distribution functions obtained with LD, as shown in figs. 7.5b and 7.5c. Opposed to MPC-MD, this indicates that no crystalline states form. While LD lacks the longer-ranged angular correlations in the angle distribution shown in fig. 7.5d, the behavior at short ranges is comparable to MPC-MD, where symmetric dimers are more likely to be aligned parallel, while asymmetric dimers are anti-parallel. Since this effect is evident in both MPC-MD and LD, it is most likely due to the collisional dynamics. When two symmetric dimers collide at acute angles, they will likely align parallel due to motility-induced attraction. This is different for asymmetric dimers. Having the small bead at front, it is likely that collisions take place with the larger back bead. A probable mechanism is that the two dimers do not crash with their front beads, but in passing get stuck with their back beads touching. Such a configuration has the dimers going in opposite directions, i.e. anti-parallel aligned, as evident in fig. 7.5d. The collision dynamics seem to provide the main contribution to the behavior in MPC-MD as the curves are quite similar to LD at the short ranges now considered. The discussed behaviors of symmetric and asymmetric dimers are also somewhat visible in the graphic depictions in figs. 7.4b and 7.4d.

The quantifications discussed are in agreement with the physical mechanism of phoretic clustering. Phoretic clustering will always induce unmoving clusters of similar structure, more or less independent of the number of swimmers and volume fraction. The formation dynamics may of course be slower for lower volume fractions, and many unmoving clusters will form that take long times to meet and agglomerate together as they just move by Brownian motion. To confirm this, a simulation of symmetric dimers with a higher number of swimmers $N = 200$ at a lower volume fraction of $\phi = 0.03$ was performed, with a comparable runtime to those discussed already. The resulting behavior is exactly as expected. An illustrating snapshot as well as characterizations in terms of the cluster velocities and radial distribution function are shown in fig. 7.6. It is visible in the snapshot in fig. 7.6a that, in comparison to the reference case shown in fig. 7.4d, more clusters of lower size are formed. This is mainly a result of the runtime of the simulation. Due to the lower volume fraction, it is less likely for swimmers to meet and smaller clusters build up first. These will eventually still form one large cluster but not within the frame of time considered. The cluster velocities and radial distribution function in figs. 7.6b and 7.6c show a course very similar to that observed in fig. 7.5, indicating very similar dynamics and structures. The radial distribution function at lower volume fraction in fig. 7.6c shows qualitatively the same peaks as that at higher volume fraction in fig. 7.5b, indicating the structural properties to be

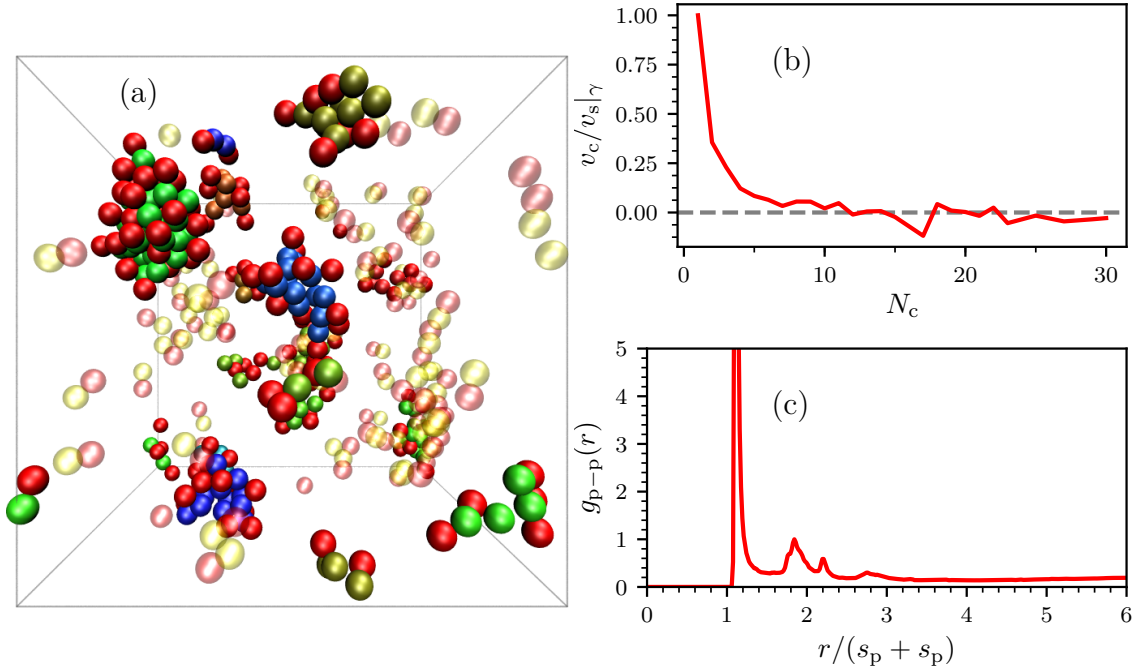


Figure 7.6: Snapshot (a) and system properties (b),c) of a system of $N = 200$ thermophilic dimers with $\gamma = 1$ at volume fraction $\phi = 0.03$. Color coding is the same as in fig. 7.4. b) Cluster velocities v_c normalized by single dimer velocity v_s . c) Radial distribution function considering phoretic-phoretic beads.

the same. The lower absolute values are due to the fact that the system at lower volume fraction still features more free dimers. The mechanism working the same in a bigger system at lower volume fraction also ensures that finite size effects are unlikely to influence these dynamics.

7.2.6 Collectives of Thermophobic Dimers

7.2.6.1 Swarming Behavior

Thermophobic dimers show a collective behavior very different from that observed for thermophilic ones. In simulations of many thermophobic dimers, no long-time stable clusters form. Instead, one observes a dynamic clustering into moving aggregates with a pronounced tendency to align, with a front-like propulsion in a layer type of structure. Illustrating snapshots of symmetric and asymmetric dimers are shown in fig. 7.7. It can be made out that in both cases, clusters with more or less random orientations as well as some with pronounced alignment are formed. A typical random cluster is for example the light blue one in fig. 7.7b. Strong alignment can be seen for the golden cluster in fig. 7.7a and the green one in fig. 7.7b. Notably, the green one of asymmetric dimers has a higher cluster size as well as a more coherent orientation. These features are representative also of the typical

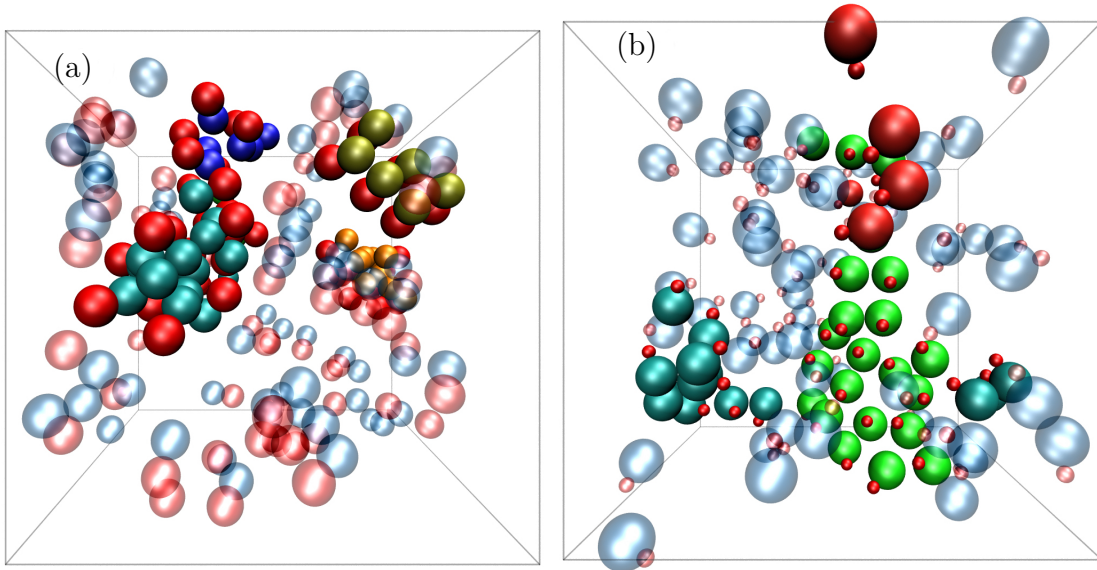


Figure 7.7: Snapshots of ensembles of $N = 100$ thermophobic dimers of size ratio $\gamma = 1$ (a) and $\gamma = 3$ (b). Non-assembled dimers are translucent, with red heated beads and blue phoretic beads. Dimers assembled in clusters of size five or larger are solid, with red heated beads and phoretic beads colored according to cluster identity.

dynamics observed. An indication of the most typical cluster sizes can be found in the plateaus of the cluster size probability distribution in fig. 7.8a, indicating $N_c = 10$ to 20 for $\gamma = 1$ and $N_c = 30$ to 55 for $\gamma = 3$. To compare the two types of construction, consider the reference system size of $N = 100$, given by the solid blue and red lines in the figure. Neither construction forms long-time stable aggregates due to the phoretic repulsion and thermal noise. However, the asymmetric dimers tend to not only form bigger, but also faster (c.f. fig. 7.8b) and more coherently oriented clusters (c.f. fig. 7.8c). For symmetric dimers, the oriented cluster velocity drops quickly as a function of cluster size to roughly $0.2v_s$. The same function for asymmetric dimers drops much slower and strongly shows a pronounced plateau at roughly $0.4v_s$, reaching up to ca. 60 swimmers. The course of the clusters' orientational correlation is similar. While that of symmetric dimers drops quickly to zero, the decay is slower for asymmetric dimers and reaches a plateau at ca. 0.12, with the same range as for the cluster velocities.

Symmetric dimers show a tendency towards aligned propulsion in small, short-lived agglomerates. Asymmetric dimers tend to move in front-like, flattened swarms that also persist for longer periods of time, propelling together over one to several dimer lengths. Note that the velocity and orientation of moving flattened swarms are underestimated by the values given in fig. 7.8, since these averages also account for non-moving clusters formed by the collisions of smaller clusters.

Before discussing the physical origin of the swarming behavior observed, note that

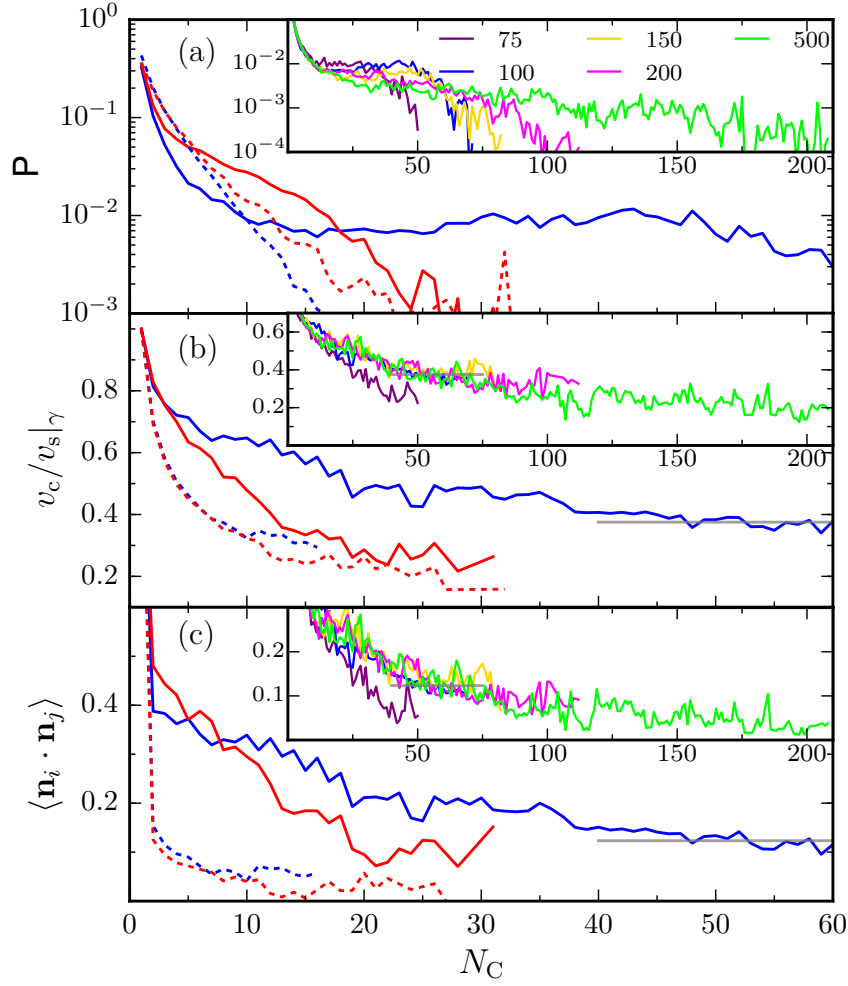


Figure 7.8: **a)** Averaged probability for a dimer to be in a cluster of size N_C . Blue (dark) lines stand for asymmetric dimers and red (light) for symmetric dimers. Solid lines correspond to hydrodynamic simulations (MPC-MD), dashed lines to non-hydrodynamic results (LD). **b)** Normalized cluster velocities as a function of normalized cluster size. **c)** Orientational correlation of dimers within the same cluster as a function of the normalized cluster size. **b,c)** Solid gray lines are a guide to the eye indicating a saturation value. The corresponding inlays show results for asymmetric dimers in systems of size 75 (green), 150 (gold) 200 (pink) and 500 (green) swimmers, blue line is the same as in the main figure. Red and blue datasets are averaged over five realizations and datasets in inlays over two; both with runtimes of around 70,000. LD results are averaged over 8 realizations.

motility-induced attraction alone could account for oriented propulsion. This effect can however not be strong, as the dimers feature very low aspect ratios. To estimate its influence, the full hydrodynamic simulations are compared to LD simulations, in which hydrodynamics and phoretic effects are completely disregarded. Results are shown in fig. 7.8 with dashed lines. LD leads for both considered geometries to

nearly identical results, emphasizing that the difference between the two observed in MPC-MD simulations originates in their different hydrodynamic and phoretic behavior. Only small, short-lived aggregates with low orientational correlation form in LD, and very quickly dissolve again. The low orientational correlation indicates that jamming is the main clustering mechanism in LD. The residual orientational correlation still being non-zero and positive is due to motility-induced attraction, since this favors aligned propulsion already for the dimers, though their aspect ratio is very low. That velocities and orientational correlations are much lower in LD for the asymmetric dimer shows that motility-induced attraction is not the cause for the emergence of swarming structures. The lower orientational correlation of symmetric dimers in LD indicates that their short-ranged hydrodynamic attractions enhance their alignment quite strongly (cf. blue lines in fig. 7.8c). The importance of short-ranged hydrodynamic interactions is currently discussed for various swimmer types, and in particular has been observed to be of importance in other colloidal systems [86].

The significant differences in collective behavior of these construction types originate in the dimers' geometries and their consequences on hydrodynamic behavior. Recalling the measured flow fields of fig. 7.3d, asymmetric dimers show long-ranged hydrodynamic attraction, while symmetric dimers show long-ranged hydrodynamic repulsion and short-ranged weak attraction. Then, the emergence of swarming structures in the particular sheet-like geometry is based on the interplay between phoretic repulsion and hydrodynamics. Phoretic repulsion is mainly affecting other swimmers in the propulsion direction, especially keeping any other dimer from attaching to the front or rear. Hydrodynamic attraction works lateral to the propulsion direction, drawing other dimers near. In combination, front-like swarming in single-layered fronts results. Thermal fluctuations and random collisions destabilize the emerging structures. Stability and velocity are also decreased as the formation of planar-like sheets is hydrodynamically unfavorable, hence friction is increased as compared to single dimers.

The swarm size in the reference system of 100 asymmetric dimers is limited by the simulation box size. To gain insight into whether one can expect them to form very large swarms, extensive simulations with up to 500 swimmers were performed. Their results are shown in the inlays of fig. 7.8. Snapshots of the largest system and a swarming cluster are shown in fig. 7.9. The results obtained from the largest system indicate that clusters with more than ca. 200 constituents are not being formed anymore. The largest clusters do not show a relevant velocity and orientational correlation anymore, what indicates that they are resulting from collisions of two or more swarming clusters. Up to the size of 150 however, significant cluster velocities and orientational correlations are still observed. As these swarms are small enough as compared to the simulation box size, this limit will likely not depend on the system size but rather on the stability of hydrodynamic lateral attraction as compared to both thermal fluctuations as well as the increased friction due to the planar-like geometry. This limiting size will however strongly depend on various other system parameters such as the volume fraction, single swimmer Peclet

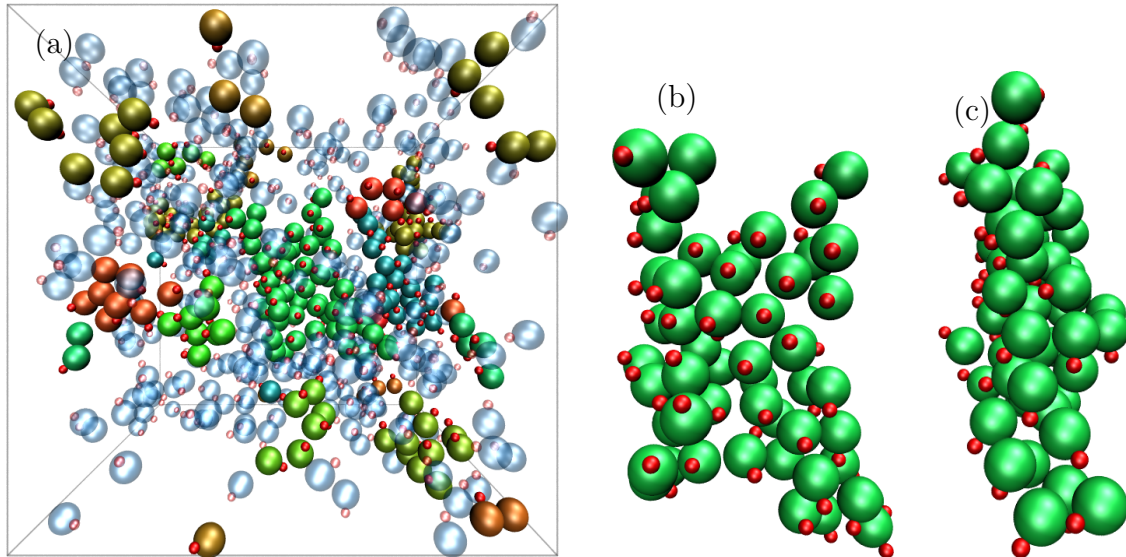


Figure 7.9: Snapshots of an ensemble of $N = 500$ thermophobic dimers of size ratio $\gamma = 3$. **a)** shows the whole simulation box, **b)** a view from the back and **c)** a view from the side on a large swarming cluster in it. Non-assembled dimers are translucent, with red heated and blue phoretic beads. Dimers assembled in clusters of size five or larger are solid, with heated beads colored red while phoretic beads are colored according to cluster identity.

number, and particle geometry. Before considering such influences, the structural characteristics will be discussed still within the scope of the reference system.

7.2.6.2 Structural Characteristics

The positive orientational correlation indicates alignment of the swimmers. However, it does not provide any information about the actual cluster shape. High orientational correlations would also result from a chain-like propulsion. To quantify the cluster shape, and in particular its planarity, the gyration tensor is measured. Unfortunately, a precise quantification is not possible due to the large stochasticity of the cluster configurations in conjunction with the prohibitive computational cost of the simulations. The results obtained suggest a ratio of around 10 of the largest to smallest eigenvalue for many cluster sizes of both asymmetric and symmetric dimers, albeit with large errors. The ratio of the intermediate to smallest eigenvalue is then around ca. 4, again with large errors. It is worth to remind that clustering through jamming also happens and is included in the averages. Though not precisely quantifying structural properties, these values indicate that the alignment in swarming stems from structures akin to planar fronts, and definitely not from line-like formations.

Structural characteristics are shown in fig. 7.10. These take into account all dimers or beads in the system, without differentiating between clustered and free

swimmers. The spatial distribution of dimer-dimer angles in fig. 7.10a clearly indi-

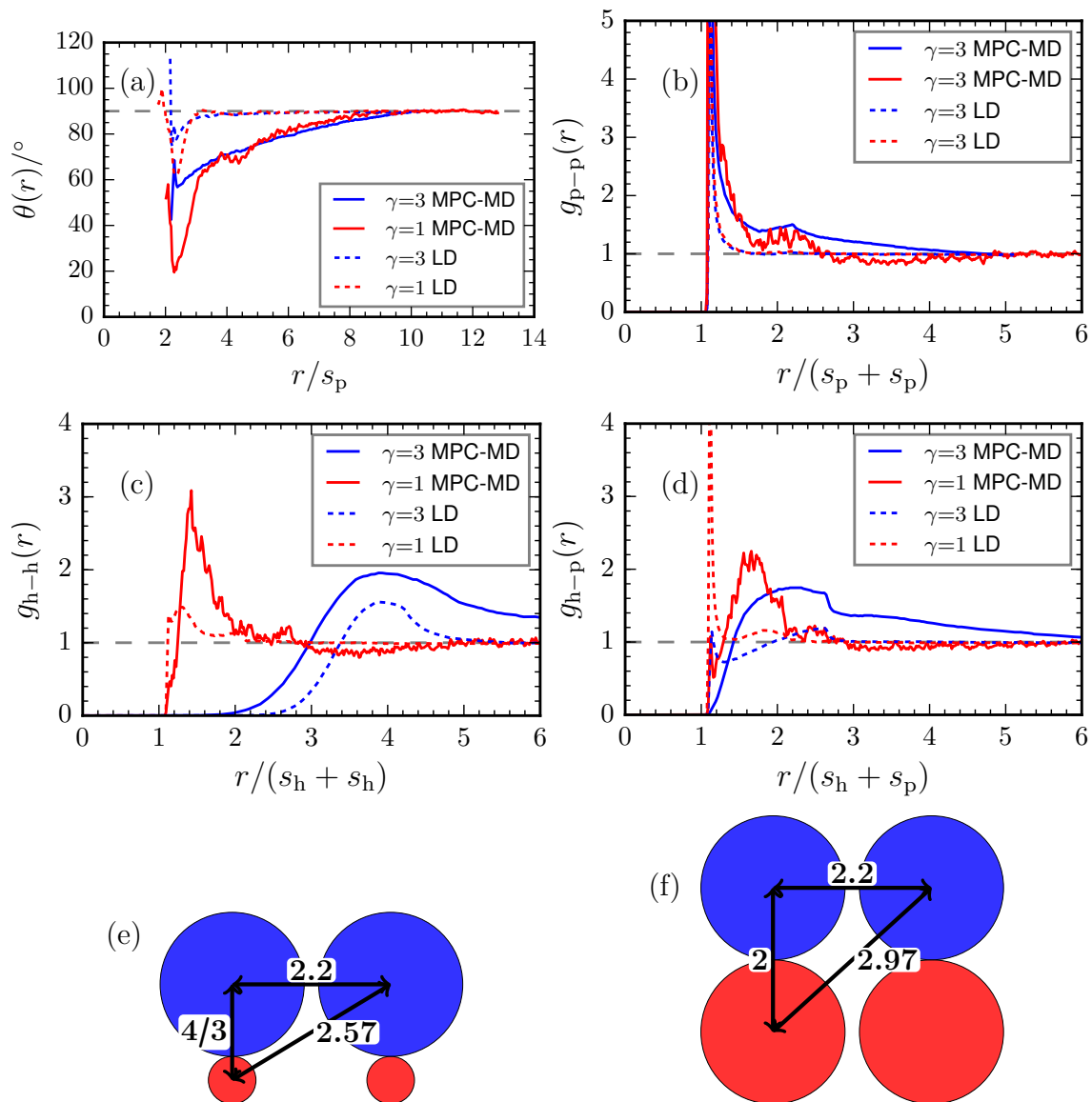


Figure 7.10: Structural features of collectives of thermophobic dimers. **a)** Spatial distribution of dimer-dimer angle, according to eq. (7.2). Radial distribution functions are shown for phoretic-phoretic beads (**b**), hot-hot beads (**c**) and hot-phoretic beads (**d**). Blue lines stand for asymmetric dimers and red for symmetric dimers. Solid lines correspond to hydrodynamic simulations (MPC-MD), dashed lines to non-hydrodynamic results (LD). **e)** and **f)** sketch a perfectly aligned configuration with phoretic beads at contact and show the relevant lengths in units of s_p , to relate them to the radial distribution functions in **b)**-**d**).

cates that it is more likely to have two dimers aligned than not, both for symmetric as well as for asymmetric dimers. In LD simulations, this correlation is very short

ranged and greatly reduced as compared to the MPC-MD results, confirming the already made assumption that motility-induced attraction has a rather weak effect in these systems. In the MPC-MD results, it is observed that at short ranges, the angular correlation is stronger for symmetric than for asymmetric dimers, which is not directly consistent with the different strengths of hydrodynamic lateral attraction observed in the quantification of the single dimer flow field in fig. 7.3d. It is then likely due to the combined effect of hydrodynamics with motility-induced attraction, which is stronger for symmetric dimers as visible in this figure when comparing the dashed red to blue line. Both types of construction show long-ranged alignment, which can only result from the hydrodynamic and phoretic effects. Of these two, phoresis will not induce alignment. The long-range alignment is comparable for both types of construction. Though their lateral hydrodynamic behavior is opposite, the effect on alignment is similar.

The radial distribution functions in figs. 7.10b to 7.10c indicate, most of all, that there is more structure inherent in clusters formed in MPC-MD simulations resolving hydrodynamics and phoresis than in those formed in LD. Sketches of aligned dimer, highlighting the relevant lengths to relate the radial distribution functions to, are shown in figs. 7.10e and 7.10f. The phoretic-phoretic radial distribution function in fig. 7.10b shows a pronounced peak at contact for both MPC-MD and LD, that is broadened towards higher distances in MPC-MD with an additional small peak around four times the colloid-colloid interaction range at $(2.2(s_p + s_p))$. This second peak indicates that dimers order in a second layer, which is consistent with a higher number of constituents in clusters that also extend longer. While the phoretic-phoretic radial distribution function has a similar course for both types of dimer construction, the hot-hot radial distribution function shown in fig. 7.10c is pronouncedly different for them. That of symmetric dimers shows a peak at contact, though less pronounced and oriented towards higher distances both in MPC-MD and LD as compared to the phoretic-phoretic one. This indicates a higher probability for dimers to collide with the front than with the rear, which is to be expected due to the propulsion direction. This is also true for the asymmetric dimers, though here the peak is shifted towards higher distances, broadly distributed around ca. $8s_h$ for both MPC-MD and LD. This indicates that it is nearly impossible for hot beads to touch due to the propulsion with the phoretic bead at front, which stands in strong contrast especially to thermophilic dimers (c.f. fig. 7.5c). The hot-phoretic radial distribution function does start at contact in both cases, but not with a pronounced peak as for the phoretic-phoretic one. As visible in fig. 7.10d, the peaks build up to show a maximum at larger distances. Notably, the peaks are at roughly the same distance for both asymmetric and symmetric dimers, as the normalization for the two is different with s_h taking on values of 2 and 6 respectively. This radial distribution function also shows the most prominent differences in between MPC-MD and LD simulations. In LD, it is in no way hindered for hot and phoretic beads to touch. In fact, it is just more likely for swimmers to collide head-on, but it does statistically happen that they will collide head-rear, such that there is a small peak at contact.

7.2.6.3 Finite Size Effects

In systems of single swimmer, the finite size of the simulation box will influence the propulsion velocity as well as the hydrodynamic behavior, mainly in terms of limiting the maximum range of the flow field, as discussed in section 3.3.1.1 and section 4.1.4.1. In a system of many thermophobic dimers, these effects will also be present, but screened. A stronger effect for these systems is that the swarm size in simulations of asymmetric dimers can be limited. As observed in the largest simulations of thermophobic dimers, the swarms are stable up to ca. 150 constituents, with the largest cluster observed containing a bit more than 200 dimers. Reaching these values is of course impossible when not enough dimers are present, which in that sense limits the swarm size. In addition to that, a small simulation box may also have a rather specific effect in this system. When the simulation box is small enough as compared to a swarm, it may happen that one cluster gets so large that the system percolates. The percolated structure gets stabilized and grows due to the effect of periodic boundary conditions. The stabilized structure contains in the end nearly all dimers, which become part of one huge, very coherently aligned front that propels fast and as a whole with only little number fluctuations. Illustrating snapshots of a back and side view of such a percolated structure are shown in fig. 7.11. This behavior was only observed in few realizations of the system dynamics and

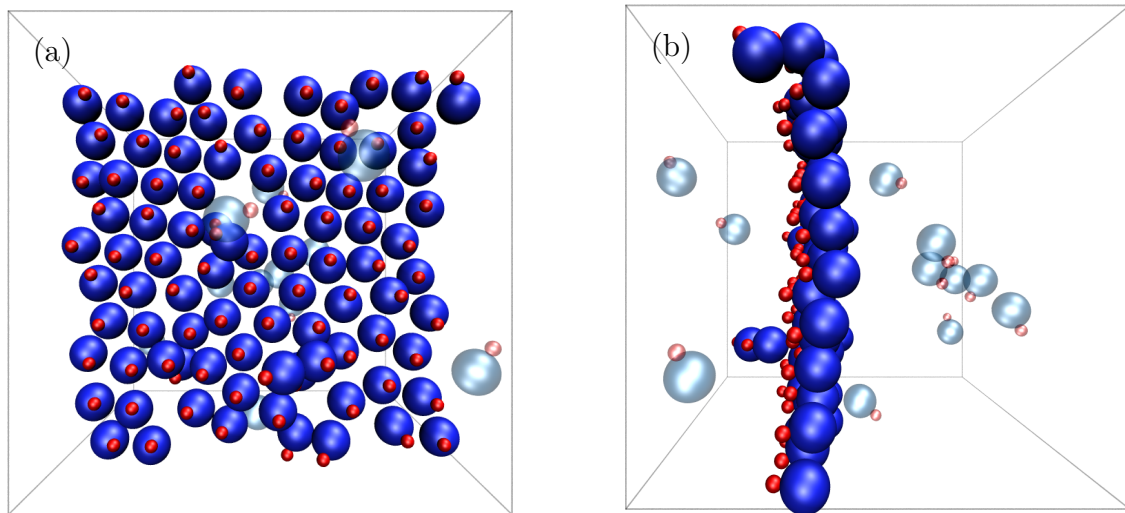


Figure 7.11: Snapshots of a percolated formation of asymmetric dimers. **a)** shows a view from the back, **b)** from the side.

the analysis discussed so far did not consider simulations that showed percolation. The increased stability of the percolated front is due to a finite size effect. When the swarm extends over the whole simulation box, fluid can not very well stream at the now-vanished sides of the swarm, thereby friction is reduced and the structure accelerates. No percolation was observed in realizations with more than 100 swimmers, though it may probably happen in systems with less dimers than constituting

the maximum swarm size. Although these very coherent structures result from a finite size effect, they indicate that additional stabilization mechanisms may favor further the formation of coherently aligned swarms of dimers.

7.2.6.4 Effect of Volume Fraction

The volume fraction ϕ will influence the collective dynamics. Before discussing its effect, it should be noted that all the MPC-MD results presented in the following are to some extent preliminary. Due to the high computational cost, the datasets are extracted from just one realization of the system dynamics. To draw definite conclusions and offer precise quantifications, future work will need to consider more simulations to provide reliable statistics. However, the main trends can already be extracted quite clearly, and are presented in the following.

The swarming behavior of asymmetric dimers discussed so far is only possible at intermediate volume fractions, such as in the reference system which features $\phi = 0.05$. If ϕ is too low, the swimmers will meet too rarely to form larger structures as the dissolution of clusters takes place before more dimers can arrive at the agglomerate. If it is too high, the clustering mechanism will be dominated by jamming and frequent collisions that are, due to the close packing, to a lesser degree influenced by the hydrodynamic interactions. Results on the collective behavior of dimers with size ratios $\gamma = s_p/s_h$ of 3, 2, and 1 are shown in fig. 7.12.

Consider first the results obtained using the asymmetric dimer with $\gamma = 3$ in fig. 7.12a. For low volume fractions, only small clusters form, with sizes only up to $N_c = 5$ at $\phi = 0.01$ and $N_c = 20$ at $\phi = 0.025$. At the lowest volume fraction, there is nearly no orientational correlation observed for these small clusters. This is attributed to the very limited statistics in this system, as collisions of dimers are a rather rare event in this dilute regime. To discuss the influence of volume fraction, it is sufficient to observe that clearly no swarming behavior emerges and this is referred to as the *dilute phase*. For the next higher volume fraction, $\phi = 0.025$, all cluster properties show a course similar already to the reference system, but clusters do not reach sizes larger than ca. 20. This points to the swarming behavior starting to develop, but due to the lower density the lifetime of aggregates is too short for more dimers to attach to those structures that have built up. This phase is called *small swarms*.

At $\phi = 0.075$, the system shows a similar behavior to the reference system at $\phi = 0.05$. At both volume fractions swarming behavior emerges, showing also similar plateaus in cluster velocity and orientational correlation of clusters. This indicates $\phi = 0.075$ to also be in the aforementioned intermediate range of volume fractions, in which swarming behavior can be observed, and this is referred to as the phase of *large swarms*.

The highest volume fraction tested is $\phi = 0.1$. There, very big clusters form, but have a very low propelled velocity and close to zero orientational correlation. These properties point out that, even though some orientational correlation remains due to remnants of swarming behavior, the dominant clustering mechanism is jamming

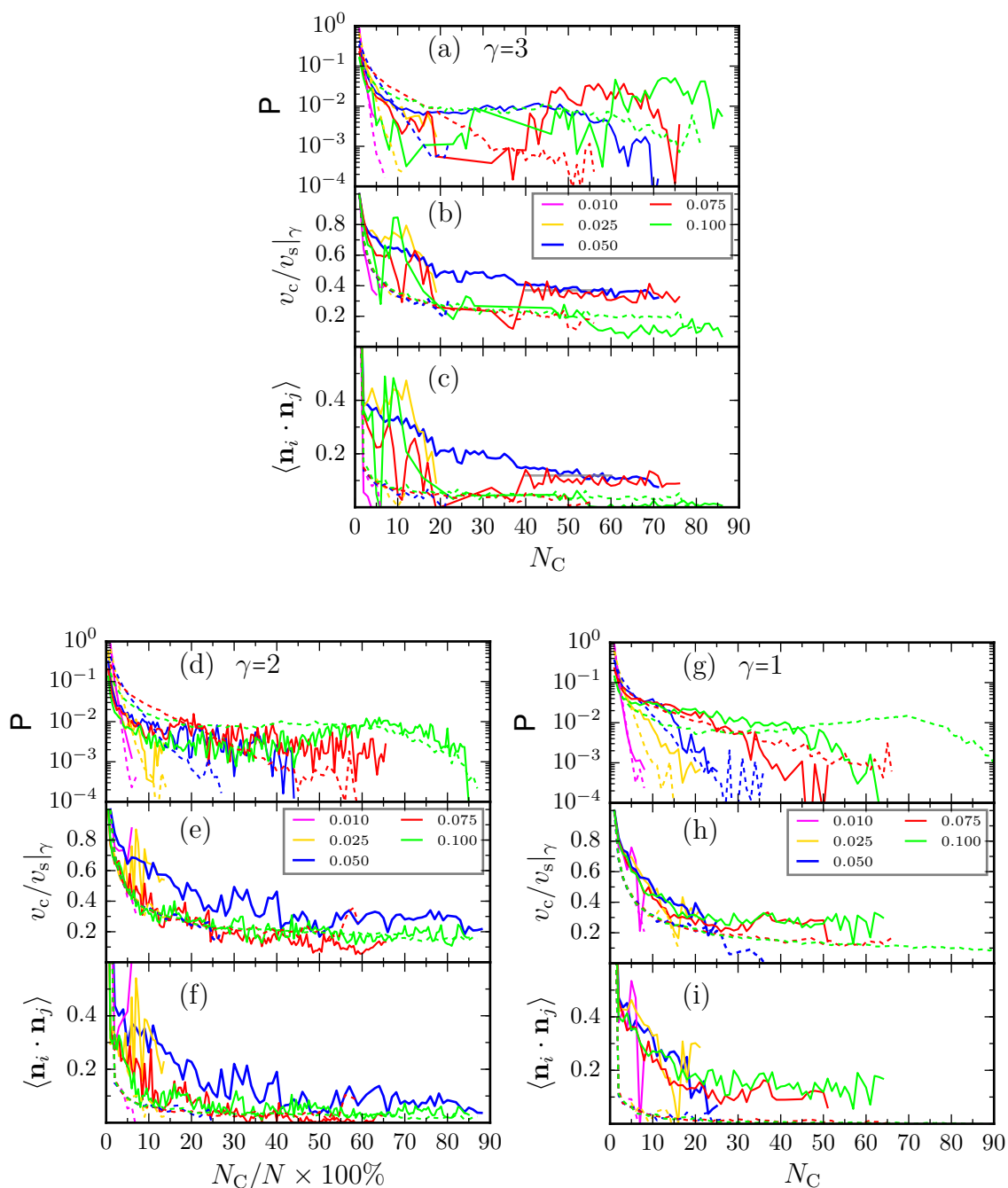


Figure 7.12: Cluster properties of ensembles of thermophobic dimers with $\gamma = 3$ (a,b,c), $\gamma = 2$ (d,e,f), and $\gamma = 1$ (g,h,i) at volume fractions $\phi = 0.01$ (pink), 0.025 (gold), 0.05 (blue), 0.075 (red) and 0.1 (green). Dashed lines show results obtained with LD. **a,d,g**) Averaged probability for a dimer to be in a cluster of size N_C . **b,e,h**) Normalized cluster velocities as a function of normalized cluster size. **c,f,i**) Orientational correlation of dimers within the same cluster as a function of the normalized cluster size. Results for $\gamma = 2$ stem from simulations using $N = 200$ dimers, and the cluster size is given as $N_C/N \times 100\%$ to facilitate comparison to the other size ratios, where $N = 100$ was used.

here and it is referred to as the *jamming* phase.

Overall, these simulation results confirm that the emergence of swarming behavior is dependent on the volume fraction. More precisely, there is a balance in between the lifetime of clusters, the probability to meet other dimers and the space and time available for each dimer to feel the hydrodynamic and phoretic influence of others. Together, these factors determine the kind of collective behavior possible. Within the volume fractions considered so far, four different phases emerge, the dilute, small swarms, large swarms, and jamming phase. Based on these, a phase diagram may be constructed and is shown in fig. 7.13a. The four phases are illustrated with snapshots of $\gamma = 3$ dimers in figs. 7.13b to 7.13e. The assignment

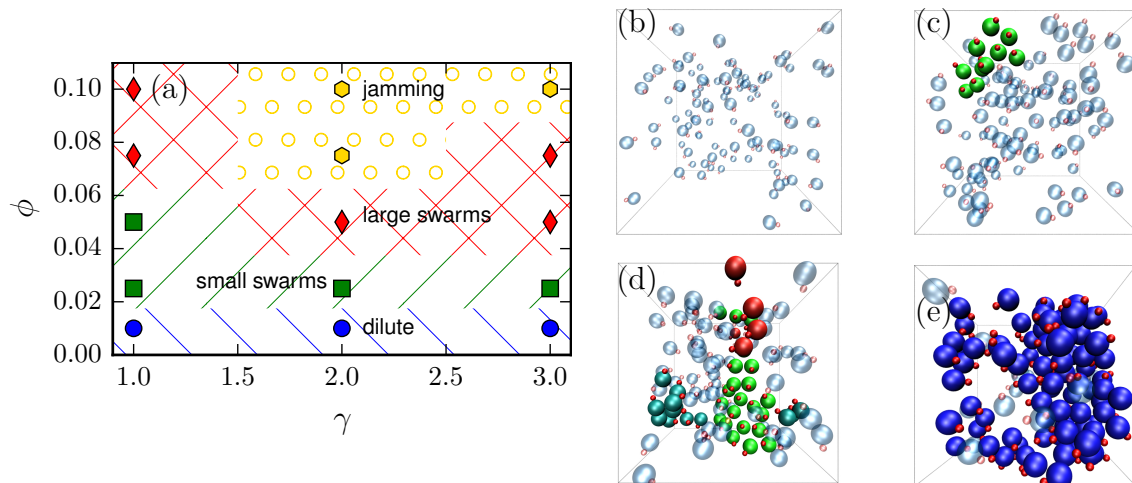


Figure 7.13: **a)** Phase diagram of thermophobic dimers as a function of bead size ratio γ and volume fraction ϕ . **b,c,d,e)** Illustrations of the dilute (**b**), small swarms (**c**), swarming (**d**) and jammed (**e**) states for dimers with $\gamma = 3$.

of phases for the asymmetric $\gamma = 2$ dimer is based on similar considerations as for the $\gamma = 3$ dimer. For the $\gamma = 2$ dimer, the self-propelled velocity $v_c = -0.0268$ is a bit faster, but close to that of the other two constructions which feature about -0.02 (see table 7.1). Its hydrodynamic interactions are similar to the $\gamma = 3$ dimer, featuring long-ranged lateral hydrodynamic attraction (c.f. fig. 4.6c and fig. 4.7c for details). Though similar, the differences lead to a shift of phase boundaries, in that the region of large swarms seems narrower, at least judging from the dataset considered. As visible in fig. 7.12f, at both $\phi = 0.075$ and $\phi = 0.1$, nearly no orientational correlation is observed for the clusters, from which follows that the jamming phase starts at lower volume fractions than that of the $\gamma = 3$ dimer. This is consistent with the observation that the lobe in the flow field leading to attractive lateral hydrodynamic interactions grows with increasing γ , such that a weaker effect is expected for smaller γ .

All results on the jamming phases are, for both the $\gamma = 3$ and the $\gamma = 2$ dimer, well accounted for by a collisional mechanism leading to jamming and a certain motility-induced attraction. This can be seen in the good agreement of MPC-MD

and LD results in fig. 7.12a to 7.11f. It follows that for asymmetric dimers at higher volume fractions, neither hydrodynamic nor phoretic effects seem to have an important influence on the collective dynamics.

This is different for the symmetric dimer with $\gamma = 1$. First, starting from low volume fractions, a dilute and a small swarms phase are observed. But at higher volume fractions of $\phi = 0.075$ and $\phi = 0.1$, i.e. the region where jamming already dominates for the $\gamma = 2$ dimer, the symmetric dimer starts swarming. Motility-induced attraction has a stronger influence on the symmetric than on the asymmetric dimer, but does not account at all for this effect. This is visible in fig. 7.12c, where it can be made out that LD simulations at higher volume fractions show zero orientational correlation, while cluster sizes, velocities as well as orientational correlation obtained in MPC-MD are well comparable to those measured for the large swarms of asymmetric dimers. That symmetric dimers show the formation of large swarms at elevated volume fractions is likely attributable to their short-ranged, laterally attractive hydrodynamic interactions. These are expected to show a more distinct influence at higher swimmer densities, when the lack of space forces the swimmers to be closer together such that short-range effects are more prominently felt. Though this alone might account for the observed behavior, an additional complication in this interpretation arises concerning the phoretic effect and its interplay with hydrodynamics. The phoretic effect is strongest for symmetric dimers, as the hot bead is largest here. It is thinkable that it provides an additional stabilization of swarms, as one dimer located between two others will be phoretically repelled by both of them, hence forced to keep its position. A future study offering a precise quantification of the interplay of hydrodynamics and phoresis will provide valuable insights into this phenomenology.

7.2.6.5 Inclusion of Depletion Effects

Up to this point, the main focus has been on studying the collective dynamics of dimeric microswimmers in a scenario as close as possible to a suspension of swimmers in an atomic/molecular fluid. Therefore, great care was taken that no depletion artifacts were present that disturb the dynamics, and it was shown that hydrodynamics and phoresis alone will lead to a dynamic swarming behavior. However, as discussed in chapter 5, the aligned formation of depleted pairs in the swimming-together (ST) bound state can be of interest, and may also be experimentally realizable, especially since inducing attractive depletion interactions in colloidal systems is a well-known and controllable procedure [89]. The depletion interaction in MPC-MD arises as numerical artifact through the ideal gas equation of state and its strength is not well-controllable. Still, it is of interest to consider what kinds of structures emerge when depletion is present, and an easy way to do so is to use a parameter region where it is present as a numeric artifact of the simulation method.

The dynamics of collective systems are different when depletion is present. Figure 7.14 shows visual representations of the structures formed in an ensemble of

1000 asymmetric, thermophobic dimers with $\gamma = 2$. This simulation uses parameters close to those of the single dimers of chapter 4, with $s_p = 4$, $s_h = 2$, $\delta_b = 0$. The inter-dimer repulsion is modeled as in chapter 5, using a standard LJ potential with $\varepsilon_D = 1$ and a range $s_p + s_h + 0.2$. With these parameters, attractive depletion interactions between pairs of dimers will be present and induce formation of ST bound states. As expected from the ST bound state, dimers attach laterally to

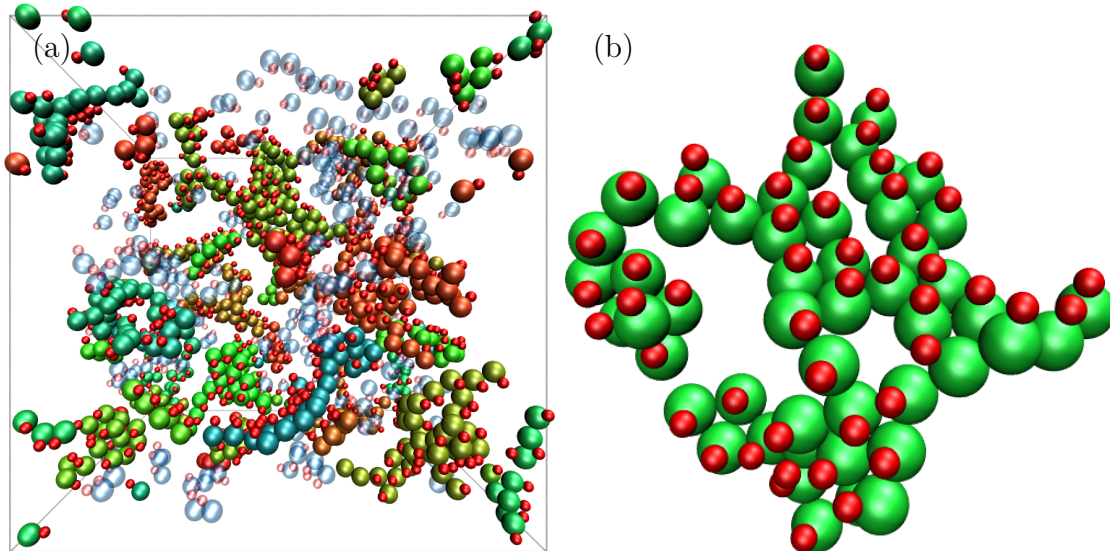


Figure 7.14: Snapshots of ensembles of $N = 1000$ thermophobic dimers of size ratio $\gamma = 2$ that feature depletion forces. Non-assembled dimers are translucent, with red heated beads and blue phoretic beads. Dimers assembled in clusters of size five or larger are solid, with red heated beads and phoretic beads colored according to cluster identity. **a)** A representation of the whole simulation box. **b)** Close-up view of a typical structure of a single swarm.

each other and form large, aligned and rather flat sheets as well as more string-like structures. The behavior is dynamic, with clusters assembling and disassembling constantly. Figure 7.15 shows a quantification of the cluster properties. These are very similar in terms of all measured properties to those observed in the undepleted case, which are also shown in the figure for comparison, even though the size ratio of the dimers' beads is different. Notably, a very similar limit on cluster size emerges, indicating that the same physical effect of increased fluid friction also limits the size of the flattened swarms in the depleted case, and no percolation takes place. However, due to the depletion interaction being stronger than pure hydrodynamic attraction, the stability of these structures is increased. The depletion interaction of the MPC-MD method is not very well controllable, especially in a complex scenario as used here which involves non-equilibrium driving forces and temperature gradients [54]. Therefore, care must be taken to draw definite conclusions from these results. However, these simulations serve as a proof-of-concept that swarming structures based on the ST state can be induced by depletion as well, and may

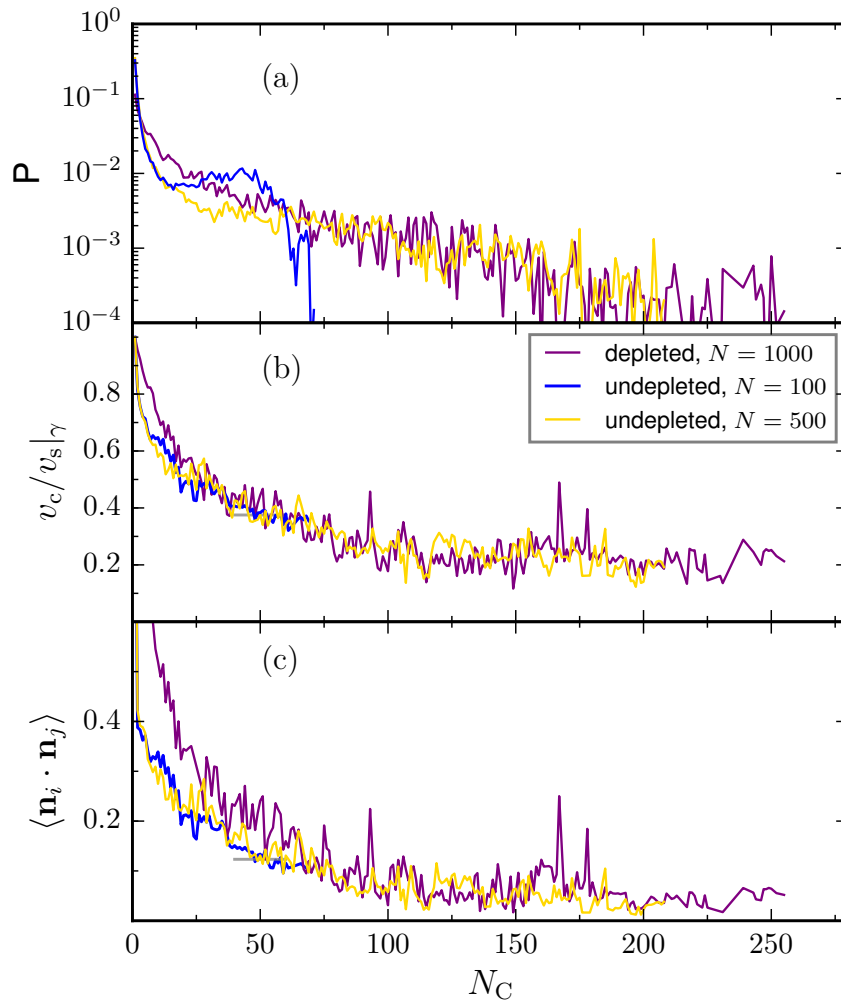


Figure 7.15: Cluster properties of ensembles of $N = 1000$ asymmetric, depleted, thermophobic dimers at volume fraction $\phi = 0.04$ featuring a size ratio of $\gamma = 2$ (purple). Also shown are the results for $N = 100$ (blue) and $N = 500$ (gold) undepleted asymmetric dimers with $\gamma = 3$ at $\phi = 0.05$. **a)** Averaged probability for a dimer to be in a cluster of size N_C . **b)** Normalized cluster velocities as a function of normalized cluster size. **c)** Orientational correlation of dimers within the same cluster as a function of the normalized cluster size.

then be more stable as compared to those relying on pure hydrodynamic attraction while showing comparable dynamics. In an extended study based on these results, it will be advisable to use a parameter region which avoids artificial depletion and induce controlled depletion forces by means of a pair-wise potential, akin to what has been considered in [96].

The major difference between employing depletion and relying on hydrodynamics to induce swarm formation in dimeric swimmers is, besides the stability of the formed clusters, what happens when the driving force is taken away by switching off

the illumination. In a non-depleted scenario, all clusters will dissolve by Brownian motion and the equilibrium distribution of a colloidal suspension will be regained after some relaxation time. But in a scenario involving depletion, all formed structures will tend to stay together when the local heating is removed, likely even more so than in case when driving forces are present as there are less fluctuations then. Without self-propulsion, they will of course not propel anymore, by eventually meet by diffusive processes and then cluster together further, likely forming a large bulk of colloidal crystal. This difference will be crucial in determining the practical use of both types of system.

7.3 Summary and Discussion

Thermophilic Dimers For thermophilic dimer swimmers, the attractive phoretic interactions dominate the collective dynamics, leading to the formation of stable unmoving aggregates. The main mechanism determining structure and behavior is that the phoretic beads are attracted by the hot beads of other dimers, becoming surrounded by as many hot beads as possible. This behavior is in some way expected from the observation that in the simulations of pairs of thermophilic dimers, phoretic and hot beads also are close together. There however, the structures are stable due to depletion interactions. When the dimer-dimer repulsion is too strong, no stable pairs form for two thermophilic dimers. This is different in a system of many thermophilic dimers. Even though no depletion is present, the dimers form stable clusters due to a multi-body effect where the phoretic propulsion force is being diminished when a phoretic bead is in close contact to several hot beads, which is inherently not possible for a low number of swimmers.

The resulting structures are solid-like, as is also the case in those formed by the mechanism of MIPS in two dimensions. In three dimensions, MIPS leads rather to liquid-like structures [8]. Coexistence with a gas-like phase is also given here, as swimmers may detach from the agglomerates through thermal fluctuations and then move freely until they are attracted to one another again. But in contrast to MIPS, solid- and not liquid-like structures form in the three-dimensional case here due to the existence of strong phoretically attractive interactions, which is a very different clustering mechanism resulting in different structures.

The degree of crystallization will depend on the strength of the phoretic attraction. Also, in contrast to MIPS as well, the reorientation time of swimmers does not play a significant role as the attachment is induced by an actual attractive interaction. Many swimmers are pointing outwards from the centers of solid-like clusters, in this sense, the (effective) attraction is working in reverse as compared to MIPS in two dimensions. Since the dimers in the clusters barely move, hydrodynamic interactions do not seem to play a role in the observed phenomenology.

Thermophobic dimers Thermophobic dimeric colloidal swimmers show a swarming behavior that is determined by their geometric construction and the resulting

phoretic and hydrodynamic behavior. It is observed that asymmetric dimers form big swarms of up to around 150 dimers for the chosen model parameters. This size and stability of such swarms will depend on a multitude of factors, such that the simulation results presented should be taken as a proof-of-concept that such collective behavior is possible, as well as provide insight into which physical effects originate it. Preliminary results at different volume fractions indicate that four distinct phases form, as a result of the balance in between hydrodynamic attraction, fluctuations and swimmer density. There is a dilute phase with dimers moving freely, a phase in which small swarms form as well as one featuring large swarms, and a jamming phase in dense systems. Likely, the swarms will be more stable at lower temperature, when thermal fluctuations are of reduced importance. Experimentally, this can be achieved also by using larger colloidal particles. The combination of phoretic repulsion with lateral hydrodynamic attraction, and to a lesser part motility-induced attraction, leads to swarming in structures with a pronounced tendency to propel as sheet-like fronts. Such behavior seems specific to these systems, and no equivalent structures were observed in either biological or synthetic active systems [5–7, 9, 20].

Though based on the results obtained here, the basic mechanism is plausible and the phenomenology clear, there are questions remaining. For one, the relative importance of short- and long-ranged hydrodynamic interactions is not easily quantifiable. It has been shown that short-range hydrodynamic interactions importantly influence the collective dynamics of colloidal swimmers [82, 86, 99]. Clusters of symmetric dimers show a pronounced increase in velocity and orientational correlation when phoresis and hydrodynamics are considered as compared to LD simulations and this can only be due to the short-rang hydrodynamic attraction. An increase in volume fraction seems to also have the effect of increasing the importance of short-ranged hydrodynamic interactions, such that in fact a phase of large swarms forms at volume fractions of symmetric dimers where some asymmetric constructions jam already. In the cases considered here, the large hot beads will lead to a slow down of swarms. This is due to the temperature field getting more uniform when many hot beads are close-by and the phoretic driving forces being thereby reduced, akin to the case of thermophilic clusters. Simulations that only consider exclusively either the phoretic effect or hydrodynamic effect may give further insight into this phenomenology. Specifically, they may answer the question if the swarm formation of symmetric dimers is stabilized by the phoretic effect. Unfortunately, for thermophoretic swimmers it is difficult to only include just one of either hydrodynamic or phoretic interactions in MPC-MD simulations, as they both rely on the fluid particles' velocities. Randomizing the fluid particles' velocities, by means of a randomized MPC collision step [108], will lead to a diminishing or eventually vanishing of the phoretic driving force, as has also been observed for diffusiophoretic swimmers [97]. A possibility could be to perform LD simulations, and within these solve numerically the Laplace equation describing the temperature field with constant-temperature boundaries at the hot beads and no-flux boundary conditions at the phoretic ones. Based on the results obtained in chapter 3, the response of a col-

loid to a temperature gradient is easily accessible for any colloid-fluid interaction potential. Then, the temperature gradients at each phoretic bead are known, from which the force can be calculated and applied. This would provide a possibility to study solely the effect of phoresis.

Depletion The addition of depletants to a suspension of dimeric swimmers, whose effect is here estimated by taking advantage of the fact that this interaction may result from MPC-MD itself, can modify the phenomenology. Interestingly, it may stabilize swarm formation, which can be of high relevance for a possible experimental realization of such systems. A major difference between depleted and non-depleted systems lies in the equilibrium state, when no illumination and propulsion are present. This will be, for colloids repelling each other, a rather uniform colloidal suspension in non-depleted systems, but a clustered state in a depleted system. Switching in between the equilibrium and the active state is easily possible by turning on and off the light source, but will then feature very different phenomenology depending on the presence of depletants.

8 Concluding Summary and Outlook

This work investigated and discussed the behavior of colloidal microswimmers driven by the thermophoretic mechanism, with a special focus on the dimeric type of construction, using hydrodynamic simulations performed with the MPC-MD method.

A microscopic hydrodynamic approach to describe the thermophoretic mechanism is developed in chapter 3, based on the general framework for phoretic mechanisms [74]. The approach describes thermophoresis in an ideal-gas-like solvent as the combination of a temperature gradient and a density gradient, resulting from the surface colloid-solvent interaction potential. These combined effects lead to a phoretic force or slip velocity, which will vary with the interaction potential and accounts for the self-propulsion of the swimmers. With it, Soret coefficients of single colloids in temperature gradients are obtained for different interaction potentials and agreement to simulation measurements is found in many cases. A linearized variant of the approach makes understandable why the Soret coefficient has a positive or negative sign, depending on the molecular interaction potential and on temperature. Some insight into the scaling of the Soret coefficient with particle size is achieved as well. However, some of the simulation results for stronger attractive potentials are not in agreement with the theoretical predictions. Some experimental results suggest a linear scaling, while others suggest a quadratic one, a discrepancy which could not be explained by the theoretical approach here. In any case, these features should be related with the density distribution around the colloid. It will be of interest to see if the framework can be extended further to also include other equations of state, since these may have a significant influence on the density distribution and could provide further insight into this phenomenology.

Single dimeric and Janus colloidal swimmers are studied in chapter 4. The Janus swimmer does show a variation in hydrodynamic short range interactions as a function of its coverage with active material, quantified in terms of the coating angle. A rather precise control of the coating angle is possible also experimentally [109], and the importance of short-ranged hydrodynamics has already been observed in several studies [82, 86, 99]. Therefore, the dynamics of ensembles of Janus swimmers are expected to also be influenced by the choice of coating angle, as will be the behavior when confining walls are present.

The dimeric swimmers are found to show intriguing hydrodynamic behavior in terms of a lateral attraction and repulsion that changes as a function of their geometric construction. A linearized and simplified version of the theoretical description of thermophoresis is employed to describe these features, capturing the qualitative features of swimming velocity and flow fields as a function of bead size

ratio quite well. The comparison to chemically driven swimmers leads to the conclusion that the main features of colloidal phoretic swimmers do not depend on the type of phoretic mechanism employed for propulsion. This is confirmed in chapter 5, in which pairs of dimeric swimmers are studied. The thermophilic dimers mainly show the same behavior as already observed for phoretically attractive, chemical dimers [77]. For thermophobic dimers, a very different behavior is observed, in which depletion-induced attraction leads, for a wide range of parameters, to a bound state that features the two dimers propelling together in an aligned fashion, the ST bound state. Since depletion is commonly used in experimental systems to induce attractive interactions, such a state is likely to be reproducible in real systems.

In order to study the behavior of ensembles of these microswimmers, a reexamination of depletion forces that can emerge as a simulation artifact in MPC-MD is undertaken in chapter 6. This is of special relevance when attractive interaction potentials are used, as for these artificial depletion is very strong. The introduction of displacements into the interaction potentials reduces the issue, allowing to perform simulations employing such potentials without suffering artificial depletion. Overall, the discussion provides a basis to choose a parameter regime in MPC-MD simulations, independent of the precise system and interaction potential, in which artificial depletion is avoided, while at the same time capturing the relevant short-range interactions, like hydrodynamics and phoresis.

Based on the observations concerning single swimmer dynamics, ensembles of thermophoretic dimers are studied in chapter 7. It is found that for thermophilic dimers, the phoretic attraction leads to long-time stable crystalline structures. Thermophobic asymmetric dimers combine lateral hydrodynamic attraction with axial phoretic repulsion, which leads at intermediate volume fractions to a unique kind of dynamic swarming behavior in which many dimers propel in fronts with a pronounced tendency to be planarly aligned. It is a question of general interest how and to what extent hydrodynamic interactions play a role in systems of colloidal particles. The swarming behavior of asymmetric thermophobic dimers provides a proof-of-concept that hydrodynamic interactions can influence collective dynamics not only quantitatively, but also lead to new phenomenology. That there are, at elevated volume fractions, swarming phases also observed for symmetric dimers, which feature only short-ranged hydrodynamic attraction, highlights the importance of short-range hydrodynamic effects. For a test case involving depletion forces, a very similar swarming behavior is observed for asymmetric dimers as well in the presence of depletion, which is found to enhance the effect, stabilizing the swarms through the additional attraction.

Based on the simulation studies performed here, the different kinds of collective behavior observed may find applications in experimental systems, in particular as their behavior is tunable and switchable. Specifically, these systems are tunable in two ways. One is to turn on and off or regulating the intensity of the light source providing the heating of the hot beads and thereby switching in between self-propelled and Brownian systems. The other is to change the sign of the Soret

coefficient by changing the average temperature, or another relevant parameter such as pressure or a solvent property like salt concentration, depending on the system. As evident from the experimental results shown in fig. 1.5, there are colloids that change their behavior from thermophilic to thermophobic within the easily accessible temperature range of 0 and 40°C.

The crystallization of thermophilic dimers is induced not by depletion or jamming, but by phoretic attraction, which presents in itself a means to induce reversible colloidal crystallization by switching on and off the light source. Any structure formed will, when no depletion is involved, dissolve when the illumination is turned off and after some relaxation time reproduce the equilibrium distribution of unpropelled swimmers. As the particles are self-propelled, the crystal formation is expected to happen quite quickly, and also at low volume fractions. Dissolution will likely take longer, as it relies on Brownian motion. This would be different when one, instead of turning off the light source, reverses the Soret coefficient by changing the average temperature. It might be possible to switch the behavior of ensembles of thermophoretic dimers from non-moving clusters to swarm formation also in experiments. Due to the system being active, this process should happen quite fast in both directions.

The front-like swarming behavior of thermophobic dimers presents a unique kind of dynamic structure formation. By itself, it might for example be useful in cleaning and substance removal applications, since these formations, as opposed to vortices or crystalline clusters, do constantly move and span up area more efficiently than many other formations. With appropriate boundary conditions, they might cover up cross sections of microfluidic channels, dragging immersed and unwanted particles along.

Further tunability of such systems could be achieved by the introduction of depletants. Especially when a constantly moving and stable formation is desired, adding depletants to thermophobic dimers could provide a means to achieve this. However, this would mean that no state akin to a suspension of unpropelled colloids without depletion can be regained by Brownian motion, as the depletion forces will likely hold any structure that built up together and rather lead to growth by attaching further colloids than to a dissolution. Still, also in the presence of depletants, a switch of the Soret coefficient should switch from swarming to crystalline clusters, given that the phoretic repulsion in the thermophobic state is strong enough as compared to depletion.

In general, the fact that thermophoretic microswimmers are tunable systems which can be made to switch in between dense states when clustered and extended states when swarming, or, depending on boundary conditions, even percolated states, suggests that they might also find application in systems where such properties could be used to change in between conducting and non-conducting states. The unique phenomenology of front-like swarming may offer new possibilities in applications of active matter systems, for example in the design of microfluidic devices or bio-compatible micromotors.

Bibliography

- [1] H. Machemer, “Ciliary activity and origin of metachrony in paramecium: effects of increased viscosity”, *J. Exp. Biol.* **1972**, *57*, 239, eprint: <http://jeb.biologists.org/content/57/1/239.full.pdf>.
- [2] J. Cosson, P. Huitorel, C. Gagnon, “How Spermatozoa Come to Be Confined to Surfaces”, *Cell Motil. Cytoskeleton* **2003**, *54*, 56, DOI [10.1002/cm.10085](https://doi.org/10.1002/cm.10085).
- [3] L. Turner, W. S. Ryu, H. C. Berg, “Real-Time Imaging of Fluorescent Flagellar Filaments”, *J. Bacteriol.* **2000**, *182*, 2793, DOI [10.1128/JB.182.10.2793-2801.2000](https://doi.org/10.1128/JB.182.10.2793-2801.2000).
- [4] J. L. Moran, J. D. Posner, “Phoretic Self-Propulsion”, *Annu. Rev. Fluid Mech.* **2017**, *49*, 511–540, DOI [10.1146/annurev-fluid-122414-034456](https://doi.org/10.1146/annurev-fluid-122414-034456).
- [5] T. Vicsek, A. Zafeiris, “Collective motion”, *Physics Reports* **2012**, *517*, Collective motion, 71–140, DOI [10.1016/j.physrep.2012.03.004](https://doi.org/10.1016/j.physrep.2012.03.004).
- [6] P. Romanczuk, M. Bär, W. Ebeling, B. Lindner, L. Schimansky-Geier, “Active Brownian Particles From Individual to Collective Stochastic Dynamics”, *Eur. Phys. J. Special Topics* **2012**, *202*, 1–162, DOI [10.1140/epjst/e2012-01529-y](https://doi.org/10.1140/epjst/e2012-01529-y).
- [7] J. Elgeti, R. G. Winkler, G. Gompper, “Physics of microswimmers - single particle motion and collective behavior: a review”, *Rep. Prog. Phys.* **2015**, *78*, 056601, DOI [10.1088/0034-4885/78/5/056601](https://doi.org/10.1088/0034-4885/78/5/056601).
- [8] A. Wysocki, R. G. Winkler, G. Gompper, “Cooperative motion of active Brownian spheres in three-dimensional dense suspensions”, *EPL* **2014**, *105*, 48004, DOI [10.1209/0295-5075/105/48004](https://doi.org/10.1209/0295-5075/105/48004).
- [9] A. Zöttl, H. Stark, “Emergent behavior in active colloids”, *J. Phys.: Condens. Matter* **2016**, *28*, 253001, DOI [10.1088/0953-8984/28/25/253001](https://doi.org/10.1088/0953-8984/28/25/253001).
- [10] I. Buttinoni, J. Bialké, F. Kümmel, H. Löwen, C. Bechinger, T. Speck, “Dynamical Clustering and Phase Separation in Suspensions of Self-Propelled Colloidal Particles”, *Phys. Rev. Lett.* **2013**, *110*, 238301, DOI [10.1103/PhysRevLett.110.238301](https://doi.org/10.1103/PhysRevLett.110.238301).
- [11] R. Dreyfus, J. Baudry, M. L. Roper, M. Fermigier, H. A. Stone, J. Bibette, “Microscopic artificial swimmers”, *Nature* **2005**, *437*, 862–865, DOI [10.1038/nature04090](https://doi.org/10.1038/nature04090).

- [12] W. F. Paxton, K. C. Kistler, C. C. Olmeda, A. Sen, S. K. St. Angelo, Y. Cao, T. E. Mallouk, P. E. Lammert, V. H. Crespi, “Catalytic Nanomotors: Autonomous Movement of Striped Nanorods”, *J. Am. Chem. Soc.* **2004**, *126*, 13424–13431, DOI [10.1021/ja047697z](https://doi.org/10.1021/ja047697z).
- [13] J. R. Howse, R. A. L. Jones, A. J. Ryan, T. Gough, R. Vafabakhsh, R. Golestanian, “Self-Motile Colloidal Particles: From Directed Propulsion to Random Walk”, *Phys. Rev. Lett.* **2007**, *99*, 048102, DOI [10.1103/PhysRevLett.99.048102](https://doi.org/10.1103/PhysRevLett.99.048102).
- [14] R. Golestanian, T. B. Liverpool, A. Ajdari, “Propulsion of a Molecular Machine by Asymmetric Distribution of Reaction Products”, *Phys. Rev. Lett.* **2005**, *94*, 220801, DOI [10.1103/PhysRevLett.94.220801](https://doi.org/10.1103/PhysRevLett.94.220801).
- [15] J. Palacci, C. Cottin-Bizonne, C. Ybert, L. Bocquet, “Sedimentation and Effective Temperature of Active Colloidal Suspensions”, *Phys. Rev. Lett.* **2010**, *105*, 088304, DOI [10.1103/PhysRevLett.105.088304](https://doi.org/10.1103/PhysRevLett.105.088304).
- [16] R. Kapral, “Perspective: Nanomotors without moving parts that propel themselves in solution”, *J. Chem. Phys.* **2013**, *138*, 020901, DOI [10.1063/1.4773981](https://doi.org/10.1063/1.4773981).
- [17] A. T. Brown, W. C. K. Poon, C. Holm, J. de Graaf, “Ionic screening and dissociation are crucial for understanding chemical self-propulsion in polar solvents”, *Soft Matter* **2017**, *13*, 1200–1222, DOI [10.1039/C6SM01867J](https://doi.org/10.1039/C6SM01867J).
- [18] G. Rückner, R. Kapral, “Chemically Powered Nanodimers”, *Phys. Rev. Lett.* **2007**, *98*, 150603, DOI [10.1103/PhysRevLett.98.150603](https://doi.org/10.1103/PhysRevLett.98.150603).
- [19] L. F. Valadares, Y.-G. Tao, N. S. Zacharia, V. Kitaev, F. Galembeck, R. Kapral, G. A. Ozin, “Catalytic Nanomotors: Self-Propelled Sphere Dimers”, *Small* **2010**, *6*, 565–572, DOI [10.1002/smll.200901976](https://doi.org/10.1002/smll.200901976).
- [20] C. Bechinger, R. Di Leonardo, H. Löwen, C. Reichhardt, G. Volpe, G. Volpe, “Active particles in complex and crowded environments”, *Rev. Mod. Phys.* **2016**, *88*, 045006, DOI [10.1103/RevModPhys.88.045006](https://doi.org/10.1103/RevModPhys.88.045006).
- [21] S. Wiegand, “Thermal diffusion in liquid mixtures and polymer solutions”, *Journal of Physics: Condensed Matter* **2004**, *16*, R357, DOI [10.1088/0953-8984/16/10/R02](https://doi.org/10.1088/0953-8984/16/10/R02).
- [22] W. Poon in *Physics of Complex Colloids*, (Eds.: C. Bechinger, F. Sciortino, P. Zihlerl), Proceedings of the International School of Physics "Enrico Fermi", IOS Press Ebooks, **2013**, Chapter From Clarkia to Escherichia and Janus: The physics of natural and synthetic active colloids, pp. 317–386, DOI [10.3254/978-1-61499-278-3-317](https://doi.org/10.3254/978-1-61499-278-3-317).
- [23] H.-R. Jiang, N. Yoshinaga, M. Sano, “Active Motion of a Janus Particle by Self-Thermophoresis in a Defocused Laser Beam”, *Phys. Rev. Lett.* **2010**, *105*, 268302, DOI [10.1103/PhysRevLett.105.268302](https://doi.org/10.1103/PhysRevLett.105.268302).

- [24] M. Yang, M. Ripoll, “Simulations of thermophoretic nanoswimmers”, *Phys. Rev. E* **2011**, *84*, 061401, DOI [10.1103/PhysRevE.84.061401](https://doi.org/10.1103/PhysRevE.84.061401).
- [25] M. Yang, A. Wysocki, M. Ripoll, “Hydrodynamic simulations of self-phoretic microswimmers”, *Soft Matter* **2014**, *10*, 6208–6218, DOI [10.1039/C4SM00621F](https://doi.org/10.1039/C4SM00621F).
- [26] A. J. Chorin, J. E. Marsden, *A Mathematical Introduction to Fluid Mechanics*, Springer-Verlag New York, Inc, **2000**.
- [27] J. Dhont, *An Introduction to Dynamics of Colloids*, (Eds.: D. Möbius, R. Miller), Elsevier Science B.V., **1996**.
- [28] R. Piazza, A. Parola, “Thermophoresis in colloidal suspensions”, *J. Phys.: Condens. Matter* **2008**, *20*, 153102, DOI [10.1088/0953-8984/20/15/153102](https://doi.org/10.1088/0953-8984/20/15/153102).
- [29] N. Van Kampen, “Diffusion in inhomogeneous media”, *Journal of Physics and Chemistry of Solids* **1988**, *49*, 673–677, DOI [10.1016/0022-3697\(88\)90199-0](https://doi.org/10.1016/0022-3697(88)90199-0).
- [30] M. Yang, M. Ripoll, “Drift velocity in non-isothermal inhomogeneous systems”, *J. Chem. Phys.* **2012**, *136*, 204508, DOI [10.1063/1.4723685](https://doi.org/10.1063/1.4723685).
- [31] U. Titulaer, “A systematic solution procedure for the Fokker-Planck equation of a Brownian particle in the high-friction case”, *Physica A: Statistical Mechanics and its Applications* **1978**, *91*, 321–344, DOI [10.1016/0378-4371\(78\)90182-6](https://doi.org/10.1016/0378-4371(78)90182-6).
- [32] F. Römer, Z. Wang, S. Wiegand, F. Bresme, “Alkali Halide Solutions under Thermal Gradients: Soret Coefficients and Heat Transfer Mechanisms”, *J. Phys. Chem. B* **2013**, *117*, 8209, DOI [10.1021/jp403862x](https://doi.org/10.1021/jp403862x).
- [33] S. de Groot, P. Mazur, *Non-Equilibrium Thermodynamics*, Dover Publications, inc., New York, **1962**.
- [34] M. Zhang, PhD thesis, Technische Universität Darmstadt, **2006**.
- [35] D. Lüsebrink, M. Yang, M. Ripoll, “Thermophoresis of colloids by mesoscale simulations”, *J. Phys.: Condens. Matter* **2012**, *24*, 284132, DOI [10.1088/0953-8984/24/28/284132](https://doi.org/10.1088/0953-8984/24/28/284132).
- [36] M. Braibanti, D. Vigolo, R. Piazza, “Does Thermophoretic Mobility Depend on Particle Size?”, *Phys. Rev. Lett.* **2008**, *100*, 108303, DOI [10.1103/PhysRevLett.100.108303](https://doi.org/10.1103/PhysRevLett.100.108303).
- [37] S. Duhr, D. Braun, “Thermophoretic Depletion Follows Boltzmann Distribution”, *Phys. Rev. Lett.* **2006**, *96*, 168301, DOI [10.1103/PhysRevLett.96.168301](https://doi.org/10.1103/PhysRevLett.96.168301).
- [38] S. A. Putnam, D. G. Cahill, G. C. L. Wong, “Temperature Dependence of Thermodiffusion in Aqueous Suspensions of Charged Nanoparticles”, *Langmuir* **2007**, *23*, PMID: 17655335, 9221–9228, DOI [10.1021/la700489e](https://doi.org/10.1021/la700489e).

- [39] D. Vigolo, G. Brambilla, R. Piazza, “Thermophoresis of microemulsion droplets: Size dependence of the Soret effect”, *Phys. Rev. E* **2007**, *75*, 040401, DOI [10.1103/PhysRevE.75.040401](https://doi.org/10.1103/PhysRevE.75.040401).
- [40] Y. Kishikawa, S. Wiegand, R. f. Kita, “Temperature Dependence of Soret Coefficient in Aqueous and Nonaqueous Solutions of Pullulan”, *Biomacromolecules* **2010**, *11*, 740–747, DOI [10.1021/bm9013149](https://doi.org/10.1021/bm9013149), eprint: <http://dx.doi.org/10.1021/bm9013149>.
- [41] D. Lüsebrink, PhD thesis, Universität zu Köln, **2011**.
- [42] A. Würger, “Thermal non-equilibrium transport in colloids”, *Rep. Prog. Phys.* **2010**, *73*, 126601, DOI [10.1088/0034-4885/73/12/126601](https://doi.org/10.1088/0034-4885/73/12/126601).
- [43] A. Malevanets, R. Kapral, “Mesoscopic model for solvent dynamics”, *J. Chem. Phys.* **1999**, *110*, 8605–8613, DOI [10.1063/1.478857](https://doi.org/10.1063/1.478857).
- [44] G. Gompper, T. Ihle, D. M. Kroll, R. G. Winkler in *Advanced Computer Simulation Approaches for Soft Matter Sciences III*, (Eds.: C. Holm, K. Kremer), Springer Berlin Heidelberg, Berlin, Heidelberg, **2009**, Chapter Multi-Particle Collision Dynamics: A Particle-Based Mesoscale Simulation Approach to the Hydrodynamics of Complex Fluids, pp. 1–87, DOI [10.1007/978-3-540-87706-6_1](https://doi.org/10.1007/978-3-540-87706-6_1).
- [45] M. P. Allen, D. J. Tildesley, *Computer Simulation of Liquids*, Clarendon Press, New York, NY, USA, **1989**.
- [46] D. Frenkel, B. Smit, *Understanding Molecular Simulation*, 2nd ed., Academic Press, Inc., Orlando, FL, USA, **2001**.
- [47] T. Schlick, *Molecular modeling and simulation: an interdisciplinary guide*, Springer Science+Business Media New York, **2002**, DOI [10.1007/978-0-387-22464-0](https://doi.org/10.1007/978-0-387-22464-0).
- [48] R. L. Davidchack, R. Handel, M. V. Tretyakov, “Langevin thermostat for rigid body dynamics”, *The Journal of Chemical Physics* **2009**, *130*, 234101, DOI [10.1063/1.3149788](https://doi.org/10.1063/1.3149788).
- [49] J. F. Brady, G. Bossis, “Stokesian Dynamics”, *Ann. Rev. Fluid Mech.* **1988**, *20*, 111, DOI [10.1146/annurev.fl.20.010188.000551](https://doi.org/10.1146/annurev.fl.20.010188.000551).
- [50] A. Satoh, *Introduction to Practice of Molecular Simulation*, Elsevier Inc., **2011**.
- [51] T. Ihle, D. M. Kroll, “Stochastic rotation dynamics: A Galilean-invariant mesoscopic model for fluid flow”, *Phys. Rev. E* **2001**, *63*, 020201, DOI [10.1103/PhysRevE.63.020201](https://doi.org/10.1103/PhysRevE.63.020201).
- [52] Y. Hashimoto, Y. Chen, H. Ohashi, “Immiscible real-coded lattice gas”, *Computer Physics Communications* **2000**, *129*, 56, DOI [10.1016/S0010-4655\(00\)00092-8](https://doi.org/10.1016/S0010-4655(00)00092-8).

- [53] M. K. Petersen, J. B. Lechman, S. J. Plimpton, G. S. Grest, P. J. in 't Veld, P. R. Schunk, "Mesoscale hydrodynamics via stochastic rotation dynamics: Comparison with Lennard-Jones fluid", *J. Chem. Phys.* **2010**, *132*, 174106, DOI [10.1063/1.3419070](https://doi.org/10.1063/1.3419070).
- [54] J. T. Padding, A. A. Louis, "Hydrodynamic interactions and Brownian forces in colloidal suspensions: Coarse-graining over time and length scales", *Phys. Rev. E* **2006**, *74*, 031402, DOI [10.1103/PhysRevE.74.031402](https://doi.org/10.1103/PhysRevE.74.031402).
- [55] M. Yang, M. Theers, J. Hu, G. Gompper, R. G. Winkler, M. Ripoll, "Effect of angular momentum conservation on hydrodynamic simulations of colloids", *Phys. Rev. E* **2015**, *92*, 013301, DOI [10.1103/PhysRevE.92.013301](https://doi.org/10.1103/PhysRevE.92.013301).
- [56] E. Allahyarov, G. Gompper, "Mesoscopic solvent simulations: Multiparticle-collision dynamics of three-dimensional flows", *Phys. Rev. E* **2002**, *66*, 036702, DOI [10.1103/PhysRevE.66.036702](https://doi.org/10.1103/PhysRevE.66.036702).
- [57] T. Ihle, D. M. Kroll, "Stochastic rotation dynamics. I. Formalism, Galilean invariance, and Green-Kubo relations", *Phys. Rev. E* **2003**, *67*, 066705, DOI [10.1103/PhysRevE.67.066705](https://doi.org/10.1103/PhysRevE.67.066705).
- [58] I. O. Götze, H. Noguchi, G. Gompper, "Relevance of angular momentum conservation in mesoscale hydrodynamics simulations", *Phys. Rev. E* **2007**, *76*, 046705, DOI [10.1103/PhysRevE.76.046705](https://doi.org/10.1103/PhysRevE.76.046705).
- [59] H. Noguchi, N. Kikuchi, G. Gompper, "Particle-based mesoscale hydrodynamic techniques", *EPL* **2007**, *78*, 10005.
- [60] D. Lüsebrink, M. Ripoll, "Temperature inhomogeneities simulated with multiparticle-collision dynamics", *J. Chem. Phys.* **2012**, *136*, 084106, DOI [10.1063/1.3687168](https://doi.org/10.1063/1.3687168).
- [61] A. Lamura, G. Gompper, T. Ihle, D. M. Kroll, "Multi-particle collision dynamics: Flow around a circular and a square cylinder", *EPL* **2001**, *56*, 319, DOI [10.1209/epl/i2001-00522-9](https://doi.org/10.1209/epl/i2001-00522-9).
- [62] F. Müller-Plathe, "A simple nonequilibrium molecular dynamics method for calculating the thermal conductivity", *J. Chem. Phys.* **1997**, *106*, 6082–6085, DOI [10.1063/1.473271](https://doi.org/10.1063/1.473271).
- [63] M. Ripoll, R. G. Winkler, G. Gompper, "Star Polymers in Shear Flow", *Phys. Rev. Lett.* **2006**, *96*, 188302, DOI [10.1103/PhysRevLett.96.188302](https://doi.org/10.1103/PhysRevLett.96.188302).
- [64] A. Malevanets, R. Kapral, "Solute molecular dynamics in a mesoscale solvent", *J. Chem. Phys.* **2000**, *112*, 7260–7269, DOI [10.1063/1.481289](https://doi.org/10.1063/1.481289).
- [65] T. Ihle, E. Tüzel, D. M. Kroll, "Resummed Green-Kubo relations for a fluctuating fluid-particle model", *Phys. Rev. E* **2004**, *70*, 035701, DOI [10.1103/PhysRevE.70.035701](https://doi.org/10.1103/PhysRevE.70.035701).
- [66] T. Ihle, E. Tüzel, D. M. Kroll, "Equilibrium calculation of transport coefficients for a fluid-particle model", *Phys. Rev. E* **2005**, *72*, 046707, DOI [10.1103/PhysRevE.72.046707](https://doi.org/10.1103/PhysRevE.72.046707).

- [67] M. Ripoll, K. Mussawisade, R. G. Winkler, G. Gompper, “Dynamic regimes of fluids simulated by multiparticle-collision dynamics”, *Phys. Rev. E* **2005**, *72*, 016701, DOI [10.1103/PhysRevE.72.016701](https://doi.org/10.1103/PhysRevE.72.016701).
- [68] M. Yang, M. Ripoll, “Thermophoretically induced flow field around a colloidal particle”, *Soft Matter* **2013**, *9*, 4661–4671, DOI [10.1039/C3SM27949A](https://doi.org/10.1039/C3SM27949A).
- [69] K. Mussawisade, M. Ripoll, R. G. Winkler, G. Gompper, “Dynamics of polymers in a particle-based mesoscopic solvent”, *J. Chem. Phys.* **2005**, *123*, 144905, DOI [10.1063/1.2041527](https://doi.org/10.1063/1.2041527).
- [70] J. Elgeti, G. Gompper, “Wall accumulation of self-propelled spheres”, *EPL* **2013**, *101*, 48003, DOI [10.1209/0295-5075/101/48003](https://doi.org/10.1209/0295-5075/101/48003).
- [71] J. C. Dixon, *The Shock Absorber Handbook*, 2nd ed., ISBN: 978-0-470-51020-9, John Wiley & Sons, **2007**.
- [72] S. Plimpton, “Fast Parallel Algorithms for Short-Range Molecular Dynamics”, *J. Comput. Phys.* **1995**, *117*, 1–19, DOI [10.1006/jcph.1995.1039](https://doi.org/10.1006/jcph.1995.1039).
- [73] Jülich Supercomputing Centre, “JURECA: General-purpose supercomputer at Jülich Supercomputing Centre”, *Journal of large-scale research facilities* **2016**, *2*, A62, DOI [10.17815/jlsrf-2-121](https://doi.org/10.17815/jlsrf-2-121).
- [74] J. L. Anderson, “Colloid Transport by Interfacial Forces”, *Annu. Rev. Fluid Mech.* **1989**, *21*, 61–99, DOI [10.1146/annurev.fl.21.010189.000425](https://doi.org/10.1146/annurev.fl.21.010189.000425).
- [75] J. L. Anderson, D. C. Prieve, “Diffusiophoresis: Migration of Colloidal Particles in Gradients of Solute Concentration”, *Separation and Purification Methods* **1984**, *13*, 67–103, DOI [10.1080/03602548408068407](https://doi.org/10.1080/03602548408068407).
- [76] S. Y. Reigh, R. Kapral, “Catalytic dimer nanomotors: continuum theory and microscopic dynamics”, *Soft Matter* **2015**, *11*, 3149–3158, DOI [10.1039/C4SM02857K](https://doi.org/10.1039/C4SM02857K).
- [77] S. Thakur, R. Kapral, “Self-propelled nanodimer bound state pairs”, *J. Chem. Phys.* **2010**, *133*, 204505, DOI [10.1063/1.3506859](https://doi.org/10.1063/1.3506859).
- [78] M.-J. Huang, J. Schofield, R. Kapral, “A microscopic model for chemically-powered Janus motors”, *Soft Matter* **2016**, *12*, 5581–5589, DOI [10.1039/C6SM00830E](https://doi.org/10.1039/C6SM00830E).
- [79] S. Thakur, R. Kapral, “Collective dynamics of self-propelled sphere-dimer motors”, *Phys. Rev. E* **2012**, *85*, 026121, DOI [10.1103/PhysRevE.85.026121](https://doi.org/10.1103/PhysRevE.85.026121).
- [80] P. M. Morse, H. Feshbach, *Methods of Theoretical Physics - Part II*, 2nd ed., McGraw-Hill Book Company, Inc., **1953**.
- [81] I. O. Götze, G. Gompper, “Mesoscale simulations of hydrodynamic squirmer interactions”, *Phys. Rev. E* **2010**, *82*, 041921, DOI [10.1103/PhysRevE.82.041921](https://doi.org/10.1103/PhysRevE.82.041921).

- [82] A. Zöttl, H. Stark, “Hydrodynamics Determines Collective Motion and Phase Behavior of Active Colloids in Quasi-Two-Dimensional Confinement”, *Phys. Rev. Lett.* **2014**, *112*, 118101, DOI [10.1103/PhysRevLett.112.118101](https://doi.org/10.1103/PhysRevLett.112.118101).
- [83] K. Kroy, D. Chakraborty, F. Cichos, “Hot microswimmers”, *Eur. Phys. J Special Topics* **2016**, *225*, 2207–2225, DOI [10.1140/epjst/e2016-60098-6](https://doi.org/10.1140/epjst/e2016-60098-6).
- [84] D. A. Fedosov, A. Sengupta, G. Gompper, “Effect of fluid-colloid interactions on the mobility of a thermophoretic microswimmer in non-ideal fluids”, **2015**, DOI [10.1039/c5sm01364j](https://doi.org/10.1039/c5sm01364j).
- [85] P. de Buyl, R. Kapral, “Phoretic self-propulsion: a mesoscopic description of reaction dynamics that powers motion”, *Nanoscale* **2013**, *5*, 1337–1344, DOI [10.1039/C2NR33711H](https://doi.org/10.1039/C2NR33711H).
- [86] J.-B. Delfau, J. Molina, M. Sano, “Collective behavior of strongly confined suspensions of squirmers”, *EPL* **2016**, *114*, 24001, DOI [10.1209/0295-5075/114/24001](https://doi.org/10.1209/0295-5075/114/24001).
- [87] T. Bickel, A. Majee, A. Würger, “Flow pattern in the vicinity of self-propelling hot Janus particles”, *Phys. Rev. E* **2013**, *88*, 012301, DOI [10.1103/PhysRevE.88.012301](https://doi.org/10.1103/PhysRevE.88.012301).
- [88] M. Yang, M. Ripoll, “Thermoosmotic microfluidics”, *Soft Matter* **2016**, *12*, 8564–8573, DOI [10.1039/C6SM01692H](https://doi.org/10.1039/C6SM01692H).
- [89] H. N. W. Lekkerkerker, R. Tuinier, *Colloids and the Depletion Interaction*, (Eds.: W. Beiglböck, J. Ehlers, K. Hepp, H. Weidenmüller), Springer Science+Business Media B.V., **2011**, DOI [10.1007/978-94-007-1223-2](https://doi.org/10.1007/978-94-007-1223-2).
- [90] T. N. Shendruk, M. Bertrand, J. L. Harden, G. W. Slater, H. W. de Haan, “Coarse-grained molecular dynamics simulations of depletion-induced interactions for soft matter systems”, *J. Chem. Phys.* **2014**, *141*, DOI [10.1063/1.4903992](https://doi.org/10.1063/1.4903992).
- [91] M. Ripoll, P. Holmqvist, R. G. Winkler, G. Gompper, J. K. G. Dhont, M. P. Lettinga, “Attractive Colloidal Rods in Shear Flow”, *Phys. Rev. Lett.* **2008**, *101*, 168302, DOI [10.1103/PhysRevLett.101.168302](https://doi.org/10.1103/PhysRevLett.101.168302).
- [92] Z. Dogic, S. Fraden in *Soft Matter, Volume 2: Complex Colloidal Suspensions*, (Eds.: G. Gompper, M. Schick), Wiley-VCH Verlag GmbH & Co. KGaA, Weinheim, Germany, **2005**, Chapter Phase behavior of rod-like viruses and virus-sphere mixtures, DOI [10.1002/9783527617067.ch1](https://doi.org/10.1002/9783527617067.ch1).
- [93] A. Dinsmore, P. Warren, W. Poon, A. Yodh, “Fluid-solid transitions on walls in binary hard-sphere mixtures”, *Europhys. Lett.* **1997**, *40*, 337.
- [94] S. Asakura, F. Oosawa, “On Interaction between Two Bodies Immersed in a Solution of Macromolecules”, *J. Chem. Phys.* **1954**, *22*, 1255, DOI [10.1063/1.1740347](https://doi.org/10.1063/1.1740347).

- [95] G. Cinacchi, Y. Martínez-Ratón, L. Mederos, G. Navascués, A. Tani, E. Velasco, “Large attractive depletion interactions in soft repulsive–sphere binary mixtures”, *J. Chem. Phys.* **2007**, *127*, DOI [10.1063/1.2804330](https://doi.org/10.1063/1.2804330).
- [96] J. K. Whitmer, E. Luijten, “Influence of Hydrodynamics on Cluster Formation in Colloid-Polymer Mixtures”, *J. Phys. Chem. B* **2011**, *115*, 7294–7300, DOI [10.1021/jp111388m](https://doi.org/10.1021/jp111388m).
- [97] P. H. Colberg, R. Kapral, “Many-body dynamics of chemically-propelled nanomotors”, **2017**, arXiv: [1703.03034v1](https://arxiv.org/abs/1703.03034v1).
- [98] M. E. Cates, J. Tailleur, “Motility-Induced Phase Separation”, *Annu. Rev. Condens. Matter Phys.* **2015**, *6*, 219–244, DOI [10.1146/annurev-commatphys-031214-014710](https://doi.org/10.1146/annurev-commatphys-031214-014710).
- [99] R. Matas-Navarro, R. Golestanian, T. B. Liverpool, S. M. Fielding, “Hydrodynamic suppression of phase separation in active suspensions”, *Phys. Rev. E* **2014**, *90*, 032304, DOI [10.1103/PhysRevE.90.032304](https://doi.org/10.1103/PhysRevE.90.032304).
- [100] I. Theurkauff, C. Cottin-Bizonne, J. Palacci, C. Ybert, L. Bocquet, “Dynamic Clustering in Active Colloidal Suspensions with Chemical Signaling”, *Phys. Rev. Lett.* **2012**, *108*, 268303, DOI [10.1103/PhysRevLett.108.268303](https://doi.org/10.1103/PhysRevLett.108.268303).
- [101] M. Abkenar, K. Marx, T. Auth, G. Gompper, “Collective behavior of penetrable self-propelled rods in two dimensions”, *Phys. Rev. E* **2013**, *88*, 062314, DOI [10.1103/PhysRevE.88.062314](https://doi.org/10.1103/PhysRevE.88.062314).
- [102] H. Moore, K. Dvorková, N. Jenkins, W. Breed, “Exceptional sperm cooperation in the wood mouse”, *Nature* **2002**, *418*, 174, DOI [10.1038/nature00832](https://doi.org/10.1038/nature00832).
- [103] S. Immler, H. D. Moore, W. G. Breed, T. R. Birkhead, “By Hook or by Crook? Morphometry, Competition and Cooperation in Rodent Sperm”, *PLOS ONE* **2007**, *2*, 1–5, DOI [10.1371/journal.pone.0000170](https://doi.org/10.1371/journal.pone.0000170).
- [104] I. H. Riedel, K. Kruse, J. Howard, “A Self-Organized Vortex Array of Hydrodynamically Entrained Sperm Cells”, *Science* **2005**, *309*, 300–303, DOI [10.1126/science.1110329](https://doi.org/10.1126/science.1110329).
- [105] Y. Yang, J. Elgeti, G. Gompper, “Cooperation of sperm in two dimensions: Synchronization, attraction, and aggregation through hydrodynamic interactions”, *Phys. Rev. E* **2008**, *78*, 061903, DOI [10.1103/PhysRevE.78.061903](https://doi.org/10.1103/PhysRevE.78.061903).
- [106] F. Ginelli, F. Peruani, M. Bär, H. Chaté, “Large-Scale Collective Properties of Self-Propelled Rods”, *Phys. Rev. Lett.* **2010**, *104*, 184502, DOI [10.1103/PhysRevLett.104.184502](https://doi.org/10.1103/PhysRevLett.104.184502).
- [107] J. A. Cohen, R. Golestanian, “Emergent Cometlike Swarming of Optically Driven Thermally Active Colloids”, *Phys. Rev. Lett.* **2014**, *112*, 068302, DOI [10.1103/PhysRevLett.112.068302](https://doi.org/10.1103/PhysRevLett.112.068302).

- [108] M. Ripoll, R. Winkler, G. Gompper, “Hydrodynamic screening of star polymers in shear flow”, English, *Eur. Phys. J. E* **2007**, *23*, 349–354, DOI [10.1140/epje/i2006-10220-0](https://doi.org/10.1140/epje/i2006-10220-0).
- [109] R. J. Archer, A. I. Campbell, S. J. Ebbens, “Glancing angle metal evaporation synthesis of catalytic swimming Janus colloids with well defined angular velocity”, *Soft Matter* **2015**, *11*, 6872, DOI [10.1039/c5sm01323b](https://doi.org/10.1039/c5sm01323b).

Acknowledgements

Foremost, I would like to express my sincerest gratitude to my supervisors, Prof. Dr. Gerhard Gompper and Dr. Marisol Ripoll, for taking me on as a PhD student and introducing me to the field of soft matter systems. Working in close cooperation with Dr. Ripoll has always been a pleasure, and I would like to say thank you for always being available, even at the most unorthodox times, for any question I had as well as for perpetually and patiently discussing each and every aspect of the work. I am also very thankful for her trusting in that my spending a whole lot of time on learning parallel programming and developing an own approach to these simulations will be worthwhile in the end.

Then, I am truly grateful to Prof. Dr. Ulrich K. Deiters, not only for taking over the role of second examiner for this thesis, but also for having introduced me to the great world of programming and simulations early in my master studies.

Furthermore, I would like here to acknowledge the support of the DFG priority program SPP 1726 on “Microswimmers - from Single Particle Motion to Collective Behaviour” as well as the computing time granted on the supercomputer JURECA at Jülich Supercomputing Centre (JSC).

I greatly appreciate the nice working atmosphere all my fellow colleagues at the ICS-2 provided over the years. Especially, I would like to thank Dinar and Zihan for the great time we had in the office, and the many others who joined me on recreational walks.

The deepest gratitude I feel towards my family, who have always supported me in each and every aspect of my life and work. Of all the people involved, I would like to first thank my parents, Cornelia and Ralf, for the uncountable, valuable contributions they made to all my life and education. I would like to thank my brother, Thomas, for patiently listening to my mathematical problems while driving home and making valuable suggestions to solve them. My heartfelt thanks extend to my in-law family, Hannah, Andrea and Ralf, living together with whom has always been a pleasure. Especially to my sister-in-law, Hannah, I would like to say thank you for taking care of every annoying everyday task for me in the critical time of finishing the writing of this thesis.

At last, the most important person in my life remains to be thanked, yet words cannot express all I wish to say to my wife Svenja. I will be forever grateful for everything you were, have been, and are to me.

Eigenständigkeitserklärung

Ich versichere, dass ich die von mir vorgelegte Dissertation selbständig angefertigt, die benutzten Quellen und Hilfsmittel vollständig angegeben und die Stellen der Arbeit – einschließlich Tabellen, Karten und Abbildungen –, die anderen Werken im Wortlaut oder dem Sinn nach entnommen sind, in jedem Einzelfall als Entlehnung kenntlich gemacht habe; dass diese Dissertation noch keiner anderen Fakultät oder Universität zur Prüfung vorgelegen hat; dass sie – abgesehen von unten angegebenen Teilpublikationen – noch nicht veröffentlicht worden ist, sowie, dass ich eine solche Veröffentlichung vor Abschluss des Promotionsverfahrens nicht vornehmen werde. Die Bestimmungen der Promotionsordnung sind mir bekannt. Die von mir vorgelegte Dissertation ist von Prof. Dr. Gerhard Gompper und Dr. Marisol Ripoll betreut worden.

(Ort, Datum)

(Unterschrift)

Teilpublikation

Martin Wagner and Marisol Ripoll: Hydrodynamic Swarming of Thermally Active Dimeric Colloids, arXiv:1701.07071 [cond-mat.soft]

Curriculum Vitae

Martin Wagner

————— Persönlich

Geburtsdatum 2. November 1988
Geburtsort Düsseldorf, Deutschland

————— Ausbildung

Aug. 2014 **Doktorand**, *Forschungszentrum Jülich/Universität zu Köln*,
– Nov. 2017 Jülich/Köln
Okt. 2011 **Msc Chemie**, *Universität zu Köln*, Köln, Note 1.2
– Juli 2014
Okt. 2008 **Bsc Chemie**, *Heinrich-Heine-Universität*, Düsseldorf, Note 1.6
– Sept. 2011
1999–2008 **Abitur**, *Annette-von-Droste-Hülshoff-Gymnasium*, Düsseldorf, Note 1.2

————— Master Chemie

Masterarbeit Investigation of nucleation in aqueous systems via molecular dynamics simulations
Betreuer PD Dr. T. Kraska, Institut für Physikalische Chemie, Köln
Note 1.0

————— Bachelor Chemie

Bachelorarbeit Neue β -Prolin-Derivate für die Organokatalyse
Betreuer Prof. Dr. J. Pietruszka, Institut für bio-organische Chemie, Jülich/Düsseldorf
Note 1.0